

See discussions, stats, and author profiles for this publication at: <https://www.researchgate.net/publication/257144920>

A Direct Measurement of Cosmic Rays to Very High Energies: Implications for Galactic Propagation and Sources

Thesis · February 2011

CITATIONS

2

READS

563

1 author:



[A. Obermeier](#)

RWTH Aachen University

24 PUBLICATIONS 2,467 CITATIONS

[SEE PROFILE](#)

A Direct Measurement of Cosmic Rays to Very High Energies

Implications for Galactic Propagation and Sources

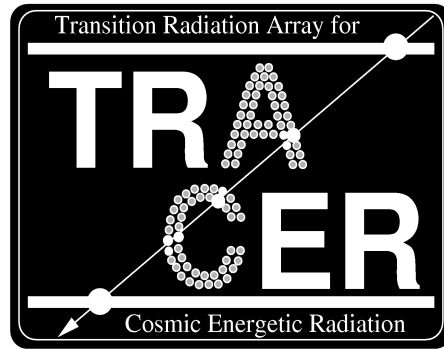
Andreas Obermeier



A Direct Measurement of Cosmic Rays to Very High Energies

Implications for Galactic Propagation and Sources

Andreas Obermeier



Cover Art by P. Herrmann: The Path of TRACER

Printed by Ipskamp Drukkers, Enschede
www.ipskampdrukkers.nl

ISBN 978-90-9025962-8

A Direct Measurement of Cosmic Rays
to Very High Energies:
Implications for Galactic Propagation and Sources

Een wetenschappelijke proeve
op het gebied van de Natuurwetenschappen, Wiskunde en Informatica

Proefschrift

ter verkrijging van de graad van doctor
aan de Radboud Universiteit Nijmegen
op gezag van de rector magnificus prof. mr. S.C.J.J. Kortmann,
volgens besluit van het college van decanen
in het openbaar te verdedigen op woensdag 23 februari 2011
om 10:30 uur precies

door

Andreas Obermeier

geboren op 15 december 1980
te Eggenfelden, Duitsland

Promotores: Prof. dr. S J. de Jong
Prof. dr. D. Müller
The University of Chicago, VS

Copromotor: Dr. habil. J.R. Hörandel

Manuscriptcommissie: Prof. dr. R. Kleiss (voorzitter)
Prof. dr. A.M. van den Berg
Rijksuniversiteit Groningen
Prof. dr. P. Groot
Dr. Ch. Timmermans
Prof. dr. S. Wakely
The University of Chicago, VS

A Direct Measurement of Cosmic Rays
to Very High Energies:
Implications for Galactic Propagation and Sources

An academic essay in Science

Doctoral thesis

to obtain the degree of doctor
from Radboud Universiteit Nijmegen
on the authority of the Rector Magnificus, Prof. S. C. J. J. Kortmann,
according to the decision of the Council of Deans
to be defended in public on Wednesday, 23 February 2011
at 10:30 hrs

by

Andreas Obermeier

born on 15 December 1980
in Eggenfelden, Germany

Supervisors:

Prof. Dr. S. J. de Jong

Prof. Dr. D. Müller
The University of Chicago, USA

Co-Supervisor:

Dr. habil. J. R. Hörandel

Reading Committee:

Prof. Dr. R. Kleiss (chair)

Prof. Dr. A. M. van den Berg
University of Groningen

Prof. Dr. P. Groot

Dr. Ch. Timmermans

Prof. Dr. S. Wakely
The University of Chicago, USA

CONTENTS

| | |
|---|-----------|
| Introduction | ix |
| 1 High-Energy Cosmic Rays in the Galaxy | 1 |
| 1.1 A General Introduction to Cosmic Rays | 1 |
| 1.2 Sources of Galactic Cosmic Rays | 2 |
| 1.3 Propagation of Cosmic Rays in the Galaxy | 5 |
| 1.4 Direct Measurements of Cosmic Rays | 8 |
| 2 The TRACER Detector, its Flights, and its Status | 9 |
| 2.1 The Balloon Flights of TRACER | 9 |
| 2.2 Detector Description | 11 |
| 2.2.1 Upgrades for the 2006 Balloon Flight from Sweden | 15 |
| 2.2.2 Geometric Aperture | 16 |
| 2.3 Energy Response and Resolution | 17 |
| 2.3.1 Response of the Čerenkov Detector | 17 |
| 2.3.2 Response of the dE/dX-array and the Transition Radiation Detector | 17 |
| 2.3.3 Energy Resolution | 19 |
| 2.4 Detector Performance and Status | 21 |
| 2.5 Description of the Data of the Sweden Flight | 23 |
| 3 Summary of Previous Results from TRACER | 25 |
| 4 Signal Reconstruction from Raw Data | 29 |
| 4.1 Trajectory Reconstruction | 30 |
| 4.1.1 First Level | 30 |
| 4.1.2 Second Level | 31 |
| 4.2 Combining High-Gain and Low-Gain Proportional Tube Signals | 32 |
| 4.3 Tube Alignment | 33 |
| 4.4 Lateral Response Maps | 34 |
| 4.4.1 Maps from Muon Data | 35 |
| 4.4.2 Comparison to Maps from Cosmic-Ray Data | 37 |
| 4.5 Time Dependent Gain Normalization | 39 |
| 4.6 The Reconstructed Signal | 39 |
| 4.6.1 Scintillation and Čerenkov Signal | 39 |

| | | |
|----------|---|------------|
| 4.6.2 | dE/dX-array and TRD Signal | 40 |
| 5 | Charge Measurement | 41 |
| 5.1 | The Scintillator-Čerenkov Correlation | 41 |
| 5.1.1 | Preliminary Charge Estimation | 42 |
| 5.1.2 | Parametrization of the Lines of Constant Charge | 42 |
| 5.2 | Charge Assignment and Resolution | 44 |
| 5.3 | Charge-Changing Interactions | 46 |
| 5.4 | The Selection of Elements | 48 |
| 5.5 | Carbon Contamination in the Boron Sample | 50 |
| 6 | Energy Measurement — The Energy Spectra of Cosmic Rays | 53 |
| 6.1 | The Determination of the Spectra | 53 |
| 6.1.1 | Quality Cuts and High-Energy Selection | 53 |
| 6.1.2 | Determination of the Differential Flux | 54 |
| 6.1.3 | Event Counting and Efficiencies | 56 |
| 6.1.4 | Evaluation of Bin Correlations | 57 |
| 6.2 | Energy Spectra of Iron, Oxygen, and Carbon | 59 |
| 6.3 | Energy Spectrum of Boron | 64 |
| 6.3.1 | Carbon Contamination | 64 |
| 6.3.2 | Atmospheric Production | 66 |
| 6.3.3 | The Spectrum of Boron | 70 |
| 7 | The Boron-to-Carbon Ratio and its Implications | 73 |
| 7.1 | The Boron-to-Carbon Ratio | 73 |
| 7.2 | Discussion of the Result | 76 |
| 7.2.1 | A Leaky-Box Model with Residual Pathlength | 76 |
| 7.2.2 | The Effect of a Leaky-Box Model on Cosmic-Ray Spectra | 80 |
| 7.2.3 | Comparison of the Data with GALPROP | 82 |
| 7.2.4 | Synopsis of the Results | 84 |
| 8 | Concluding Summary | 87 |
| | Deutsche Zusammenfassung | 89 |
| | Nederlandse samenvatting | 93 |
| | Bibliography | 97 |
| | Acknowledgments | 105 |
| | Curriculum Vitae and List of Publications | 107 |

INTRODUCTION

This thesis describes measurements of the individual energy spectra of cosmic-ray nuclei of boron, carbon, oxygen, and iron at high energies. Special emphasis is given to the determination of the abundance of the secondary boron nuclei, relative to their parent element carbon.

The Earth is exposed to a steady flux of cosmic radiation, the bulk of which appears to be of Galactic origin. However, cosmic-ray sources in the Galaxy could not yet have been investigated in detail. In order to determine properties of the sources, propagation effects altering cosmic-ray energy spectra and composition on their way from the sources to the Earth need to be understood. The major parameter for the propagation of cosmic radiation in the Galaxy is the diffusion coefficient or, in a simpler approximation, the escape pathlength.

The elemental abundance ratio of boron to carbon is a measure for the escape pathlength. Boron is not produced in nucleosynthesis processes, so that all cosmic-ray boron observed at the Earth is the result of cosmic-ray interactions with the interstellar medium. The longer the time a carbon nucleus, boron's parent nucleus, is confined within the Galaxy, the more boron is produced. Thus, a measurement of the boron-to-carbon abundance ratio can determine the average matter traversed by cosmic rays in the Galaxy.

The energy spectrum of cosmic radiation is falling very steeply with increasing energy. This makes the direct measurement of cosmic-rays at high energy extremely challenging, because it requires a large exposure factor and has to be conducted at the top of the atmosphere. Direct measurements are achieved by means of satellite or balloon-borne experiments. However, balloon-borne experiments are often the preferred means because of the much lower costs compared to satellite missions. The balloon-borne TRACER detector ("Transition Radiation Array for Cosmic Energetic Radiation") is designed to measure cosmic-ray energy spectra to high energies for individual elements from boron to iron ($Z = 5$ to 26), and well into the TeV/amu energy region.

TRACER is currently the largest balloon-borne cosmic-ray detector with a geometric aperture of about $5 \text{ m}^2 \text{ sr}$. TRACER utilizes only electromagnetic interactions to determine the charge and the energy of cosmic-ray nuclei traversing the detector. All detector components are optimized for low weight, low power consumption, and operation in external vacuum. After a test flight in 1999, TRACER was launched in two long-duration balloon flights: in the year 2003 in Antarctica and in 2006 from Sweden.

In this thesis the data from the most recent flight will be presented and analyzed. All data

analysis steps and all necessary data corrections will be outlined. The absolute energy spectra of iron, oxygen, carbon and boron will be presented. The boron-to-carbon abundance ratio will be determined up to 2 TeV/amu. All results will be discussed in the light of previous measurements and different propagation models.

The contribution of the author to the TRACER project begins with post-flight hardware testing, includes the complete data analysis for the latest flight, and ends with the interpretation of the measurement. Although the data analysis builds upon the experience of the previous measurement from the Antarctic flight, all data analysis steps have been newly evaluated, altered and updated. Also, additional operations have been included in the analysis chain. For the work on this project the author spent three years at the Enrico Fermi Institute of the University of Chicago (USA).

This thesis is organized as follows. The first chapter gives a brief introduction to cosmic radiation and introduces a model for cosmic-ray propagation in the Galaxy. In the second chapter, the TRACER detector and its flights are described. Also, a description of the data and the current status of the instrument is included in this chapter. For completeness, previous results from TRACER are outlined in Chapter three.

Chapter 4 describes analysis and signal corrections of the initial data. The processed signals are used for charge measurement in Chapter 5, and for the determination of the energy spectra in Chapter 6. Finally, the boron-to-carbon ratio and the implications of the measured data are discussed in Chapter 7. After the concluding Chapter 8, summaries in German and Dutch are appended.

CHAPTER 1

HIGH-ENERGY COSMIC RAYS IN THE GALAXY

In this chapter a general description of Galactic cosmic rays is given. It is kept brief and the interested reader is referred to the many textbooks and reviews that give a broader description of the subject, for example [18, 30, 33, 54, 76, 80].

This chapter also introduces a model of cosmic radiation assuming that cosmic rays are accelerated in Galactic sources, and subsequently propagate through the interstellar medium and magnetic fields.

1.1 A General Introduction to Cosmic Rays

The phenomenon of cosmic radiation was discovered at the beginning of the 20th century, when Viktor Hess observed an increase of ionization in the atmosphere at high altitudes during his famous balloon flights in 1912 [37]. He concluded that this phenomenon could not be explained by terrestrial radioactivity [38], and so a new source of radiation was later proposed to explain his findings: cosmic radiation from outer space or “penetrating radiation” [58].

Scientists began to undertake many experiments in order to uncover the nature of cosmic radiation. There were more balloon flights, and later aircraft and satellite experiments. Also observations at sea level and at mountain altitudes were conducted, and ground arrays were constructed, after Kolhörster [47] and Auger [11] discovered “extensive cosmic-ray showers” in 1938.

Cosmic radiation provides particles at energies that cannot be reached with man-made accelerators. Until the 1950s, it was not possible to observe the primary cosmic-ray particles directly, but only the many secondary particles that are produced in the atmosphere. These particles still extended to energies beyond anything accelerators could produce. Therefore, cosmic-ray studies led to many discoveries in particle physics. The positron [8], the muon [64, 77], the pion, and several strange particles like the kaon were discovered. Also, an experimental proof of special relativity was provided by the observation of time dilation of the muon lifetime in air showers induced by cosmic rays [74].

While particle physics later relied more and more on the new generation of accelerators, high-altitude balloon and satellite experiments made it possible to access primary cosmic-ray particles above the atmosphere. Thus, cosmic-ray research became a subject of astrophysics.

Cosmic radiation does not mainly consist of photons, but mostly of atomic nuclei. The major component is protons, but all elements up to uranium have been found, as well as electrons, positrons and anti-protons.

In Figure 1.1 the elemental abundances of Galactic cosmic-ray nuclei at low energy (GCR, 170 MeV/amu) are compared to the solar-system abundances. The trends of the two abundance distributions are similar for most elements. A striking difference occurs for light elements below carbon (Li, Be, and B), as well as for elements lighter than iron ($Z = 21$ to 25). These elements are only very sparsely if at all produced by nucleosynthesis. They are products of spallation processes of cosmic-ray nuclei colliding with interstellar matter. Hence, *primary* cosmic rays — like C, O, or Fe — that are accelerated in the sources are distinguished from *secondary* cosmic rays — like Be, B, or Mn — that are produced by spallation in the interstellar medium.

The previously measured abundances of secondary elements below 200 MeV/amu (Fig. 1.1) show that nuclei at low energy have to traverse 5 to 10 g/cm² of interstellar matter before they can be observed at the Earth. Radioactive nuclei, termed “cosmic-ray clocks”, reveal a confinement time of these cosmic rays in the Galaxy of about $1.5 \cdot 10^7$ years [31, 95], which in turn requires the average galactic density they encounter to be about 0.3 protons/cm³. Thus, cosmic-ray particles travel mostly through the galactic halo. The particles do not approach the Earth in a straight line from their sources, but travel in a diffuse, undirected way. This can be expected because of the randomly oriented Galactic magnetic field of about 3 μ G [36] through which cosmic-ray nuclei propagate.

The energy spectrum of cosmic radiation covers more than 12 decades in energy and more than 30 decades in intensity (Figure 1.2). It can be described with a broken power law [61]:

$$\frac{dN}{dE} \propto E^{-\gamma}, \quad \gamma \approx \begin{cases} 2.75, & E \lesssim 4 \cdot 10^{15} \text{ eV} \\ 3.05, & 4 \cdot 10^{15} \text{ eV} \lesssim E \lesssim 10^{19} \text{ eV} \\ 2.75, & E \gtrsim 10^{19} \text{ eV.} \end{cases} \quad (1.1)$$

At 10^{11} eV the cosmic-ray intensity exceeds 1 particle per m² per second, but decreases to about 1 particle per km² per century at 10^{20} eV [61]. The first change in the spectral index γ occurs at 4 PeV, called the “knee”, and a second change of γ , the so-called “ankle”, may appear at around 10 EeV. The cosmic-ray spectrum is then believed to feature a sharp cutoff at about $6 \cdot 10^{19}$ eV, called the “GZK-cutoff” [35, 61, 96].

1.2 Sources of Galactic Cosmic Rays

Sources of Galactic cosmic rays must be able to accelerate the particles to the observed energies and must be able to sustain the estimated energy density of about 1 eV/cm³ of cosmic radiation in the Galaxy.

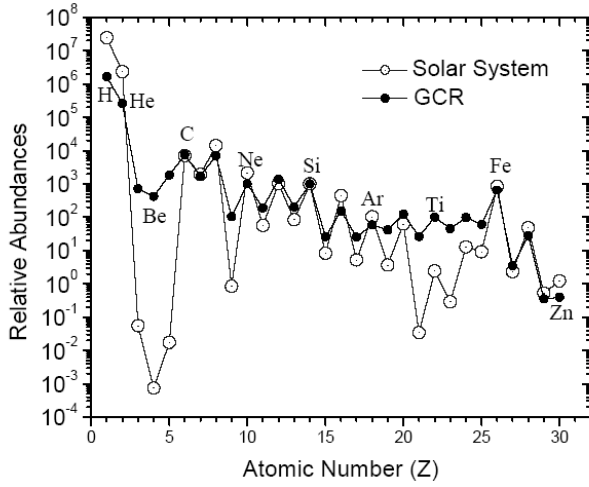


Figure 1.1: Abundances of elements ($Z < 30$) at about 170 MeV/amu measured by the ACE/CRIS experiment, normalized to Si. The differences between Galactic cosmic-ray (GCR) and solar-system abundances are explained in the text. [53]

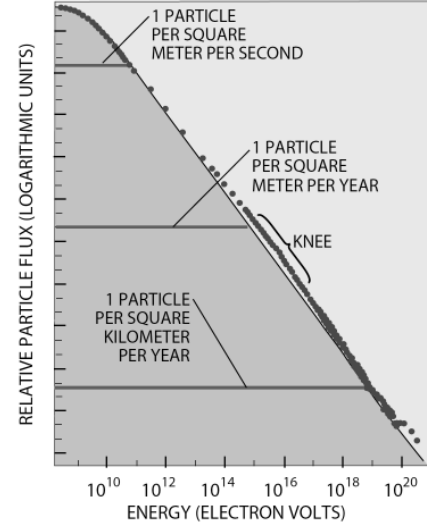


Figure 1.2: Flux of cosmic rays as a function of energy. The power law is broken at the “knee” (at 10^{15} eV) and the “ankle” (at 10^{19} eV, not labeled). Compiled by S. Swordy [23].

An acceleration process for cosmic-ray particles that leads to a power-law energy spectrum was first introduced by Fermi [28]. Fermi proposed that particles collide with moving magnetized clouds in interstellar space. Each time they encounter a cloud they gain, on average, energy proportional to their initial energy, $\Delta E = \epsilon E$, and have a chance of escaping the cloud P_e . After n encounters they have an energy of $E_n = E_0(1 + \epsilon)^n$, and the number of particles that gain more energy than E is given by:

$$N(> E) \propto \frac{1}{P_e} \left(\frac{E}{E_0} \right)^{-\gamma}, \quad (1.2)$$

with

$$\gamma = \frac{\ln(\frac{1}{1-P_e})}{\ln(1+\epsilon)}. \quad (1.3)$$

This results in a power-law energy spectrum. The energy gain ϵ is proportional to the square of the cloud’s speed $\beta^2 = v_c^2/c^2$, so that the acceleration takes a long time and is inefficient, especially for heavier nuclei, as Fermi already pointed out in his seminal paper [28].

In the 1970s, Fermi’s idea of stochastic acceleration was modified by Bell [15] and others. A similar mechanism was proposed not for magnetic clouds, but for expanding shock fronts, for example generated by supernova explosions. In this scenario, again a power-law shape of the spectrum is obtained, but the acceleration is much faster because the particle gains energy not on average, but in every encounter. The energy gain per encounter ϵ is then proportional to $\beta = v_s/c$ (first-order Fermi acceleration). The expected power-law index of the differential energy spectra for acceleration at strong shocks is close to 2. Note that this is smaller than the observed value (Eq. (1.1)).

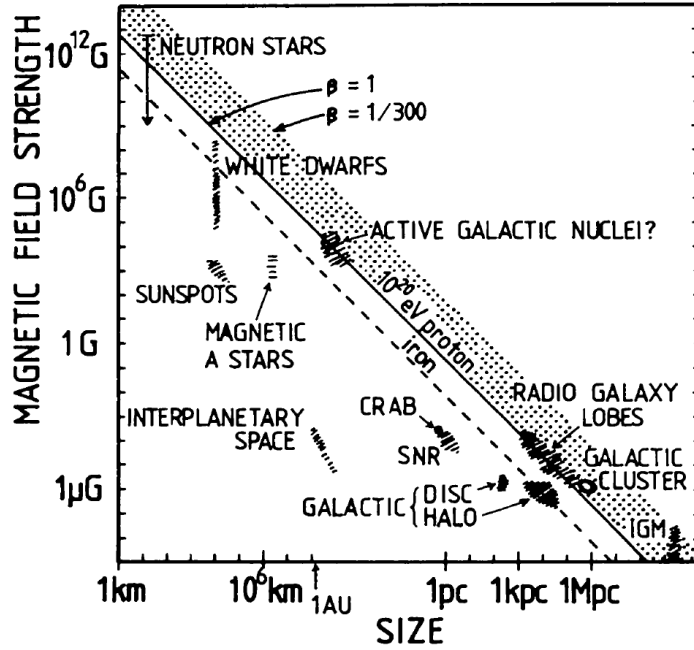


Figure 1.3: Hillas plot (1984): Characterization of astrophysical objects with respect to size and magnetic field strength. Objects below the lines cannot accelerate particles to 10^{20} eV. β refers to the velocity of the shock front. [39]

Energetic arguments require a power output of about $7 \cdot 10^{40}$ erg s^{-1} to sustain the population of cosmic rays in the Galaxy. This requires very powerful sources, as can be found in supernova remnants (SNRs), if at least several % of the released energy is assumed to be transformed into cosmic radiation (e. g. [69, 76]).

The power-law energy spectrum, described with Eq.(1.2), is restricted to a maximum energy that depends on the ability of the source to confine the particle. The gyro radius of the particle in the source needs to be smaller than the source itself. The maximum energy is then proportional to the size and magnetic field of the source. A general estimate yields [39, 61]

$$E_{max} \propto ZBR, \quad (1.4)$$

with the magnetic field strength B , radius R of the source, and nuclear charge Z of the particle.

The limit (1.4) can be used to classify astrophysical objects as sources for cosmic rays. This is shown in a Hillas plot [39], Figure 1.3, where size and magnetic field strength are used to arrange objects according to the maximum cosmic-ray energy they could reach. A constant E_{max} corresponds to a diagonal line, and objects above the line are able to accelerate a particle to that energy. The position of the line depends, as shown, on the particle charge and the velocity of the shock front.

Figure 1.3 shows that Galactic sources like supernova remnants (SNR) do not reach the highest energies observed in the cosmic-ray spectrum. There is some uncertainty on the maximum energy that can be reached by Galactic sources. The maximum energy estimated ranges from 10^{14} eV for protons [51] to 10^{18} eV in special cases [72]; for a review see also [43].

The implied transition from Galactic to extragalactic cosmic radiation may occur in the energy range around the “ankle”.

The maximum energy is also dependent on the charge of the accelerated species (see Eq. 1.4). This is a possible explanation of the steepening of the spectrum at the “knee”. When the proton (or light) component begins to reach this limit, but heavier nuclei can still be accelerated to higher energies, the overall effect is a steepening. The ground-based KASCADE experiment investigated the composition of cosmic rays at the knee [45]. It has reported that the composition tends to become heavier, supporting the hypothesis of supernova remnants reaching their acceleration limit.

Unambiguous evidence that supernova remnants are the sources of Galactic cosmic rays has not yet been shown. In fact, not only the acceleration but also the propagation of cosmic rays through the Galaxy is not fully understood yet. To come closer to the answers, many approaches are pursued to observe cosmic rays. From measuring the highest energy particles with huge ground-based arrays like Auger [75], to satellites that can distinguish isotopes of cosmic radiation at low energies (e. g. ACE [44]), or with indirect means by looking for γ -ray sources (e. g. with Fermi [10], VERITAS [92], or H.E.S.S. [40]). Major contributions continue to be made by direct observations using balloon-borne detectors like TRACER.

1.3 Propagation of Cosmic Rays in the Galaxy

For a simple model of cosmic rays in the Galaxy (illustrated in Fig. 1.4), it is assumed that the Galaxy is populated homogeneously with sources of cosmic rays. Cosmic rays then propagate diffusively through the interstellar medium. This is described by the continuity equation for the differential intensity $N_i(E)$ (in units of flux: $\text{m}^{-2} \text{s}^{-1} \text{sr}^{-1} (\text{GeV}/\text{amu})^{-1}$) of stable nuclear component i , where E is the kinetic energy per nucleon (e. g. [33]):

$$Q_i(E) + \sum_{k>i} \frac{\beta c \rho}{m} \int_{E'>E} \frac{d\sigma_{k \rightarrow i}(E, E')}{dE'} N_k(E') dE' = -\nabla(D_i(E)\nabla N_i(E)) + \frac{\partial}{\partial E}(b_i(E)N_i(E)) + \nabla \cdot \vec{u}N_i(E) + \frac{\beta c \rho}{\Lambda_i} N_i(E). \quad (1.5)$$

The left hand side of the equation comprises the rate of production at the source Q_i and the gains due to spallation of heavier nuclei k into species i in the interstellar medium, with velocity $\beta = \frac{v}{c}$, the speed of light c , the mass density of interstellar gas ρ , the average mass of an interstellar “atom” m , and the differential cross section $d\sigma_{k \rightarrow i}(E, E')$ for spallation of species k with energy E' into species i with energy E . The right hand side describes the losses due to diffusion with diffusion coefficient D_i , energy losses through ionization or energy gains through reacceleration (all included in $b_i = \frac{\partial E}{\partial t}$), convection with convection velocity \vec{u} , and spallation losses with spallation pathlength Λ_i .

The energy dependence of the diffusion coefficient D of Eq. (1.5) is a consequence of the random nature of the Galactic magnetic field B (see for example [69, 70]). Cosmic rays are scattered randomly (and thus diffusively) in the magnetic field’s irregularities. Particles feel only irregularities whose sizes are of the order of their Larmour radius $1/k \approx r_l = pc/ZeB$

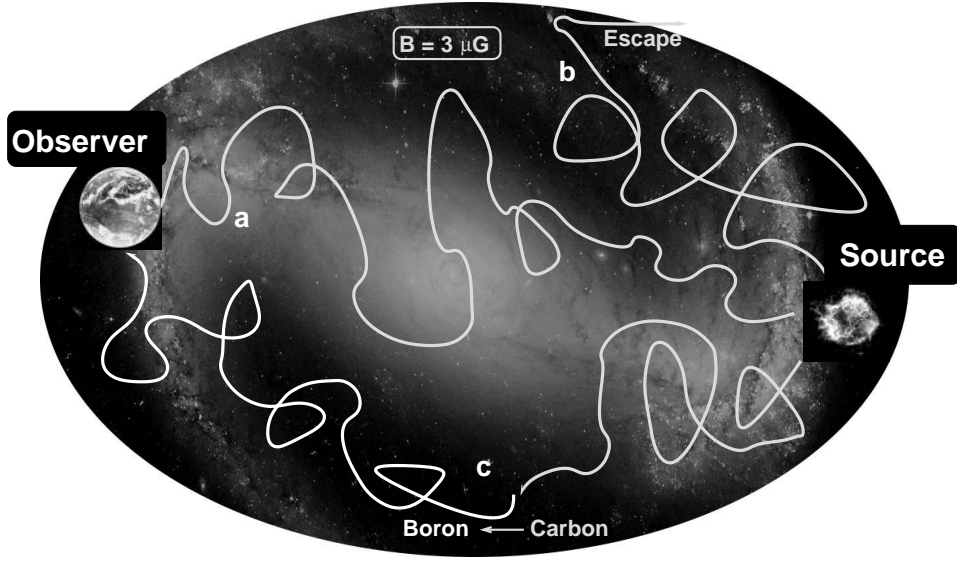


Figure 1.4: Illustration of a simple Leaky-Box model for Galactic cosmic rays. Sources emit cosmic rays into the Galaxy, which then propagate diffusively in the interstellar magnetic field until they (a) reach the Earth, (b) escape the Galaxy, or (c) spallate into lighter nuclei — as shown for the example of carbon producing boron.

(or $r_l = RB$ with rigidity $R = pc/Ze$ measured in volts, momentum p , charge Ze , the speed of light c , and wavenumber k of the magnetic field fluctuations). The diffusion coefficient can be estimated to be ([69], in units of m^2/s):

$$D \approx \frac{vr_l}{3} \left(\frac{\tilde{B}^2}{B^2} \right)^{-1} \approx 3 \cdot 10^{28} \left(\frac{R}{10^9 \text{V}} \right)^\delta, \quad (1.6)$$

with the particles' velocity v and the amplitude of the random field fluctuations \tilde{B} . The diffusion coefficient turns out to be a function of rigidity R (i. e. a function of energy) as a power-law with index δ . For typical Galactic magnetic field fluctuations, δ ranges from 0.2 to 0.6, where $1/3$ corresponds to a Kolmogorov spectrum [48] in magnetic fluctuations.

The number of free parameters in Eq. (1.5) is so large that a simpler version is usually adopted for the interpretation of experimental data, or numerical models like GALPROP [78] are used.

A popular simplified model is the “Leaky-Box” model that treats the Galaxy as a uniform and homogeneous volume with a homogeneous cosmic-ray density. It is clear that in such a structureless volume convection has no bearing. Also, there is no reacceleration or energy loss, due to ionization, taken into account. These effects have some influence on the observed cosmic-ray fluxes, but almost exclusively at low energies (i. e. $E < 40 \text{ GeV}/\text{amu}$, [71]).

The diffusion term in Eq. (1.5) is simplified by introducing the mean containment time $\tau(E)$ of cosmic rays in the Galaxy, or equivalently the escape pathlength $\Lambda_{\text{esc}}(E)$:

$$\Lambda_{\text{esc}}(E) = \beta c \rho \tau(E), \quad (1.7)$$

which is interpreted as the amount of matter a particle traverses on average before it escapes the confinement of the Galaxy. In [70] it is pointed out that the escape pathlength and the diffusion

coefficient D are equivalent within the flat halo diffusion model, where $\Lambda_{\text{esc}} = \mu v H / (2D)$ with the surface gas density of the Galactic disc μ , the velocity of a particle v , and the height of the Galactic halo H .

Combining this and the rigidity dependence of D from Eq. (1.6), one expects the escape pathlength to decrease with energy according to a power law. In order to prevent the escape pathlength from becoming arbitrarily small, which means that a cosmic-ray particle could escape the Galaxy instantly, a residual pathlength Λ_0 has been introduced (e. g. [13, 81]). With this, the escape pathlength at high-energy can be written as:

$$\Lambda_{\text{esc}}(E) = C \cdot E^{-\delta} + \Lambda_0, \quad (1.8)$$

where δ is the power-law index introduced to describe the energy dependence of the diffusion coefficient in Eq. (1.6).

With these simplifications outlined above, the Leaky-Box approximation is defined as illustrated in Fig. 1.4. The continuity equation for cosmic radiation in the Galaxy (1.5) becomes

$$\begin{aligned} N_i(E) &= \frac{1}{\Lambda_{\text{esc}}(E)^{-1} + \Lambda_s(A)^{-1}} \left(\frac{Q_i(E)}{\beta c \rho} + \sum_{k>i} \frac{N_k}{\Lambda_{k \rightarrow i}} \right) \\ &= \frac{1}{(C \cdot E^{-\delta} + \Lambda_0)^{-1} + \Lambda_s(A)^{-1}} \left(\frac{n_i \cdot E^{-\alpha}}{\beta c \rho} + \sum_{k>i} \frac{N_k}{\Lambda_{k \rightarrow i}} \right), \end{aligned} \quad (1.9)$$

where the source term Q_i can be written in its simplest form as a power law with source abundances n_i and source spectral index α . The spallation term is expressed, analogous to the diffusion term, as a spallation pathlength Λ_s that depends not on energy but on the mass number A of the particle. The production pathlength $\Lambda_{k \rightarrow i}$ describes the spallation gains of element i from heavier nuclei k . For a target nucleus of mass m , the interaction pathlengths Λ are related to the respective cross sections σ as

$$\Lambda = \frac{m}{\sigma}. \quad (1.10)$$

It can be seen in Eq. (1.9) that the two effects of spallation and escape compete to decide a cosmic ray's fate. The smaller pathlength is the dominant factor, so that at high energies (for which the escape pathlength is becoming small) the leakage from the Galaxy is the major propagation effect that modifies the cosmic-ray energy spectra.

For boron, the source term in Eq. (1.9) is not applicable. Thus, the differential boron intensity becomes:

$$N_B = \frac{1}{\Lambda_{\text{esc}}^{-1} + \Lambda_s^{-1}} \cdot \left(\sum_{k>B} \frac{N_k}{\Lambda_{k \rightarrow B}} \right), \quad (1.11)$$

where the boron production stems exclusively from the spallation of heavier elements. Expressing the production of boron relative to the carbon intensity with an effective production pathlength $\Lambda_{\rightarrow B}$, Equation (1.11) can be solved for the boron-to-carbon ratio (B/C):

$$\left(\frac{B}{C} \right) = \frac{N_B}{N_C} = \frac{\Lambda_{\rightarrow B}^{-1}}{\Lambda_{\text{esc}}^{-1} + \Lambda_s^{-1}}, \quad (1.12)$$

where it is assumed that the Lorentz factor, or energy per nucleon, is conserved in the spallation process. In the equation it is evident that a measurement of the boron-to-carbon ratio can determine the escape pathlength Λ_{esc} , if the spallation pathlengths are known. The equation is discussed in more detail in Section 7.2.1, where it is used to estimate the escape pathlength from the new measurement presented in this thesis.

1.4 Direct Measurements of Cosmic Rays

For energies up to 10^{15} eV (i. e. below the knee), cosmic radiation can be directly observed above the Earth's atmosphere. High-altitude balloons and satellites facilitate these observations, but also impose severe limitations on detector size, weight, power consumption, and especially in case of balloons, flight duration. These limiting factors restrict the total exposure factor that can be reached, and make direct measurements of cosmic rays extremely challenging.

Balloon-borne experiments are especially versatile as they are low in cost and relatively quick to develop. Since the very beginning, they serve as a reliable basis for cosmic-ray experiments, and as a testing ground for future satellite missions. High-altitude balloons are often the preferred means to reach the top of the atmosphere.

Direct measurements provide more accurate data on cosmic rays than indirect techniques (airshower observations) that depend on extensive simulations. Direct measurements can also resolve individual elements or even isotopes and anti-particles, and have excellent energy resolution.

This makes direct methods the ideal tool to investigate the detailed elemental composition of cosmic rays up to the knee. This could constrain acceleration mechanisms and determine propagation parameters. It could also provide an anchor for indirect methods and provide a constraint on the various nuclear interaction models used in the reconstruction of airshower observations.

The TRACER project combines the sophistication of direct observation techniques with a concept for light-weight detectors that allow a larger aperture than previously possible. The TRACER detector (described in Chapter 2) does not absorb particles in a calorimeter (weighing typically 1 ton per m^2 per hadronic interaction length), but measures charge and energy as they pass through the instrument using only electromagnetic interactions of the particles. This allows TRACER to aim for higher energies than ever before in the search for sources and propagation of cosmic radiation in the Galaxy by direct observation of individual energy spectra of cosmic-ray elements heavier than lithium.

CHAPTER 2

THE TRACER DETECTOR, ITS FLIGHTS, AND ITS STATUS

This chapter gives a description of the TRACER detector (“Transition Radiation Array for Cosmic Energetic Radiation”), its flights, and the measured data that are the basis of this work. The detector design and integration was not part of the work for this thesis, so the description is kept to the necessary details. A fully detailed account will be given in [14].

The TRACER detector was designed and constructed at the University of Chicago, where also the CRN detector was constructed before. CRN [52] was the first detector to use a transition radiation detector (TRD) for the energy measurement of cosmic rays. In many ways, TRACER benefits from the heritage of CRN, especially in the design of its TRD.

TRACER was flown in three balloon flights and underwent upgrades between each flight. Described here is the most recent configuration for the latest flight. The enhancements of the detector implemented for this flight are significant and are described in Section 2.2.1.

2.1 The Balloon Flights of TRACER

The TRACER instrument has had three successful flights on high-altitude balloons. For each flight a 39 million cubic-foot balloon was used. Float altitudes of 36-40 km were reached, corresponding to a residual atmospheric overburden of 3.5-6 g/cm². The instrument and data have been recovered intact after each flight.

First, was a successful test flight in 1999, launched from Ft. Sumner (USA). The flight was 28 hours in duration and proved that the detector functions well and can reach its scientific goals. Its results are reported in [29]. After this, the instrument was launched in two long-duration balloon flights (LDB).

The first LDB flight was launched on December 12, 2003 from McMurdo station in Antarctica. The flight lasted 14 days and a total of 5×10^7 cosmic-ray particles were collected, while TRACER completed one full circle around the South Pole. The instrument had the distinction of being the heaviest payload to be then launched from the continent. The results of this flight are briefly summarized in Chapter 3 and are reported in full detail in [12, 13].

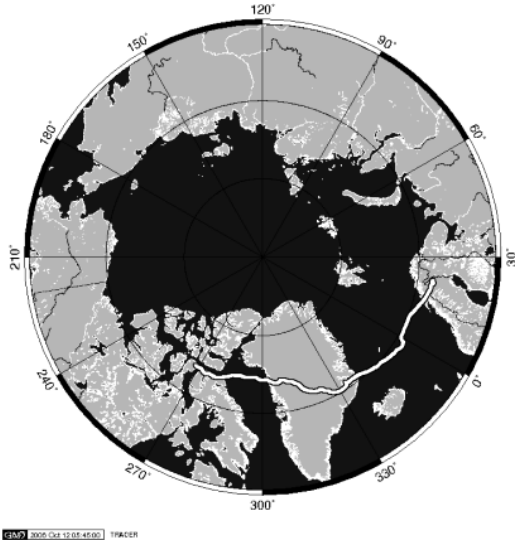


Figure 2.1: Flight trajectory of the instrument in its Arctic flight in 2006 from Kiruna (Sweden) to Canada.

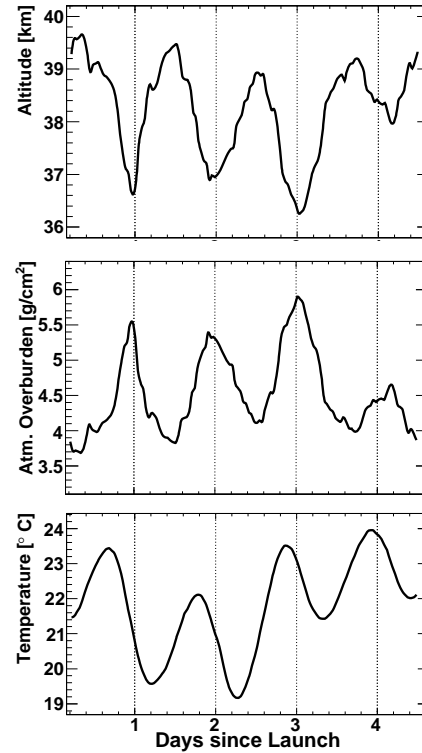


Figure 2.2: Profiles of altitude, atmospheric overburden, and temperature in the instrument as a function of flight time for the 2006 flight.

For the first two flights, the trigger threshold was set such that the instrument had full efficiency for the elements oxygen to iron ($Z = 8$ to 26). In order to extend the range, such that all elements from boron to iron ($Z = 5$ to 26) could be covered, several upgrades were realized for TRACER's latest flight. They are described in Section 2.2.1.

This thesis is based on the data collected during the second LDB flight of the detector. This flight was launched on July 8, 2006 from Kiruna (Sweden) and aimed to fully circle the North Pole. Unfortunately, the flight was limited to 4.5 days due to the lack of permission to fly over Russian territory.

The flight trajectory is shown in Figure 2.1. A total of 3×10^7 cosmic-ray particles were collected with full trigger efficiency from boron to iron. The average atmospheric overburden was 4.5 g/cm^2 . Instrumental profiles, such as altitude, atmospheric overburden, and instrument temperature profiles are shown in Figure 2.2. The altitude of the payload, and thus the residual atmosphere, vary on a daily basis, as the helium gas in the zero pressure balloon expands during the day, lifting the payload higher. During nighttime, the sun's lower intensity decreases the gas temperature, and the altitude drops.

2.2 Detector Description

Overview

TRACER is designed for the measurement of energy spectra of individual cosmic-ray elements. Two quantities need to be measured for each event: the nuclear charge Z to identify the elemental species, and the energy E . The detector must exhibit a large area, but may not exceed limitations set by the lifting capabilities of long-duration balloons. These benchmarks lead to a design using only light-weight detectors that utilize electromagnetic processes only to generate the measured signals.

The active detector elements are $2 \times 2 \text{ m}^2$ in area and form a stack of 1.2 m height. The whole instrument is supported by a 2.5 m high open support structure and has a mass of just under 2000 kg. Figure 2.3 shows a schematic view of the detector's active science instruments. Two pairs of Čerenkov and Scintillation detectors sandwich a single wire proportional tube array. In total there are 1584 proportional tubes in the instrument, each 2 m long and 2 cm wide. The single wire proportional tubes are arranged in 16 layers. The layers are arranged in two perpendicular directions. This arrangement facilitates the trajectory reconstruction through the instrument. The proportional tube array comprises two parts: The upper eight layers of tubes are the dE/dX-array, while the lower eight layers are interspaced with four layers of radiator material to form the transition radiation detector (TRD).

The scintillation detectors serve as triggers and, in combination with the Čerenkov counters, measure the nuclear charge Z . The charge is determined at the top and the bottom of the instrument independently in order to ensure particles did not undergo charge-changing interactions within the instrument.

The energy measurement is conducted in three different energy regions: with the Čerenkov detector up to a few GeV/amu, with the dE/dX-array from about 10-500 GeV/amu, and with the TRD above 700 GeV/amu. Response functions and energy resolutions are given in Section 2.3. The TRD is expected to saturate at energies around 30,000 GeV/amu. Because of the steeply falling energy spectrum, the measurement is limited by counting statistics and not by saturation of the detector.

The instrument also includes various analog and digital electronic circuits to read out the detector subsystems, format, store and transmit the data, and receive commands from the ground. All electronics are optimized for low power consumption. As a whole, the instrument consumes less than 250 W of power, which is supplied by solar power using a photo voltaic array.

Most components of the detector, except some elements of the electronics, operate at an ambient pressure of a few mbar at float altitude. This creates a number of technical challenges, including the danger of corona discharge at the detector elements under high voltage, and local overheating of the electronics. The instrument's entirely passive thermal control is achieved using foam insulation and layers of aluminized mylar as sun shields.

The proportional tubes have an on-board gas supply and distribution system that allows for regulation of the gas pressure in flight. The proportional tube system of TRACER has a total volume of 1000 liters, which is segmented into 16 manifolds, each of about 60 liters. Three

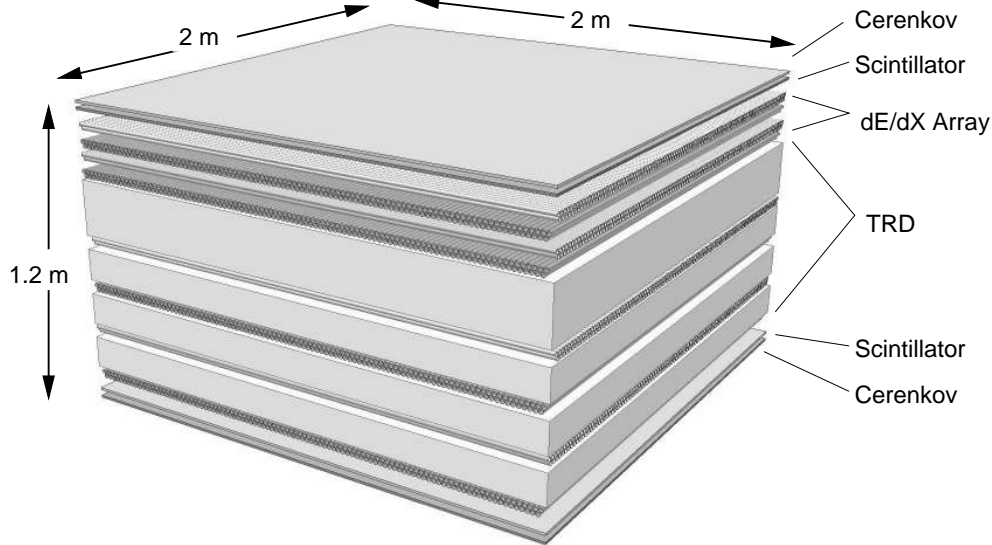


Figure 2.3: Schematic diagram of the active detector materials of the TRACER detector.

thousand liters of xenon-methane gas are carried on board as make-up gas in the event of small leaks during the flight, or, if required, to purge the entire system with new gas. The Xe:CH₄ gas mixture used is 95%:5% by volume at 1 atmosphere.

Scintillation and Čerenkov Detectors

The large geometric factor of TRACER requires similarly large scintillation and Čerenkov counters ($2 \times 2 \text{ m}^2$) to provide both, a trigger and a measurement of nuclear charge over the active area of the detector.

In order to achieve a relatively uniform response, and to keep the number of photomultiplier tubes (PMTs) moderate, each counter is divided into four quadrants and uses a wavelength-shifter bar readout, as shown in Figure 2.4. Each Čerenkov quadrant is made from one acrylic plastic sheet; each scintillator quadrant is constructed from two $1 \times 0.5 \text{ m}^2$ wide sheets of scintillating plastic. Each counter comprises 24 PMTs, so that each quadrant is seen by 8 PMTs. Every 12 PMTs share one high voltage supply, so that 4 PMTs per quadrant are on a separate HV channel.

The scintillating plastic is 0.5 cm thick, whereas the Čerenkov material is 1.3 cm thick. The Čerenkov material has a refractive index of 1.49 and is doped with a wavelength-shifting admixture that additionally disperses the Čerenkov light isotropically. Table 2.1 summarizes the detector components used in the scintillator/Čerenkov systems of the detector.

A fraction of the light that is emitted in the active part of each counter travels to the wavelength-shifter bars where it is absorbed and re-emitted isotropically. A fraction of this light again travels directly or via total internal reflection to the photomultiplier tubes. The scintillator system detects ≈ 40 photoelectrons for a singly charged particle at minimum ion-

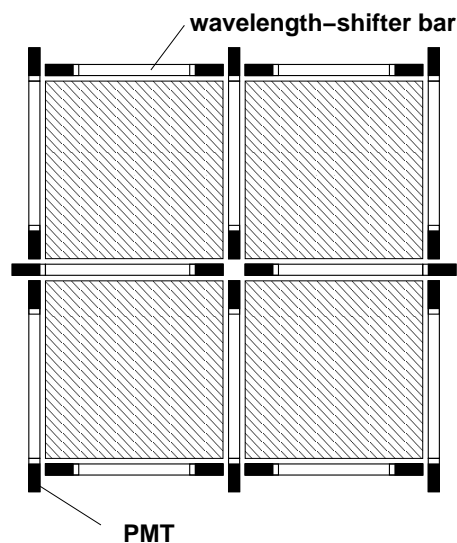


Figure 2.4: Schematic diagram of the scintillation and Čerenkov counters. Each quadrant is seen by 8 PMTs, 24 PMTs per counter mean a total of 96 PMTs are used in the instrument.

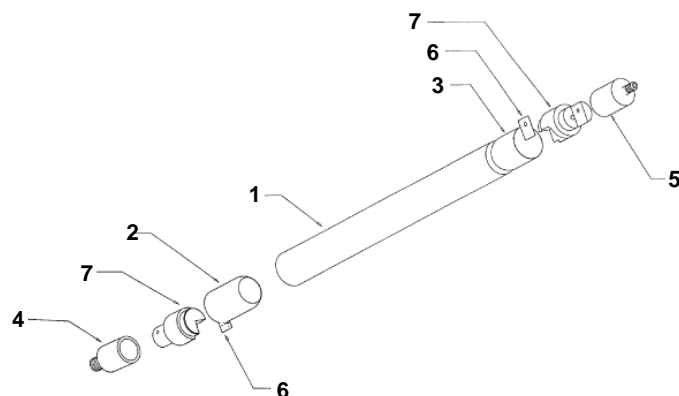


Figure 2.5: Proportional tube assembly drawing. (1) Mylar tube; (2), (3) modified cigar tubes to anchor assembly; (4) end-cap with o-ring groove and threaded neck to interface with gas manifold and HV distribution; (5) end-cap with hose barb; (6) G-10 pad for wire (7) wire holder.

izing energy, whereas the Čerenkov system detects ≈ 2 -3 photoelectrons for a singly charged particle in Čerenkov saturation.

Each scintillator PMT generates two signals, one from the anode, and one from the last dynode. The summed anode signals of all PMTs are used for the coincidence trigger. The dynode signals are amplified individually and analyzed with 12-bit accuracy by custom-built peak-detecting ADCs. The Čerenkov counter is not used in the trigger, and only the dynode signals are analyzed.

Proportional Tube Array

The 1584 single wire proportional tubes on TRACER are used to reconstruct the trajectory of an event through the instrument, and to provide energy measurements in the dE/dX -array and the TRD. The energy measurement relies on the signal created by the specific ionization of the gas by a traversing ion (i. e. cosmic-ray nucleus) and the additional ionization due to x-rays generated in the radiator material of the TRD. The proportional tubes are set up in 16 perpendicular layers of 99 tubes each. Each tube consists of a central wire, a conducting wall around it, and end caps that allow high voltage and gas feed through. The tubes must be gas-tight and transparent to x-rays.

The design is shown in Figure 2.5. The tube body ((1) in Fig. 2.5), is 2 m long, 2 cm in diameter, and is constructed from three layers of spiral wound Mylar. The inner layer is aluminized for conductivity.

To provide easy servicing of gas, high voltage and readout, the proportional tubes are

Table 2.1: Summary of components used in the scintillation and Čerenkov counters, as well as TRD fiber radiator parameters.

| Scintillator and Čerenkov components | | |
|---|---------------------------------|-----------------------------|
| Component | Type | Comments |
| scintillator | BICRON 408 (0.5 cm thick) | St. Gobain Inc. |
| Čerenkov | Polycast Acrylic (1.3 cm thick) | Refractive index $n = 1.49$ |
| wave-shifter bars | BC 482A | St. Gobain Inc. |
| PMTs | Photonis XP1910 | 19mm, 10 Stage |

| TRD radiator parameters | | |
|--------------------------------|-----------------------|---|
| Parameter | Thick Fibers | Thin Fibers |
| supplier | Hercules, Inc. | 3M Company |
| material | Herculon 101 | Thinsulate M400 |
| density | 40 mg/cm ³ | 45 mg/cm ³ |
| average fiber thickness | 17 μm | 2-5 μm (avg. 4.5 μm) |
| equivalent foil thickness | 0.0021 cm | 0.00045 cm |
| equivalent foil spacing | 0.038 cm | 0.01 cm |

connected to manifolds. Each manifold is 1 m wide and holds 99 tubes that are arranged in two closely packed layers. In total, 8 pairs of manifolds are required for the proportional tube array, each with an independent gas servicing system, and with its own high-voltage converter.

The gain along the 2 meter tubes was determined to be constant within 5%. At the very ends of the tubes the gain is slightly reduced due to inhomogeneities of the electric field close to the end caps, but this is not significant for the measurement of cosmic rays. Due to distortions in the support structure, additional gain variations were observed in the second LDB flight. They are described in section 2.4.

The proportional tube system is analyzed by track-and-hold AMPLEX chips [16]. Knowledge of the signal rise time is vital for these electronics. It is related to the electron drift time and depends on the gas mixture and high voltage. For the Xe:CH₄ gas mixture used, a maximum signal was measured to occur 1400 ns after trigger [49].

A dual-gain readout is used (see Section 2.2.1) for an extensive dynamic range. The overall dynamic range is limited by noise at the low end (10^{-15} C), and by the maximum signals possible before a proportional tube develops “limited streamers” ($\approx 5 \cdot 10^{-12}$ C). In practice, the proportional tube array can analyze signals for all nuclei from Be ($Z=4$) to Fe ($Z=26$). The electronics of the dual gain output provide more than 10^4 ADC channels for the measurement.

The TRD comprises four layers of plastic-fiber blankets as radiators above four double

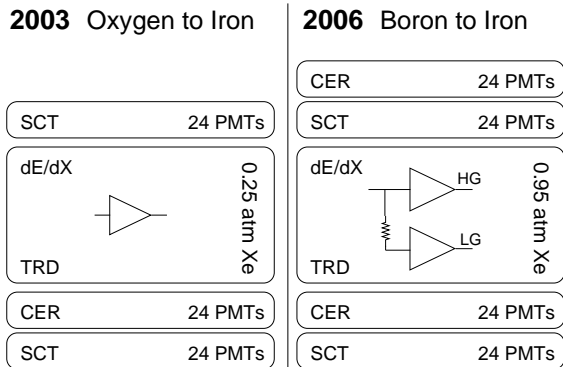


Figure 2.6: Comparison of detector configurations of 2003 and 2006 (SCT: Scintillation detector, CER: Čerenkov detector).

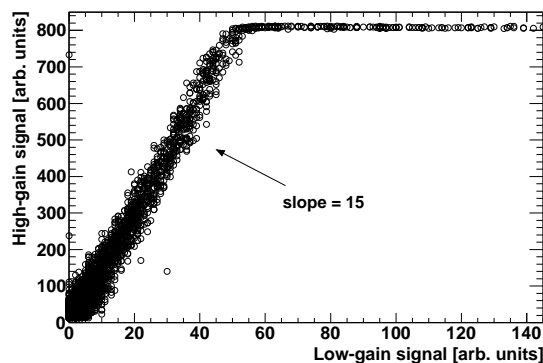


Figure 2.7: High-gain signal vs. low-gain signal for an individual proportional tube and events recorded in flight. The slope of the linear domain is about 15, then the HG signal saturates while the LG signal still increases.

layers of proportional tubes (for an overview on TRDs see [59, 88]). The radiators are the same as those used on CRN [52]; their components are summarized in Table 2.1. The top radiator, with a thickness of 17.8 cm, is somewhat thicker than the following three radiators (each 11.25 cm) in order to compensate for the lack of “feed-through” x-rays that may be generated but detected only after passing through more than one radiator/detector pair. This arrangement has proved to be useful for obtaining a uniform energy response of all detector layers in accelerator calibrations for the CRN instrument [52].

2.2.1 Upgrades for the 2006 Balloon Flight from Sweden

For the long-duration balloon flight of 2006, several upgrades were integrated into TRACER in order to facilitate the measurements of the light nuclei boron, carbon, and nitrogen. The dynamic range of the proportional tube system had to be extended, and the charge and energy resolution had to be improved. A schematic comparison is given in Figure 2.6, which highlights all important changes.

Extended dynamic range The useful dynamic range of one channel of the AMPLEX chip is of the order of a thousand. However, the measurement in the charge range from boron to iron requires an overall range of several thousand. This was achieved by providing the proportional tube system with a dual gain output. For this, the signal is split into two channels, of which one is attenuated resistively, as Figure 2.6 indicates. The read-out electronics had to be updated as well to accommodate twice as many channels, the “high gain” (HG) and attenuated “low gain” (LG) channels. Both sets of 1584 data channels are digitized to 10 bits. A ratio between HG to LG of about 15 (see Fig. 2.7) gives an overlap of about 6 bits and a nominal dynamic range of 13,000.

Improved energy resolution The energy resolution that can be achieved from the specific ionization measured in the proportional tubes is limited by statistical fluctuations of the signal. Hence, in order to reduce the fluctuations, and thereby to improve the energy resolution, an increase in the gas density in the tubes is necessary.

The gas used in the proportional tubes for the Antarctic flight was a 50%:50% mixture of Xe and CH₄ at a pressure of 0.5 bar. For the Sweden flight this was replaced by a 95%:5% mixture at 1 bar. This almost fourfold increase in Xe density increases the ionization signal also by a factor of four, and thus reduces statistical fluctuations by half. This improvement made energy measurements for the light elements boron and carbon possible, as will be described in Section 2.3.3.

Improved charge resolution A second Čerenkov detector was installed at the top of the instrument (identical in design to the bottom Čerenkov detector). This enabled a second independent charge measurement.

The two charge measurements at the top and at the bottom of the instrument enhance the redundancy and the resolution of the charge determination.

2.2.2 Geometric Aperture

The maximum geometric aperture of the detector, derived for a cube of the dimensions of the trigger geometry, is 4.73 m² sr. For the flux calculation a modified aperture has to be determined. Certain areas in the detector are defined as “blind regions”. They are the locations of the PMTs and a 1 cm border on either side of the wavelength-shifter bars to avoid edge effects and steep gradients in PMT responses.

Events passing through these regions cannot be accepted, so that the reduced aperture is given by

$$A_i = A \cdot 2\pi \int_{\theta=\pi/2}^0 P_D(\theta) \cos \theta \, d(\cos \theta), \quad (2.1)$$

where A is the area of the instrument (206 cm × 206 cm) and P_D is the probability of detection for a given angle θ . In this equation $P_D(\Theta)$ is evaluated by averaging over all azimuth angles and all lateral positions of events. This way the calculation of the aperture can be reduced to the given integral over $\cos \Theta$.

The detection probability is evaluated by a Monte Carlo simulation under consideration of the conditions that a particle needs to produce a trigger (i. e. hit both scintillation detectors) and avoid blind regions in the detector from simulated events uniformly distributed in lateral position and azimuth angle. The detection probability $P_D(\Theta)$ is found as the ratio of detected particles to the total number of injected particles ordered by zenith angle.

The detection probability for vertical incident particles is 98%, the maximum zenith angle Θ detectable is about 60°. The effective aperture of TRACER is 3.85 m² sr.

2.3 Energy Response and Resolution

2.3.1 Response of the Čerenkov Detector

At a few GeV/amu, the energy measurement relies on the Čerenkov detector. A particle traversing the detector emits a cone of Čerenkov light if its energy is above the Čerenkov threshold. The acrylic Čerenkov material has a refractive index $n = 1.49$, which corresponds to a threshold Lorentz factor of $\gamma = 1.35$ ($\beta = 0.67$) or a kinetic energy of 0.33 GeV/amu. Below this energy, some light is produced by residual scintillation in the plastic sheet; above the threshold the signal S_c increases rapidly [62] according to:

$$\frac{S_c}{Z^2} = \frac{C_0}{1 - 1/n^2} \cdot \left(1 - \frac{1}{n^2\beta^2}\right), \quad (2.2)$$

before it saturates towards the asymptotic value C_0 . The signal is proportional to the square of the charge of the particle Z^2 .

In both Čerenkov counters, additional light is produced by δ -rays, or “knock-on” electrons. These electrons are produced in the Čerenkov material itself and the material above. As shown in Figure 2.8, the bottom Čerenkov detector is more affected by δ -ray contributions than the top Čerenkov detector, simply because there is much less material above the latter. The effect of δ -rays on the Čerenkov signal has been studied in simulations [42] and was confirmed using the data themselves. The response curves are parametrized and used for the analysis as shown in Fig. 2.8.

2.3.2 Response of the dE/dX-array and the Transition Radiation Detector

Above about 10 GeV/amu the signal from the proportional tubes is used as an energy measure. Up to about 700 GeV/amu all tubes measure the same signal S_e , which is proportional to the energy deposited by the traversing particle in the tubes [62, 73]:

$$S_e \propto -\frac{dE}{dx} = \frac{KZ^2}{\beta^2} \left[\ln \left(\frac{2m_e c^2 \beta^2 \gamma^2 T}{I^2} \right) - \beta^2 \left(1 + \frac{T}{T_{\max}}\right) \right], \quad (2.3)$$

with $K = 2\pi r_e^2 m_e c^2 n_{el}$, the classical electron radius r_e , the electron rest-mass energy $m_e c^2$, the electron density of the material n_{el} , the mean excitation energy of the material I , the maximum electron energy absorbed T , the maximum energy transferable to an electron T_{\max} , and the particle’s charge Z , speed β , and Lorentz factor γ .

Equation (2.3) is the restricted energy loss of a particle based on the energy loss due to ionization (Bethe-Bloch formula), neglecting the density effect and restricting the absorbed energy in the tubes to a maximum of T . The density effect and the restricted absorbed energy both lead to a saturation of the signal, which is not observed in the energy region of this measurement.

The signal is proportional to Z^2 , falls steeply below $\gamma = 3.97$ (energy of minimum ionizing particles, MIP), then rises slowly and is linear in $\log(\gamma)$ -space for $\gamma > 10$. This rise is referred to as the relativistic rise and is used as a measure of energy in the dE/dX-array.

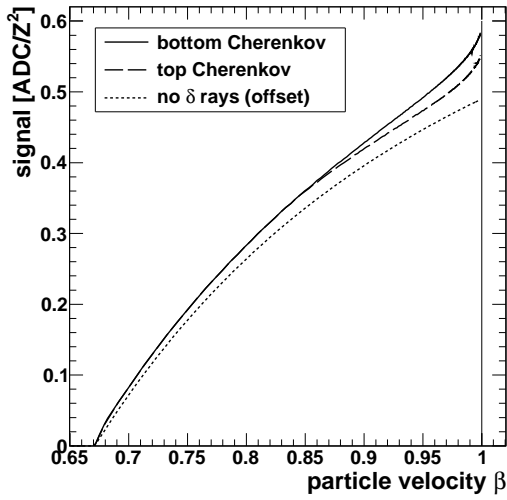


Figure 2.8: Response function S_c/Z^2 of the Čerenkov detectors as a function of particle speed $\beta = v/c$. Bottom and top detectors have different responses due to δ -rays. The analytical Čerenkov response is shown as the dotted line (offset for clarity).

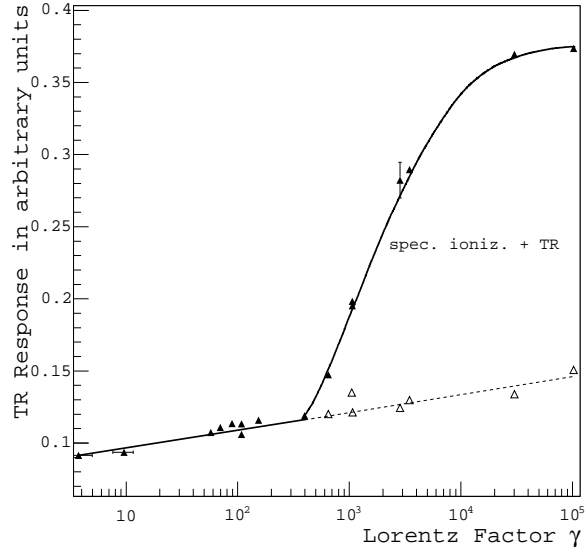


Figure 2.9: Calibration measurements of the CRN TR detector (reproduced from [12]). Signal in the multi-wire proportional chambers as a function of particle energy. This calibration is valid for TRACER, see text.

The relativistic rise in the signal from $\gamma = 10$ to $\gamma = 440$ is found to be $33 \pm 2\%$, in agreement with the value used by the CREAM collaboration for the same detector configuration [55]. The signal function is shown in Fig. 2.10. In the normalization used here the energy of minimum ionizing energy loss, corresponding to $\gamma = 3.97$, is at $S_c/Z^2 = 3.07$.

Above a Lorentz factor of about 700, transition radiation is produced in the radiators of the TRD. Then the ionization signal is superimposed by the TR signal.

The photon energy of transition radiation (TR) typically peaks around 10 keV [21, 22]. The energy threshold above which TR is produced, the steepness of the TR signal increase with particle energy, and the energy at which it saturates depend strongly on the actual realization of the detector. Both, the number and the spacing of the foils (or fibers), are equally important as the gas mixture for detecting the TR photons (see [82]).

In general, the TR signal is proportional to the square of the incident particle's charge Z^2 , becomes observable at Lorentz factors of about 500 to 1000, and saturates below $\gamma \approx 10^5$. It is noteworthy that the TRD response can be fully calibrated with light particles (electrons, pions, etc.) at accelerators even for highest Lorentz factors. This is a distinct advantage compared to measurements with calorimeters, which must rely on simulations for calibration.

The TRD used on this instrument employs the same radiator configuration as CRN. For the long-duration balloon flight in Antarctica 2003 the same gas mixture was used, so that the CRN calibration [52] was valid. The calibration curve is shown in Fig. 2.9. For the flight in

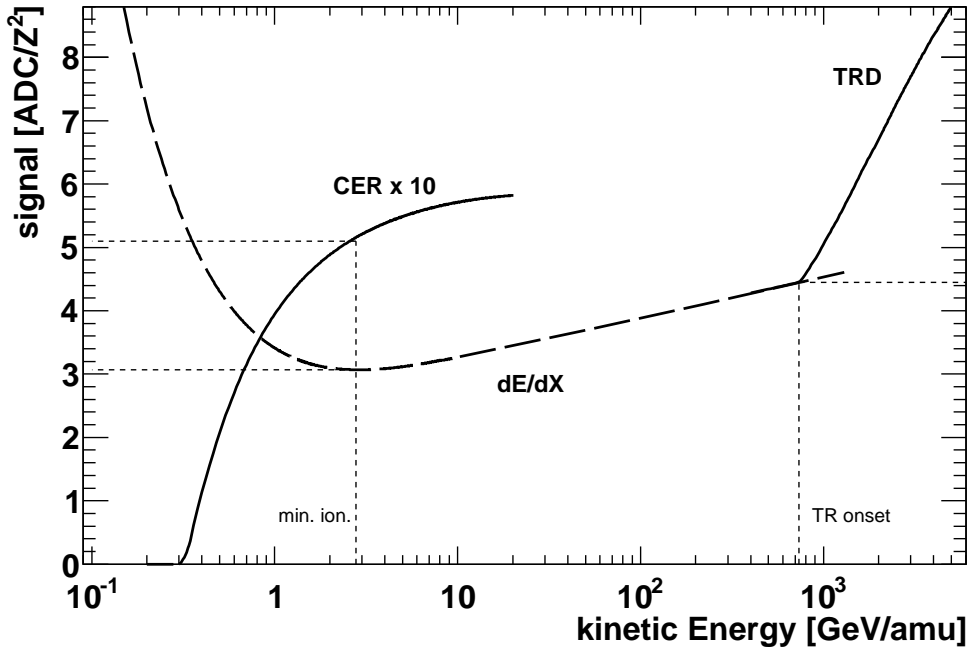


Figure 2.10: Response functions, normalized by Z^2 , of sub-detectors that are used for energy measurement. The natural normalization of the signals shown here is used throughout the analysis. Minimum ionizing energy ($\gamma = 3.97$) is at 3.07 in dE/dX signal and at 0.51 in the bottom Čerenkov signal per Z^2 . TR onset ($\gamma = 785$) is at 4.45 in dE/dX and TR signal per Z^2 . The normalization of the Čerenkov signal is multiplied by 10 for clarity.

2006 from Sweden, the calibration has to be modified due to the different gas mixture used (see Section 2.2.1).

Because of the higher Xe content in the proportional tubes, more TR x-rays are absorbed. This increases the TR signal, but the ionization signal also increases. Using data from [82], the overall effect of the gas change is estimated to be a relative reduction of TR signal by $19 \pm 3\%$ compared to the CRN calibration [52].

Furthermore, this relative signal attenuation shifts the TR onset energy to a higher value. TR onset is found at a dE/dX signal $S_e/Z^2 = 4.45$, which corresponds to a Lorentz factor of $\gamma = 785$ or to an energy of $E = 735$ GeV/amu.

The TRD response function is shown together with the dE/dX -array and bottom Čerenkov response in Figure 2.10.

2.3.3 Energy Resolution

The signals of all detectors used for the energy measurement scale with Z^2 of the incoming particle. This means that the relative statistical signal fluctuations decrease like $1/Z$ for all sub-detectors. Thus, the best energy resolution is achieved for heavy elements.

For the proportional tube system, the relative signal fluctuations σ_S have been determined with data recorded during flight for elements from boron to iron. This was achieved by se-

lecting elements with a preliminary charge estimation and then use the signals of other sub-detectors to roughly estimate the energy for which the fluctuations have been determined. The signal fluctuations can be modeled as a superposition of statistical and systematic contributions by:

$$\sigma_S = \sqrt{\frac{a^2/Z^2 + b^2}{n}}, \quad (2.4)$$

with parameters for the proportional system $a = 1.26 \pm 0.04$ and $b = 0.144 \pm 0.007$, and number of tubes n , which is 16 for the dE/dX-array and 8 for the TRD. Thus, the signal fluctuations in the dE/dX-array are a factor $\sqrt{2}$ smaller than in the TRD, but the resulting energy resolution is still worse due to the shallow relativistic increase of the ionization signal with energy. The parameter b corresponds to a systematic contribution to the signal fluctuations of about 2.5% for the whole proportional tube array due to uncertainties in the trajectory reconstruction. The signal fluctuations in the dE/dX-array for oxygen are for example $5.3 \pm 0.2\%$.

The signal fluctuations for the Čerenkov detector were estimated in an analogous way, using a different set of sub-detectors for the selection of the data sample. The signal fluctuations also follow Eq. (2.4) (with n fixed to 1) since the Čerenkov signal scales with Z^2 . For oxygen the relative signal fluctuations in the Čerenkov counters are 8%.

The uncertainty in the signal fluctuations translates into an uncertainty in the measured cosmic-ray fluxes. This is taken into account for the measured energy spectra in Chapter 6. In the following the signal fluctuations are used to determine the energy resolution of the three sub-detectors of the instrument. The energy resolution σ_E is derived from the signal fluctuations and therefore also has the form

$$\sigma_E^2 = \frac{a'}{Z^2} + b'. \quad (2.5)$$

Since each sub-detector in the instrument has a different energy response, the energy resolution must be calculated for each detector individually.

Using a $\pm 1\sigma$ interval in signal, the $\pm 1\sigma$ interval in energy ΔE is found from the response functions. The energy resolution is then defined as $\Delta E/2E$ and is shown in Figure 2.11. The resolution is very good for the Čerenkov (at 1 GeV/amu) and TR (at 1500 GeV/amu) detectors with values about 3% and 7% for iron, respectively. For boron their resolution is 13%. The dE/dX-array suffers from the very shallow relativistic rise but still gives a usable resolution between 10 and 500 GeV/amu of about 30% for iron or 55% for boron.

The upgrades to the proportional tube system for the Sweden flight (2006) enhanced the energy resolution in the proportional tube array significantly. This is illustrated in Figure 2.12 for the dE/dX-array around 100 GeV/amu by the fit results to the measured energy resolution as a function of charge. For light elements the improvement is about a factor of 2, but it is smaller for iron where systematic effects of the trajectory reconstruction are more dominant.

This improvement is necessary to make energy measurements in the dE/dX-array possible for boron and carbon.

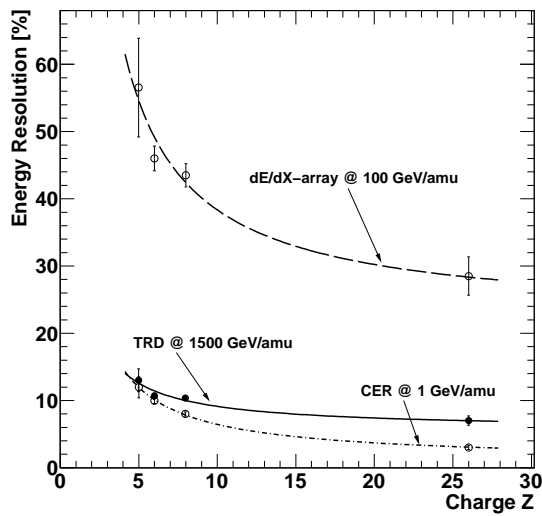


Figure 2.11: Measured energy resolution (1σ) of individual detector subsystems vs. charge Z for typical energies. The resolutions develop as $1/Z$ with charge with a systematic offset, see Eq. (2.5).

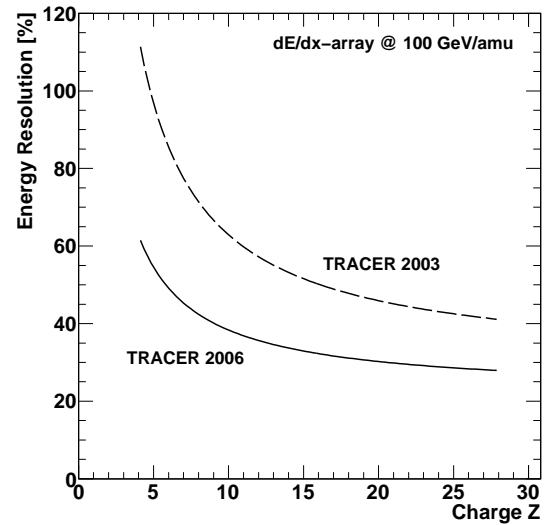


Figure 2.12: Parametrizations of measured energy resolutions for flights in 2003 and 2006 for the dE/dX -array. The enhancement of the energy resolution due to detector upgrades becomes clear, especially for light elements where statistical fluctuations dominate.

2.4 Detector Performance and Status

During each flight, there was no indication of a deterioration of the performance of the proportional tubes, due to gas poisoning, for the duration of the flights. This is in contrast to measurements on the ground, where amplitude and resolution of the signals deteriorate noticeably on a scale of 1-2 days. This happens as oxygen diffuses into the proportional tubes and acts as a quenching agent. This result is of practical importance if flights of much longer duration are anticipated: There seems to be no need for gas-purging at the time scales of at least a few weeks except for the provision of make-up gas to correct for minor leaks.

During the Sweden flight (2006), the instrument (Fig. 2.13) functioned well. All electronics, data acquisition, flight computer, data storage, telemetry, power system, batteries, etc. performed as expected.

After 1.5 days of flight, a subset of 12 PMTs in the bottom scintillator had to be deactivated due to an electrical discharge. For the remainder of the flight each quadrant of the bottom scintillation detector was viewed by 4 instead of 8 evenly distributed PMTs. This had only a minor impact on the instrument's performance.

At about the same time, seven PMTs in one half of the top Čerenkov detector failed. The face plates of these PMTs ruptured and rendered them unusable. It is noteworthy that all PMTs in the top Čerenkov that failed this way belonged to a new batch of PMTs (Photonis XP1910) acquired for this flight. Two of the four quadrants of the top Čerenkov counter were affected and as a consequence are avoided during analysis. This part of the data is termed selection C

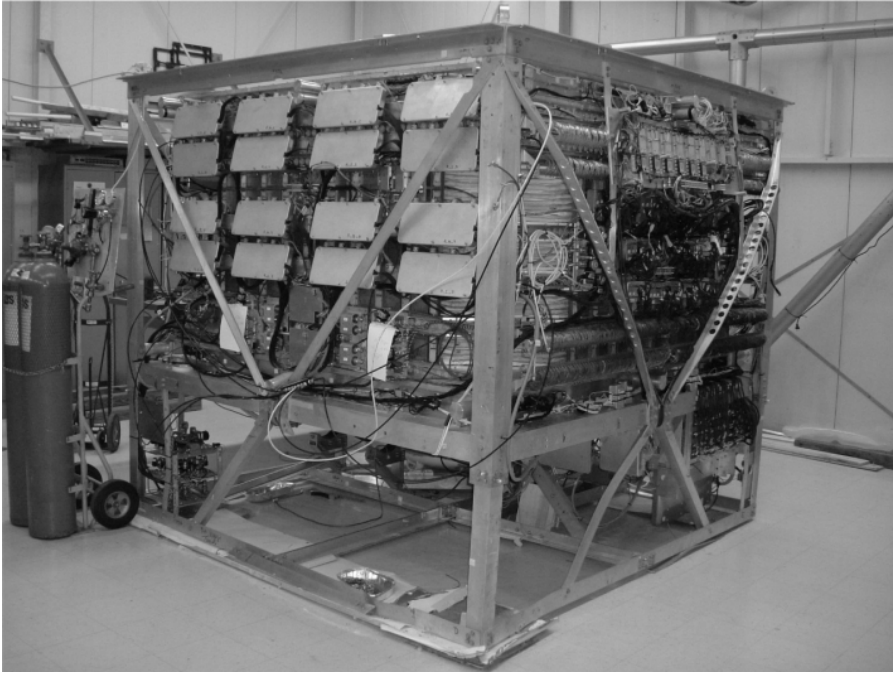


Figure 2.13: The TRACER detector after its recovery from Canada in 2006 at the University of Chicago.

(SelC, see Section 2.5).

Later in flight, one PMT in the top Čerenkov counter produced a visible discharge for about 4 hours as ambient air was leaking through its damaged face plate. This generated a background signal that can be seen in all active PMTs of the counter. The top Čerenkov data taken during the time of the discharge are rejected.

The proportional tube system performed without significant problems during the whole flight.

After the flight, a complete test was performed. The original flight read-out electronics were found to be in good shape after the landing. All proportional tubes were supplied with high voltage and Ar:CH₄ gas, then tested with a radioactive ⁵⁵Fe source (x-ray energy: 6 keV).

For 25 tubes, a broken low-gain AMPLEX channel was discovered both in the lab test and in the data. These tubes are only used in the analysis if the signal is in the high-gain regime.

Of the 1584 single wire proportional tubes of the detector, 91 could not be used in the data analysis for the following reasons:

20 tubes were found to produce no signal, 3 tubes showed an abnormal high-gain to low-gain ratio despite working electronics.

The largest portion of deactivated tubes are 52 tubes whose gain drops at exactly half the tube length to zero. Examination of one such tube showed that the conductive aluminum layer on the inside was scorched away by an electrical discharge. This isolated one half of the tube from high voltage and thus caused the gain to drop to zero. Such discharges happen at the center of the tubes, because there the center wire is closest to the tube wall if the tube is bent.

Another 16 tubes had to be omitted from data analysis because of very large gain variations

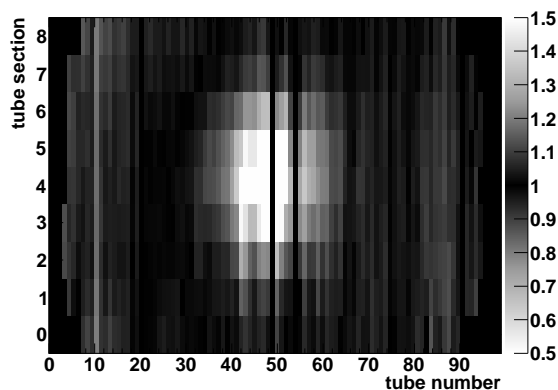


Figure 2.14: Gain-correction factors derived from oxygen data for layer 6 of the proportional tube system (99 tubes). Each tube is sectioned into nine 22 cm parts.

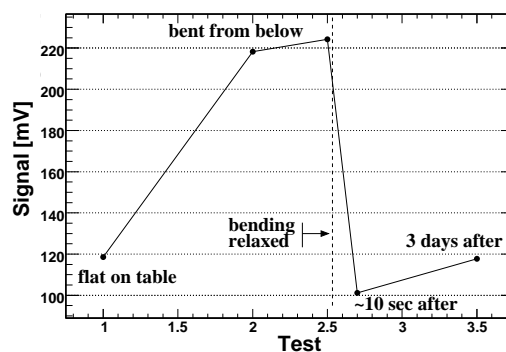


Figure 2.15: Test result of a tube in the lab. The signal from a radioactive ^{55}Fe source is shown for different test setups (signal uncertainty about 30%). The tube quickly recovers and maintains its original gain level after a pressure point was released.

along the tubes. Several areas with enhanced tube gains (termed “hot spots”) were found in layers of proportional tubes, as shown in Fig. 2.14.

The “hot spots” have been found consistently in data of the flight for different elements (carbon to iron), in pre-flight muon data, and after the flight in laboratory tests. The relative signal increase in these areas compared to normal tube gains was of the order of 50%, with some extreme cases of a 250% enhancement. The gain variations are stable in time during the whole flight.

It was shown that these gain variations are due to uneven support of the tube manifolds resulting in pressure points or bending of the tube body. The gain level recovers instantly when the position is corrected. Figure 2.15 shows a tube signal recovering from a pressure point applied in a lab test. This is important especially in the light of a possible future flight of the instrument.

Consistent correction factors in the form of gain maps have been derived from oxygen and iron data for all tubes in 9 sections (22 cm long) along each tube. They are shown in Fig. 2.14 for layer 6. They represent the ratio of the signal in a tube section to the average signal in all tubes excluding “hot spots”. After correction the tube gains of all tubes in all sections are equal within 5%.

The TRACER detector is currently residing at the University of Chicago and has the possibility to be refurbished for another flight.

2.5 Description of the Data of the Sweden Flight

For each event, the signals from all PMTs are recorded. To minimize the size of each event, a zero-suppression system is utilized for the proportional tubes. Only signals above a threshold

value are stored. Hence, individual events have variable length (4-8 kbits).

TRACER monitors the pressure in each manifold, the temperature of critical components, high-voltage levels, counting rates from the discriminators, coincidence circuit, master trigger, as well as the status of each disk, storing them in “housekeeping” events.

All events (data and housekeeping) are assembled in custom made electronics. The data are processed by the on-board CPU for storage on a hard disk, and are also sent to the telemetry transmitters. Data are recorded on-board (including housekeeping) using multiple SCSI disks.

In the five-day flight, 50 GB of compressed raw data at an event rate of about 120 Hz were gathered. With a dead time of the data acquisition of 17.7% and some gaps in the data taking due to maintenance the overall active lifetime of the instrument was 203200 s (2.4 days).

The final data analysis was performed for three distinct parts of the data set. Selection A (SelA) is data from the first 1.5 days of flight, during which the detector performed in its starting configuration. Selection B and C (SelB, SelC) represent the data after PMTs in the top Čerenkov detector and the bottom scintillator failed (see 2.4). In SelB the undamaged part of the top Čerenkov is used, while SelC is analyzed without the top Čerenkov signal.

The relative sizes of the data parts are 20%, 40%, and 40%, respectively. The different detector configurations of these parts affect only the charge analysis. SelA yields the best charge resolution, but SelB’s shortcoming is only minor, as the Scintillation detector was designed to cope with this kind of failure. A quality cut that ensures a minimum of three PMTs detect an event in a quadrant, is used to ensure data quality in SelB and SelC. The efficiency of this cut is almost 100%.

For SelC, the top Čerenkov detector is not used and the bottom Čerenkov is instead used in combination with the top scintillator to provide a charge measurement. For these data the charge resolution is decreased somewhat, but the data can still be used.

In the final analysis, the efficiencies of quality cuts and the charge selection that are affected by the changed detector configuration are evaluated separately for the three data selections A, B, and C. The data could then be used together with a weighted average of these efficiencies.

Before the flight, the instrument recorded muon events on the ground. In order to generate usable signals from these singly charged particles the high voltages supplied to the PMTs and proportional tubes were increased. These pre-flight muon data are used in the later analysis to construct lateral signal response maps for the scintillation and Čerenkov detectors (see Section 4.4) and to investigate signal fluctuations in the proportional tubes.

CHAPTER 3

SUMMARY OF PREVIOUS RESULTS FROM TRACER

In 2008 and 2009, measurements of the first long-duration balloon flight of primary cosmic-ray elements [12] and an interpretation of these results [13] were published. These measurements represent the most comprehensive data on heavy primary Galactic cosmic rays to date. The measurements include the individual elemental energy spectra up to 10^{14} eV per particle for O, Ne, Mg, Si, Ar, Ca, and Fe, and are shown in Figure 3.1 together with data from space missions HEAO [27] and CRN [60]. The TRACER measurements exceed the previous data by at least one order of magnitude in energy. Recently data were published by the CREAM experiment [5] that confirm the spectra, although they do not reach as high in energy.

The measurements narrowed the gap between direct and indirect methods, but do not yet close it. The gap between the direct TRACER data [12] and indirect air-shower data from KASCADE [9] or EAS-TOP [63] is less than a decade. More exposure is needed to generate the desired overlap between these two complementary techniques

A simple power-law fit to the observed energy spectra from TRACER yields a common power-law index of 2.65 ± 0.05 [12], without noticeable dependence on the elemental charge Z . This hints towards a shared origin of these cosmic-ray elements.

A more detailed study was carried out in [13] in order to investigate the propagation of cosmic-rays and properties of their sources. Therefore, a Leaky-Box model of cosmic-ray propagation (see Section 1.3) was used that also takes into account secondary production of lighter elements from their heavier parents. The propagation index δ was assumed to be 0.6 for this analysis. The propagation model was fit to the TRACER data and it describes the data well. The result of this procedure is an estimate of the source abundances n_i , the source spectral index α and the residual pathlength Λ_0 (see Eq. (1.9)).

The fit result for α and Λ_0 is shown in Figure 3.2 as a likelihood map of the combined fit over all elements. The best fit values are at $(\alpha, \Lambda_0) = (2.4, 0.3 \text{ g/cm}^2)$, but these values are ambiguous, especially for Λ_0 , as can be seen by the long valley in the likelihood map. Although soft source spectra are favored ($2.35 < \alpha < 2.45$, 3σ contour), the residual pathlength Λ_0 is not well constrained.

The source abundances found with the TRACER data, using the best fit values for α and

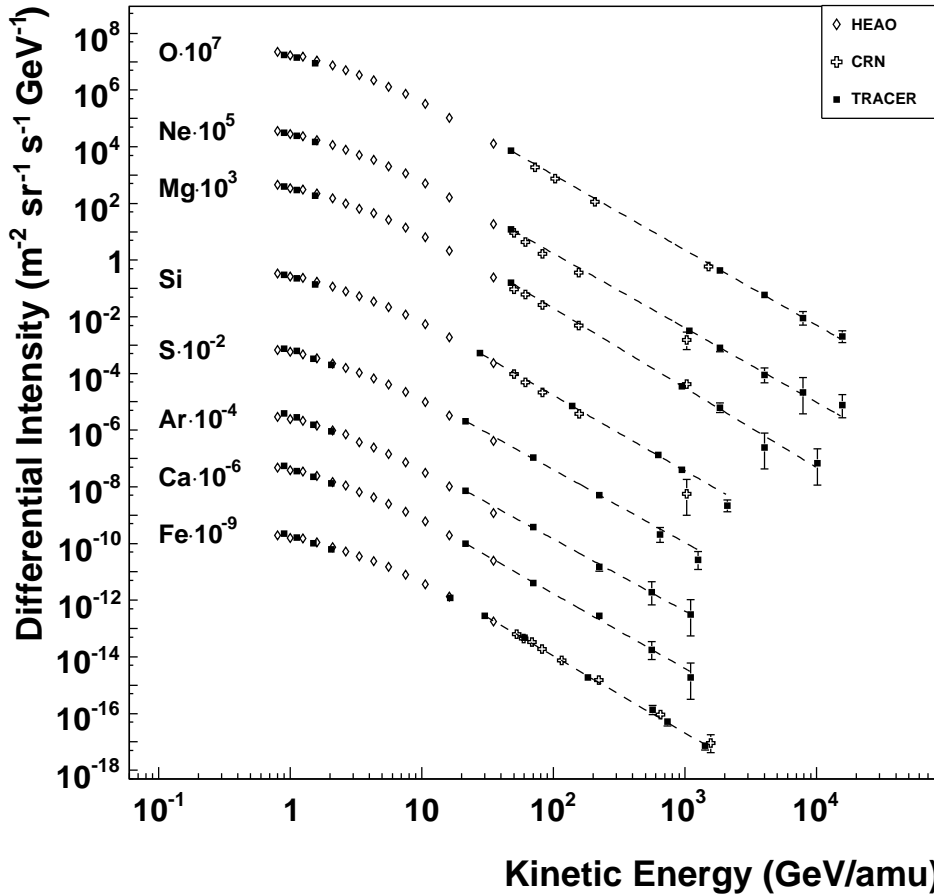


Figure 3.1: Differential energy spectra of eight primary cosmic-ray elements ($Z = 8$ to 26) as measured by TRACER [12] compared to HEAO [27] and CRN [60]. The dashed line is a common power-law fit yielding a spectral index of 2.65.

Λ_0 from above, are shown in Figure 3.3 and compared to previous measurements. The values agree with the abundances observed at low energies and also show the same correlation with condensation temperature. Elements with high condensation temperature seem to be efficiently accelerated, maybe because they are efficiently injected into the acceleration site as they form dust grains [26, 57]. The relative cosmic-ray abundances are also correlated with first ionization potential and some ambiguity remains over which correlation represents the true one.

The soft source spectrum suggested by the TRACER data is not easily accommodated by first-order Fermi acceleration at strong shocks, which predicts a source spectral index of about 2. More complex shock acceleration models are needed that can produce soft source spectra (see for example [46] and references therein).

The TRACER measurement of the Antarctic flight in 2003 represents the most detailed data on the energy spectra of heavy primary cosmic-ray elements to date. For the first time, the source index α could be estimated in a self-consistent model including the Galactic propagation of cosmic rays. The source index $\alpha \approx 2.35$ is also discussed in Chapter 7.

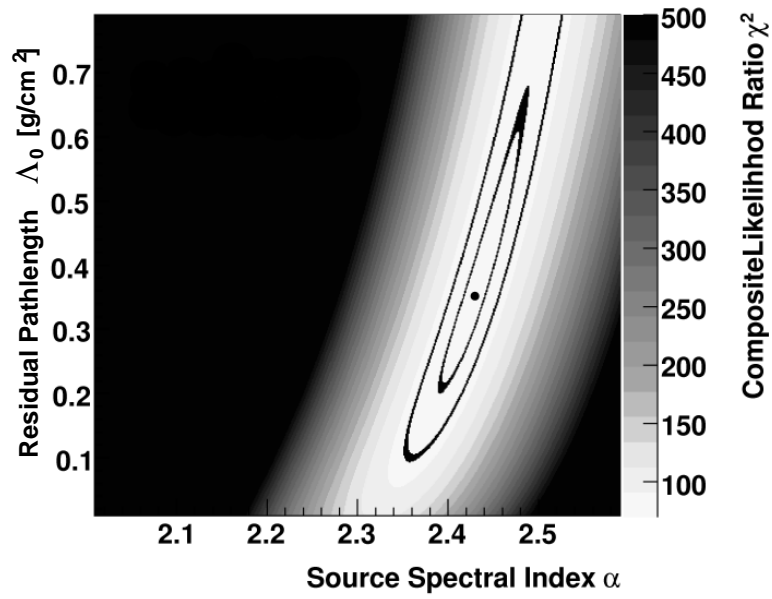


Figure 3.2: Likelihood map in the parameter space of residual pathlength Δ_0 and source spectral index α . Result of a combined fit to eight primary cosmic-ray elements from O to Fe. 1σ and 3σ contours are indicated around the best fit value.

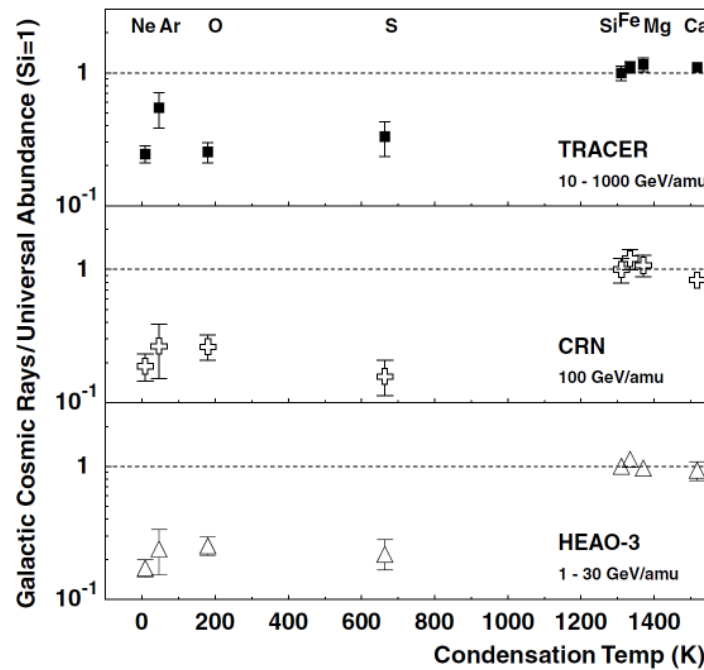


Figure 3.3: Relative abundances of Galactic cosmic-ray elements compared to the solar-system abundances as a function of condensation temperature. The TRACER data agree with previous measurements at lower energies (HEAO [27] and CRN [60]) and show a correlation with condensation temperature.

CHAPTER 4

SIGNAL RECONSTRUCTION FROM RAW DATA

This chapter is concerned with the analysis steps that prepare the initial data from the Sweden flight of TRACER for charge and energy measurement. Corrections to the data have to be found and applied. This process relies strongly on iterative procedures and is performed with muon data taken before flight as well as data of heavy nuclei taken during flight. This makes it tedious to describe the analysis steps in a chronological order. Instead, each section is concerned with a particular signal correction or aspect of the raw data analysis, which together form the iterative process.

An illustration of the analysis chain is shown in Fig. 4.1. After a first level trajectory reconstruction, lateral response maps are derived for the scintillation and Čerenkov detectors from muon data. Also, several operations are done concerning hardware properties: finding dead proportional tubes and PMTs, correcting tube positions, correcting for non-linearities in ADCs, and unifying high-gain and low-gain signals from the proportional tubes onto one scale. After an iteration of this procedure, a preliminary crude charge estimation helps to isolate mostly pure elemental samples, which are used to derive gain corrections for PMTs and proportional tubes, and to generate lateral response maps from data. Then a second level trajectory reconstruction refines the previously found trajectory, after which the whole chain is repeated. The corrected signals for data analysis can then be generated, from which the charge and energy of every event is determined.

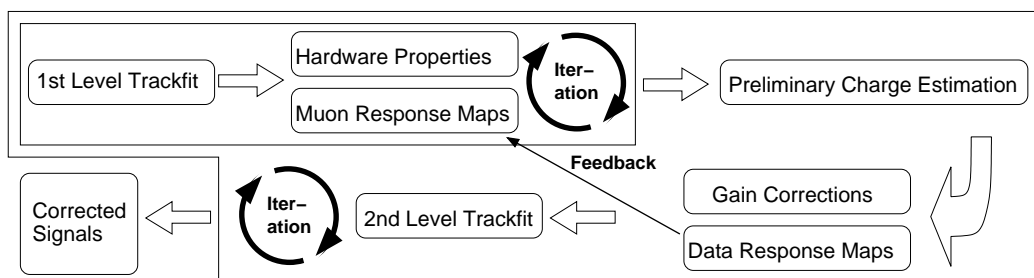


Figure 4.1: Analysis chain from initial data to corrected signals.

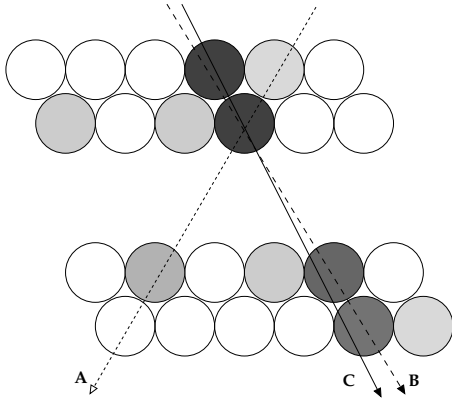


Figure 4.2: Schematic illustration of the first-level tracking fit. Darker tubes represent higher signal. Track A is considered by the fit, but rejected. The true trajectory is found, but tracks B and C cannot be distinguished within the resolution limits.

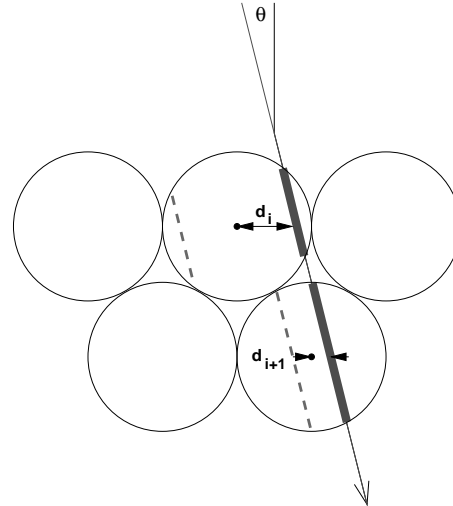


Figure 4.3: Illustration of the second-level tracking fit. Distances d_i of the true trajectory from the tube centers are estimated with the tube signals and define two possible tracks through each tube. These tracks are then arranged to the true trajectory.

4.1 Trajectory Reconstruction

4.1.1 First Level

The first-level trajectory reconstruction identifies the particle's trajectory through the TRACER instrument. The fit looks for combinations of tubes with a signal above threshold that are aligned in a straight line. The signal amplitudes in the individual tubes are not used in the fit but only the tube positions and the information that it was hit.

The trajectory in three dimensions is defined by two independent linear fits in two perpendicular projections. Therefore, the signals of up to 8 tubes hit in each projection are fit independently.

All combinations of three or more tubes are fit and the four best tracks are stored. The best trajectory is accepted as the true one. It is defined by the smallest χ^2 value of the fits and the largest number of tubes hit along the track.

For light elements most events are found to have only one acceptable trajectory, because only a few proportional tubes away from the track have spurious signals above threshold. In the case of iron, however, many knock-on electrons (δ -rays) are produced in the instrument, which produce signals in tubes close to, and sometimes farther from, the true trajectory. In this case many possible tracks are found, but they are easily rejected with the summed signal heights, which are very large for the iron nucleus and thus for the true trajectory. Misidentification of tracks was found to be less frequent than one in a thousand.

The lateral uncertainty of the first-level tracking fit is much smaller than the size of a tube

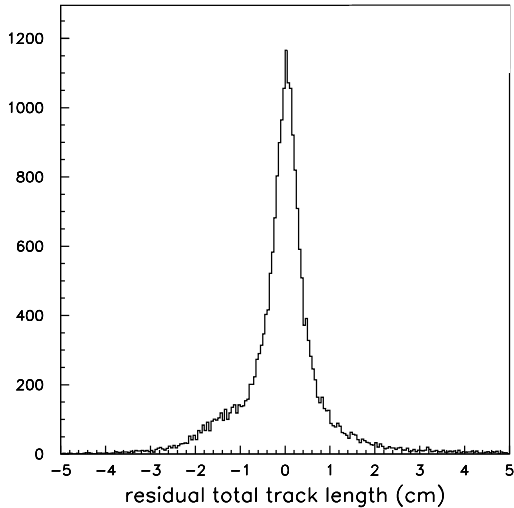


Figure 4.4: Study of the tracking quality by MC simulation. The residual track length distribution determines the uncertainty to 3%.

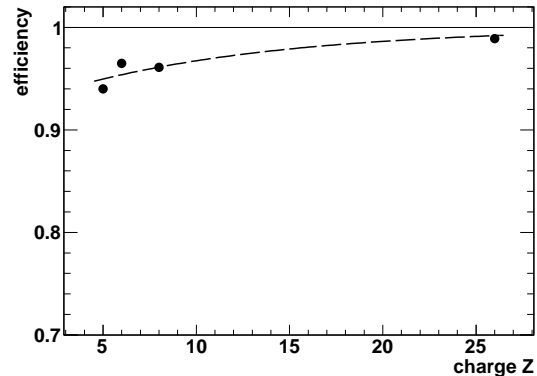


Figure 4.5: Efficiency of the second-level trajectory reconstruction as a function of charge.

radius; it is about 5 mm. Figure 4.2 illustrates how the resolution is limited by the tube radius.

For 4.6% of triggered events no trajectory could be found. Thus, the efficiency after the first level trajectory reconstruction is 95.4%. This was found to be the same for all elements from boron to iron. This can be expected, because the reconstruction follows a purely geometrical procedure without use of the signal amplitudes.

4.1.2 Second Level

The second-level trajectory reconstruction refines the result of the first-level track fit by utilizing the signal amplitudes in the tubes. The signals are proportional to the energy loss in the tube, ΔE , and hence to the length of the track through a tube. The distribution of track lengths for each event is used to determine the distance of the particle's trajectory from the tube centers (impact parameter d_i) as illustrated in Fig. 4.3. Note that each impact parameter defines two possible track positions through a tube, so that a fit is carried out to find the most suitable linear function through all track segments in all layers. This is done in the two perpendicular projections independently.

The important parameters inferred from the reconstructed trajectory are the total track length through the proportional tubes and the lateral position of the event in the four scintillation and Čerenkov detectors. Also the zenith and azimuth angles are determined from the trajectory. The refined fit is more precise than the first-level fit. A Monte Carlo study has shown the total track length to be precise to 3%. This corresponds to an uncertainty of 2 mm in lateral position. The result of the MC study is shown in Fig. 4.4 as the distribution of the residual track length of the reconstructed trajectories.

The second-level trajectory reconstruction treats the signal fluctuations in the tubes as Gaussian. In general the fluctuations of energy loss are Landau fluctuations. However, be-

cause boron has a charge $Z = 5$ and therefore ionization is 25 times more intense as for singly charged particles, the fluctuations for heavy nuclei are symmetrical and can be treated as Gaussian.

The efficiency of the second-level trajectory reconstruction is 94.0% for boron and increases to 98.9% for iron, as can be seen in Figure 4.5. It is found by comparing the number of events with successful first-level trajectory reconstruction with the number of events with successful second-order trajectory reconstruction. In rare cases the impact parameters can not be assembled to a consistent trajectory, so no second-level trajectory is found. This is more likely for smaller signals, so the efficiency is slightly charge dependent (see Fig. 4.5).

4.2 Combining High-Gain and Low-Gain Proportional Tube Signals

For the proportional tubes both, high-gain (HG) and low-gain (LG) channels are digitized to 10 bits. Their ratio is about 15, meaning that a signal in HG bin 600 can be found in LG bin 40.

Both signal channels suffer from a slight nonlinearity above ADC bin 500 intrinsic to the AMPLEX signal processor [16]. This is taken into account when combining the signals into one scale for a continuous analysis. Thus, the resulting scale has three regions: the HG channel is used for signals in its linear regime (i. e. $ADC_{HG} < 500$). For higher signals the LG channel is used. For still higher signals the LG signal is corrected for ADC non-linearity.

In the second region the LG signal is mapped onto the HG scale for every tube i linearly:

$$ADC_{HG} = \alpha_i \cdot ADC_{LG} + \delta_i, \quad (4.1)$$

where the scale factor α_i is about 15 and a small offset δ_i compensates different zero-offsets. These parameters are determined for each tube.

In the third region this linear mapping is combined with a correction for ADC non-linearity above an ADC value of $ADC_0 = 500$

$$ADC_{\text{corr}} = \frac{ADC}{1 + \beta(ADC - ADC_0)}, \quad (4.2)$$

with the non-linearity parameter β , which is assumed to be the same for all tubes.

A unified scale for the tube signals S_t can therefore be constructed as:

$$S_t = \begin{cases} ADC_{HG}, & ADC_{HG} < ADC_0 \\ \alpha_i \cdot ADC_{LG} + \delta_i, & ADC_{LG} < ADC_0 < ADC_{HG} \\ \alpha_i \cdot \frac{ADC_{LG}}{1 + \beta(ADC_{LG} - ADC_0)} + \delta_i, & ADC_{LG} \geq ADC_0 \end{cases} \quad (4.3)$$

In practice most events occur in the first region, including all events of light nuclei up to oxygen. The last region is only reached for high energy iron nuclei and is also the only region that needs correction for non-linearity. The unified scale ranges to an equivalent HG ADC value of 13000, which is effectively a 13.6 bit scale.

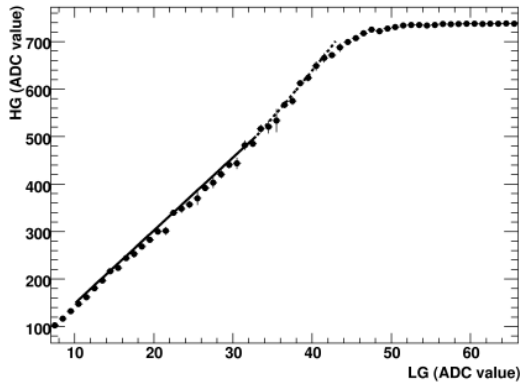


Figure 4.6: High-gain vs. low-gain signal and fit for α , δ , and β . Linear regime: solid line, Non-linear regime: dotted line.

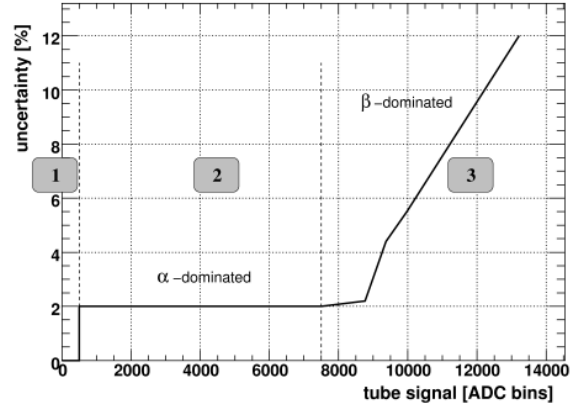


Figure 4.7: Scale uncertainty for the signal S_t in one single proportional tube. Almost all events fall into region 1 or 2, the increase in region 3 is due to the non-linear behavior of the ADC converter.

The parameters α_i , δ_i , and β are determined from data in every tube. Figure 4.6 shows data and fit for tube 37 of layer 2. The solid line represents the fit in the linear region and is continued with a dashed line for the fit modified to accommodate the non-linearity. The data are fitted up to $ADC_{LG} = 42$, above which the HG channel saturates.

The error bars drawn in Fig. 4.6 are statistical only, but the fit considers an additional uncertainty from temperature fluctuations. During the flight the temperature inside the instrument fluctuates following a night and day cycle (see Fig. 2.2). This causes, through the temperature dependent resistive signal splitting, the ratio between HG and LG to vary slightly.

The fits have an average reduced χ^2 of 0.6 and result in $\beta = (2.7 \pm 0.9) \cdot 10^{-4}$. The parameters α_i and δ_i are determined and used for each tube individually. Their distributions are Gaussian with mean values of 15.3 and -14 , and with widths of 0.5 and 11, respectively.

The uncertainties in these parameters introduces an additional uncertainty in the tube signal S_t in regions 2 and 3. It can be estimated in region 2 by

$$\Delta S_t^2 = ADC_{LG}^2 \cdot \Delta \alpha_i^2 + \Delta \delta_i^2. \quad (4.4)$$

The small contribution of $\Delta \delta_i$ can be neglected and the uncertainty in region 2 works out to be about 2%.

For the region 3 the uncertainty in β has to be propagated as well. The scale uncertainty is dominated by the contribution of β and is about 5.5% for $S_t = 10^4$. The scale uncertainty in all regions is plotted in Fig. 4.7.

4.3 Tube Alignment

The proportional tubes are not rigid and can therefore shift or bend a little within the frame of the instrument. For a correct trajectory reconstruction the exact positions of all tubes are

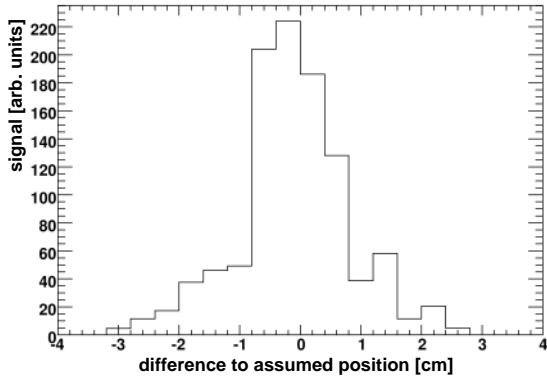


Figure 4.8: Summed signal in section 4 of tube 20 in layer 4 as a function of distance to the nominal tube position. The peak position marks the tube center.

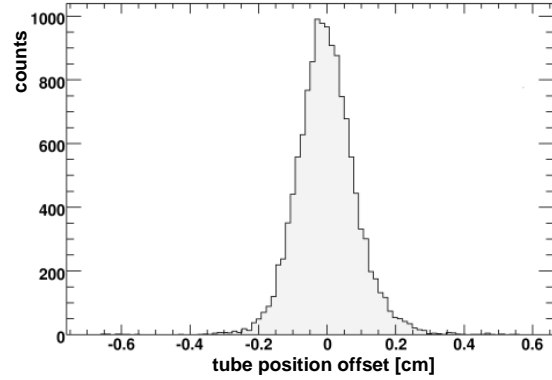


Figure 4.9: Offset distribution of the tube positions from the corrected positions. The positions are precise to 0.08 cm.

determined from the data themselves.

The actual tube positions are checked in nine sections along the tubes by determining the peak of the signal distribution as a function of position. An example is shown in Fig. 4.8 for a tube with minor offset. The peak in the signal corresponds to the tube center, through which the longest track lengths pass and produce the largest amount of ionization in the tube.

Figure 4.9 shows the offset distribution of all tube sections after the correction took effect. The tube positions assumed in the analysis are now matched within a 1σ offset of 0.08 cm to the actual positions during flight, compared to an average offset of 0.4 cm before correction.

4.4 Lateral Response Maps

To ensure a uniform response everywhere in the scintillation and Čerenkov detectors, lateral response maps are used to correct for non-uniformities in the signal. For each PMT a response map is calculated in $2 \times 2 \text{ cm}^2$ bins covering the whole detector area. The maps are derived from pre-flight muons recorded on the ground (muon maps). Then the maps are compared to their counterparts derived from carbon and oxygen data recorded during flight, to ensure their validity.

The validity of the response maps also requires the average signal to be independent of azimuth angle ϕ . No dependence on azimuth angle is expected, since the PMTs are arranged symmetrically around the quadrant centers, and the light is emitted isotropically in the scintillation detectors. The Čerenkov light cone is mostly isotropic due to the many reflections in the detector materials and a scintillating admixture. Still, the independence from azimuthal angle is verified with data taken during flight. The average signal as a function of azimuth angle during flight is shown in Fig. 4.10 for quadrant 3 of the top scintillator. All detectors used, scintillation and Čerenkov detectors, show no sign of azimuthal dependent signals beyond a 2% effect visible in Fig. 4.10 for the quadrant shown. The slight reduction is most probably

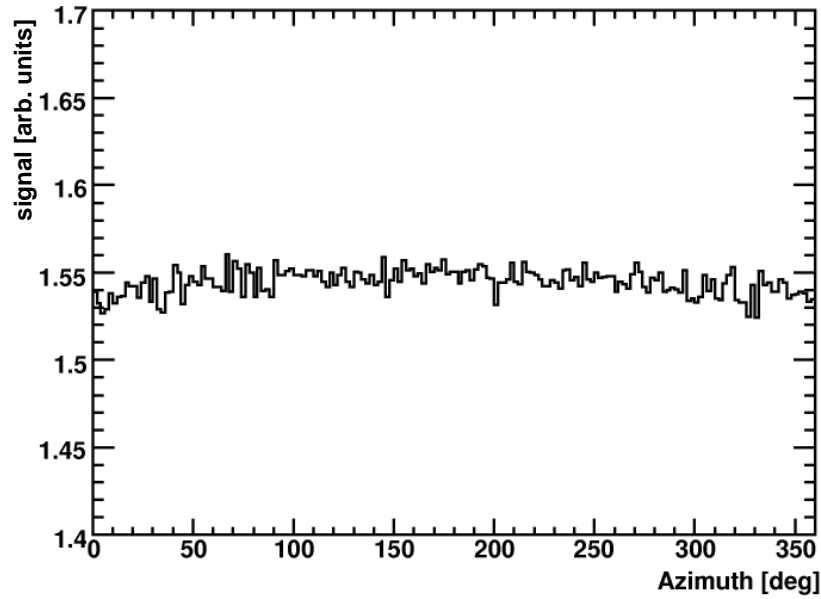


Figure 4.10: Average oxygen signal in quadrant 3 of the top scintillator as a function of azimuth. It is independent of azimuthal angle. This particular quadrant suffers a 2% reduction of the average signal, where few events might cause a statistical effect.

due to a statistical effect because of the low number of events in the direction of $\phi = 0^\circ$ and is of no significance for the data analysis.

4.4.1 Maps from Muon Data

Response maps from muon data are used in the final analysis, because they have the lowest statistical uncertainty. Because the muon signals are relatively small, the high voltage to the PMTs was increased to increase the PMT gain. Since the response maps represent a relative signal correction, they should not be affected by a change in PMT gain. This is verified with data of heavy nuclei.

In each bin i (2×2 cm²; 10,000 bins) the correction factor or response map value r_{ij} is derived for each PMT j as the uncorrected average signal

$$r_{ij} = \frac{\sum_i S_j}{N_i}, \quad (4.5)$$

with the signal S_j of PMT j and the total number of events N_i falling into bin i . N_i is on the order of 5000 events. The summation is carried out over all events occurring in bin i .

The small Čerenkov signal still leads to significant bin-by-bin fluctuations. These introduce an unnecessary source of uncertainty, since the response must be a steady and flat function. Except for the steeper edges, the Čerenkov response maps are therefore smoothed with a Gaussian kernel.

The smoothing kernel correlates an area of 5×5 bins and calculates a weighted average for

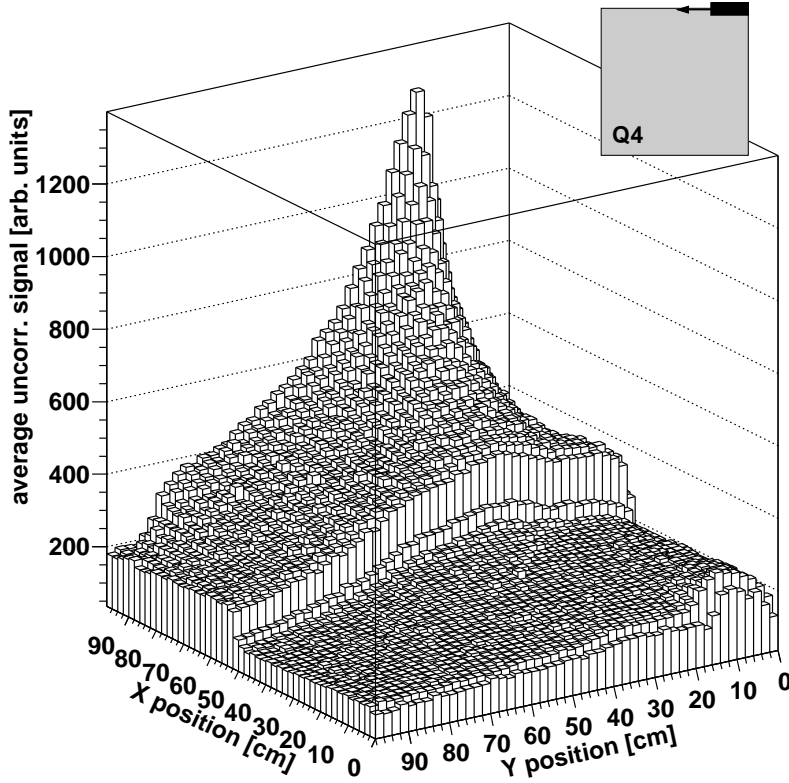


Figure 4.11: Lateral response map for PMT 10 in the top scintillator calculated from muon data. The steep drop at $X = 50$ cm is due to the meeting edges of the two scintillator sheets that build the quadrant. The position of the PMT in the quadrant and the direction of its view are illustrated in the gray box in the upper right corner of the figure.

the center bin. The Gaussian profile used is [25]:

$$\frac{1}{52} \cdot \begin{pmatrix} 1 & 1 & 2 & 1 & 1 \\ 1 & 2 & 4 & 2 & 1 \\ 2 & 4 & 8 & 4 & 2 \\ 1 & 2 & 4 & 2 & 1 \\ 1 & 1 & 2 & 1 & 1 \end{pmatrix}. \quad (4.6)$$

The response map for PMT 10 in the top scintillator (Figure 4.11) spans one quadrant, which is seen by the PMT from one corner. The signal peak visible is in front of the PMT, the signal then fades. In the middle of the quadrant is a steep step in response due to a discontinuity in scintillator material that is arranged in two sheets to span the quadrant.

Figure 4.12 shows the response map for PMT 19 in the bottom Čerenkov detector, which sees two quadrants. The signal response is flat, except right in front of the PMT, where events hit the wavelength-shifter bar and produce scintillation light. This produces the steep spine in the muon map. The response map shown in Fig. 4.12 is not smoothed.

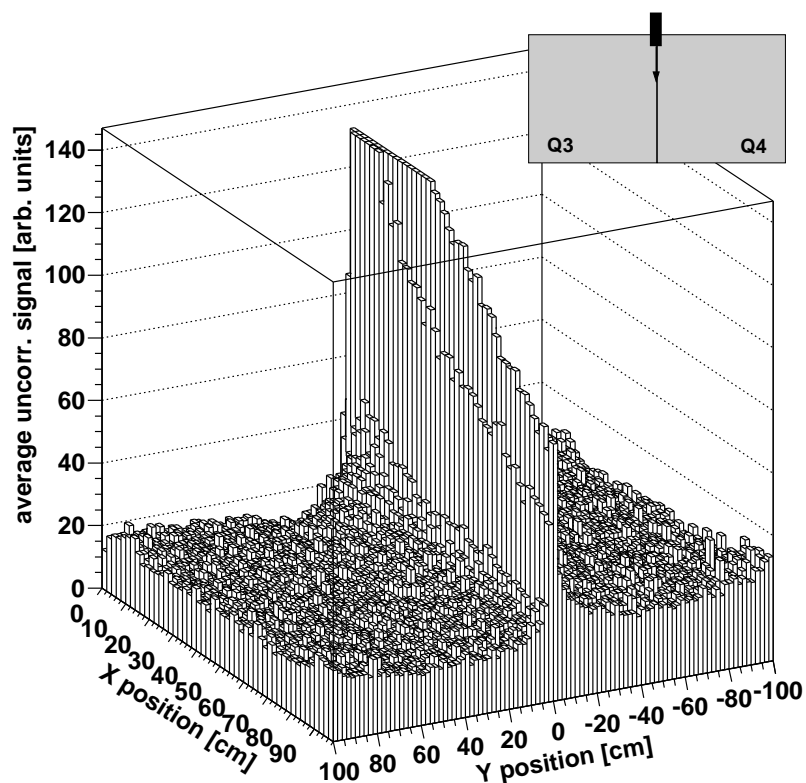


Figure 4.12: Lateral response map for PMT 19 in the bottom Čerenkov detector calculated from muon data before smoothing. Events hitting the wavelength-shifter bar between the observed quadrants produce scintillation light, hence the steep spine. The position of the PMT between the quadrants and the direction of its view are illustrated in the gray box in the upper right corner of the figure.

In the analysis the actual correction factor applied to each PMT's signal is interpolated at the exact position of the event calculated by the 2nd level trackfit. The lateral response map is fit by a plane in x - and y -direction using a 5×5 bins area around the event position. The correction factor is then the z -coordinate of the point in the plane where the track intersects.

If the gradient of the plane is very high (i. e. the response map very steep, $|\nabla z| > 5.5$), the respective PMT is excluded from the analysis. This ensures that the uncertainty in the track position does not impose a large uncertainty on the signal. In practice those steep gradients are only found around the edges of the wavelength-shifter bars and where scintillator sheets meet.

4.4.2 Comparison to Maps from Cosmic-Ray Data

No change in response maps is expected due to a change in PMT gain (e. g. due to voltage changes or gain drifts). Also, it is not expected that the alignment of the PMTs in flight changed from their configuration on ground. Nevertheless, these expectations are examined with data from cosmic-ray nuclei recorded in flight.

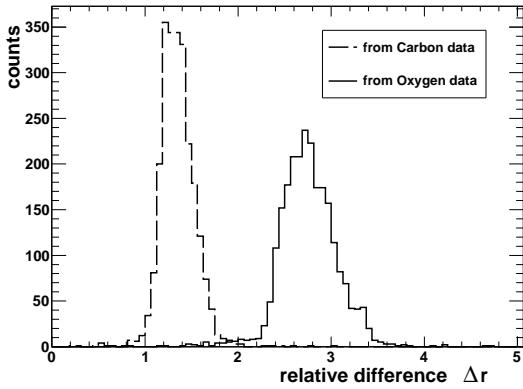


Figure 4.13: Comparison of muon map to data map for PMT 10 in the top scintillator. Data maps are calculated from carbon (dashed) and oxygen (solid) data, see text for the definition of Δr .

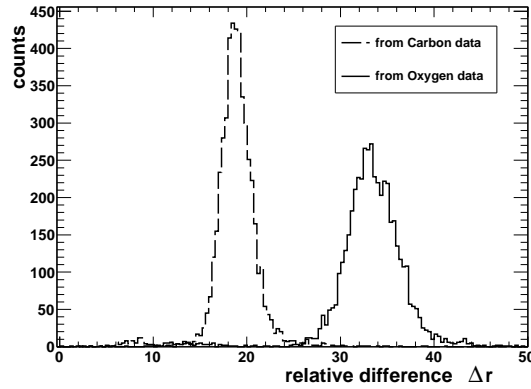


Figure 4.14: Comparison of muon map to data map for for PMT 19 in the top Čerenkov detector. Data maps are calculated from carbon (dashed) and oxygen (solid) data, see text for the definition of Δr .

Lateral response maps were built from actual flight data after carbon and oxygen samples were identified in a preliminary charge estimation. These data response maps were then compared to the muon maps.

The relative difference of data maps to muon maps is shown in Fig. 4.13 and 4.14 respectively for the same PMTs as the muon maps were shown before in Figures 4.11 and 4.12. The quantity evaluated is:

$$\Delta r = \frac{r_d - r_m}{r_m}, \quad (4.7)$$

where r_d is the value of the data map and r_m the value of the muon map. Δr is evaluated for all bins in the quadrant(s) the PMT observes.

The Gaussian shape of the peaks — the reduced χ^2 of fits to Gaussian distributions is smaller than 1.4 — shows that the response maps have the same overall form. There are no changes in alignment of the PMTs during launch or flight. The widths of the distributions are dominated by the statistical fluctuations of the carbon and oxygen maps. The Čerenkov detector suffers more from poor statistics because of the smaller signal. The width changes as expected when only parts of the data from the flight is used (e. g. selection A). It was also shown that the distributions are commensurate for the first and second half of the flight.

The relative difference in peak positions between carbon and oxygen reflects the change in signal with the charge of the incident particle. For the scintillator signals this difference is expected to be 1.6 and is measured to be 1.6. Also for the Čerenkov signals an excellent agreement is observed between the expected separation of 1.8 and the measured value of 1.7. This shows that the overall signal height is of no importance to the response maps. They are independent of PMT gain changes.

The comparison of lateral response maps from pre-flight muons and in-flight oxygen and carbon shows that the muon maps are valid for the entire flight.

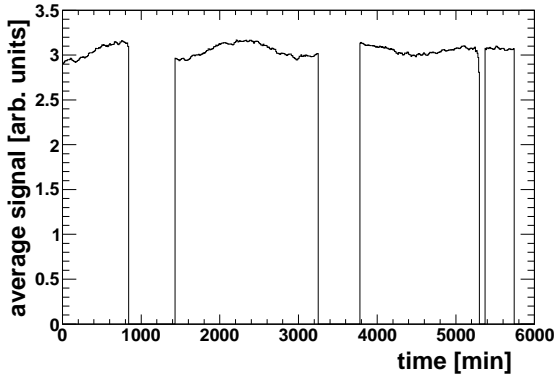


Figure 4.15: Average oxygen signal as function of time for PMT 8 in the top scintillator to illustrate gain variations during flight. Gaps occur due to interruptions in the data taking.

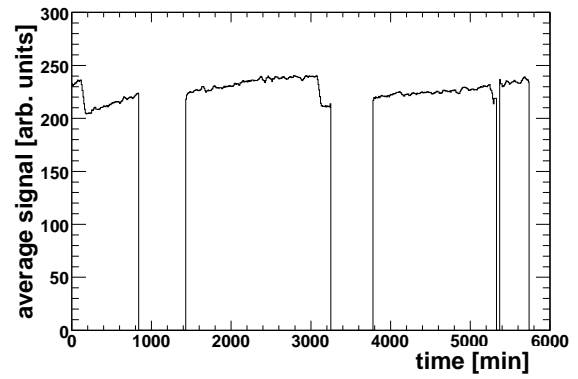


Figure 4.16: Average oxygen signal as function of time in the proportional tubes of manifold 6 to illustrate gain variations during flight. Gaps occur due to interruptions in the data taking.

4.5 Time Dependent Gain Normalization

The gain in the proportional tubes and PMTs is not entirely stable during 4.5 days of flight. Temperature, voltage, and variations in gas pressure cause slight gain drifts with time. The signal of each PMT is corrected individually, thereby setting the signal normalization for all Čerenkov PMTs and scintillator PMTs. The gain in the proportional tube system is corrected for each of the manifolds, which provide gas and voltage to the individual tubes.

The gain is normalized with oxygen data after a preliminary charge estimation. The average signal is computed in 10 minute bins for the whole duration of the flight. Figure 4.15 and Figure 4.16 show the average signal for a PMT and a manifold respectively. These average signals are used as correction factors to normalize all responses by time bin. The gain during flight is stable within about 10% of the mean gain in the PMTs and proportional tubes.

4.6 The Reconstructed Signal

4.6.1 Scintillation and Čerenkov Signal

The signals from the PMTs in the scintillation and Čerenkov detectors are read out and digitized to 4096 ADC bins. For the analysis the signals of all PMTs are used, provided the PMTs are active at the time of the event, are in the quadrant the particle intersects the detector, and are not saturated.

Each PMT's signal s_i is corrected to vertical track length in the detector material by a zenith angle correction $\cos \Theta$. It is corrected for gain drifts by a time dependent normalization $c_i(t)$, and for lateral response non-uniformities $r_i(x, y)$. Gain normalizations and lateral response corrections are described in Sections 4.5 and 4.4, respectively.

After these operations the signals of all PMTs i are combined to an average signal S

$$S = \frac{1}{n} \cdot \sum_i \frac{s_i}{c_i(t)r_i(x,y) \cos \Theta}. \quad (4.8)$$

This is the signal used in the following analysis to determine charge and energy of cosmic-ray events. It is required for the later analysis that the signal was reconstructed from at least 3 PMTs. Typically, events are seen by 6 to 7 PMTs of a quadrant.

4.6.2 dE/dX-array and TRD Signal

For the signal reconstruction of the proportional tubes, all active tubes are used through which the trajectory of the event passes.

The signal of each tube is corrected for spatial gain variations (Section 2.4), time dependent gain variations (Section 4.5), and is converted to the unified scale described in Section 4.2.

After these operations the tube signals s_i are combined to an average taking into account the length of the trajectory through each tube. The signal in the dE/dX-array is the average in the top 8 layers, the TRD signal of the bottom 8 layers of the proportional tube system. If both signals are equal within fluctuations, no transition radiation was produced in the TRD and all 16 layers (dE/dX-array and TRD) measure the specific ionization in gas, dE/dX . The average signal S is defined as

$$S = \frac{\sum_{i=k}^n s_i}{\sum_{i=k}^n \Delta x_i} \text{ for } \Delta x_i > 1 \text{ cm}, \quad (4.9)$$

where the summation is over the tube layers. For the dE/dX-array $k = 1$ and $n = 8$, for the TRD $k = 9$ and $n = 16$. For events without transition radiation the average signal can be calculated for the whole proportional tube array with $k = 1$ and $n = 16$, thereby reducing the signal fluctuations by $\sqrt{2}$.

Tube signals are excluded, if the associated track length Δx_i is less than 1 cm. This is necessary to reduce statistical signal fluctuations dominated by small signals, and because particles skimming the tube wall may produce enhanced signals due to δ -ray production in the mylar tube body [73].

On average 14 of 16 possible tubes are hit in an event. Signal fluctuations and the resulting energy resolution are mentioned in Section 2.3.3.

CHAPTER 5

CHARGE MEASUREMENT

5.1 The Scintillator-Čerenkov Correlation

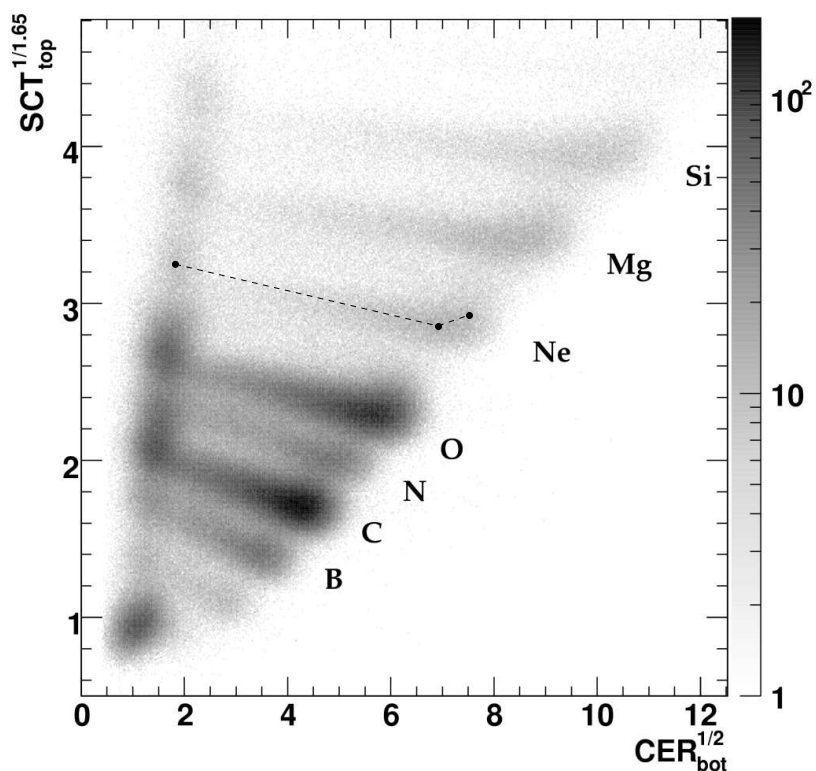


Figure 5.1: Top scintillator vs. bottom Čerenkov signal for elements from B to Si. Both signals are scaled to be linear in charge. Elements are grouped along lines of constant charge. The dashed line and points illustrate the charge line parametrization for neon.

The charge measurement relies on the correlation of the signals from the scintillation and Čerenkov detectors. As an example, the correlation of top scintillation and bottom Čerenkov detectors for elements up to silicon ($Z = 14$) is shown in Figure 5.1. The elements are aligned on lines of constant charge. The lines visible in Fig. 5.1 can be distinguished because the

signals scale with $Z^{1.65}$ and Z^2 for the scintillation and Čerenkov counters, respectively. In order to establish linearity in charge, the scintillator and Čerenkov signals are scaled to the power 1/1.65 and 1/2, respectively.

For the analysis the combinations of scintillation and Čerenkov counters used are top/top, top/bottom, and bottom/bottom. Correspondingly, the charges are measured at the bottom of the instrument Z_{bot} (bottom/bottom), and at the top Z_{top} (top/top). For data selection C the charge at the top of the instrument is Z_{tb} , derived from the top/bottom combination.

At low energy, below Čerenkov threshold (0.33 GeV/amu), clusters of events are arranged along a line almost parallel to the ordinate, which corresponds to residual scintillation in the Čerenkov material. With increasing energy, the Čerenkov signal increases, while the scintillation signal decreases according to the Bethe-Bloch relation. The Čerenkov response saturates slightly above the signal level corresponding to the energy of a minimum ionizing particle. Events above that energy are clustered around the point that corresponds to the saturated Čerenkov signal and a constant scintillator signal, which is just slightly above the minimum ionization level.

5.1.1 Preliminary Charge Estimation

Some normalizations derived in Chapter 4 require samples of individual elements. These samples are selected directly from the scintillator-Čerenkov correlation, because the final charge measurement needs all corrections in place.

Carbon, oxygen, and iron samples are generated by cutting squares out of the correlation space around minimum ionizing energy. The location of this selection coincides with the middle marker along the lines of constant charge, an example of which is illustrated in Figure 5.1 for neon.

The quality of this cut and its efficiency are not of concern for calculating signal corrections.

5.1.2 Parametrization of the Lines of Constant Charge

To assign a charge value (not necessarily an integer charge) to every point of the signal correlation of Fig. 5.1, first the Čerenkov and scintillator signals are parametrized for three energies as functions of charge. These three fixed points in the signal correlation for each charge are then used to define lines of constant charge in the scaled representation, as Fig. 5.1 shows as a dashed line for neon.

The energies used for the parametrizations correspond to Čerenkov threshold, the energy at minimum ionizing, and the energy at saturation of the scintillation and Čerenkov responses. The three thick markers in Figure 5.1 illustrate the signal coordinates at those energies for neon.

The Čerenkov Signal as Function of Charge The Čerenkov signal S_C is always proportional to Z^2 (see Eq. 2.2), so only the β -dependent proportionality factor $C(\beta)$ is fit at each

energy:

$$S_C = \frac{C_0 \cdot Z^2}{1 - 1/n^2} \cdot \left(1 - \frac{1}{n^2\beta^2}\right) = C(\beta) \cdot Z^2, \quad (5.1)$$

with a different value for C at each of the three different energies. The proportionality factors are found for both, bottom and top Čerenkov detectors, in the three counter combinations used. In the top/bottom and bottom/bottom combinations, the same value was found for the bottom Čerenkov signal.

The Scintillation Signal as a Function of Charge The scintillation signal S_S is proportional to the light yield in the scintillating material. Due to a saturation effect the light yield dL/dX is not exactly proportional to the deposited energy dE/dX .

Scintillation light is produced when ionizing radiation excites the scintillating material. If the energy deposit is very large in a small volume, all molecules are excited and thus the light output saturates at the core of the ionized volume. Especially for heavy ions, this means that, although the energy deposit dE/dx is proportional to Z^2 , the light yield dL/dx is not. The exponent is energy and charge dependent. There are many models to describe this effect, e. g. by Voltz [87] and Birks [17]. Here we follow an empirical description of Matsufuji [56] describing the light yield as

$$S_S \propto \frac{dL}{dx} = \alpha_0(E, Z) \left(\frac{dE}{dx}\right)^{\beta(E, Z)} = \alpha(E, Z) \cdot Z^{2 \cdot \beta(E, Z)}, \quad (5.2)$$

with the parameters α and β that themselves are functions of charge and energy.

The parameters α and β are estimated as functions of Z at the three energies used for the parametrization by fits to the data. This way the scintillation signal can be expressed as a function of charge Z at these three energies needed. For the scintillators used here, β is about 0.8, so that the light yield is on average proportional to $Z^{1.65}$. The exponent of the charge is smaller than that for heavy elements and closer to 2 for light elements because of the different extent of the saturation effect.

Charge Line Parametrization With the scintillation and Čerenkov signal parametrized as functions of charge at three energies, three points are defined for each element on its line of constant charge. These three points are illustrated in Fig. 5.1 for neon.

They define two linear functions along the lines of constant charge in the scaled signal space shown. This is the parametrization of the scintillator signal S_S as a function of Čerenkov signal S_C and charge Z :

$$S_S = f(S_C, Z). \quad (5.3)$$

This parametrization is calculated individually for all detector combinations used, and is a steady function of Z in the whole signal space. It is used in the next section to assign each event a measured charge.

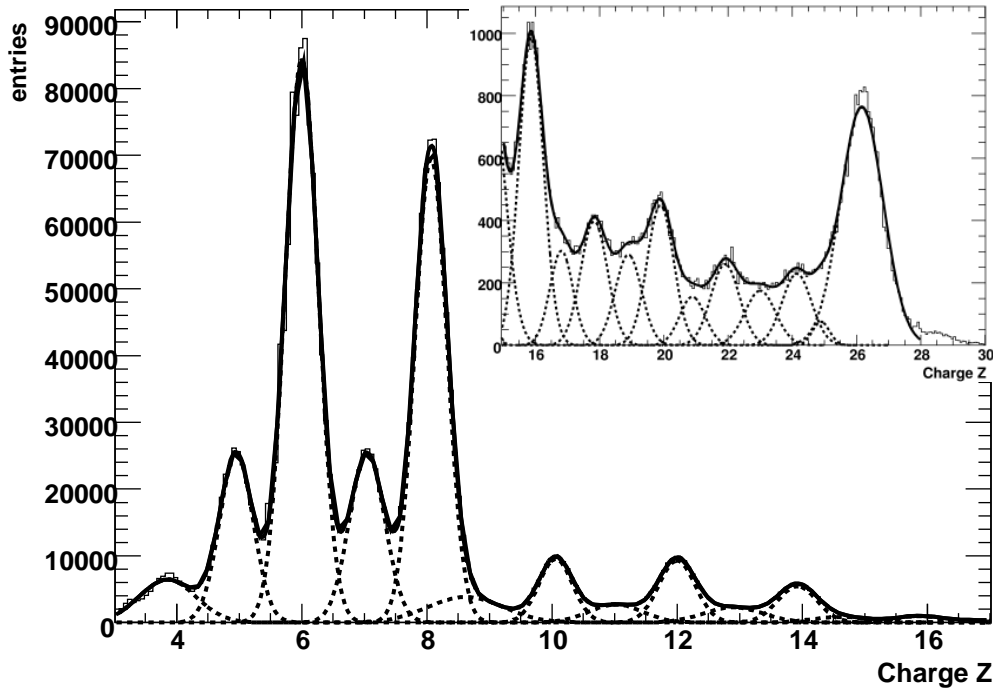


Figure 5.2: Charge histogram from boron to iron for the average charge \hat{Z}_t . A global fit is shown as a solid line, with the results for individual elements as dashed lines. See text for details.

5.2 Charge Assignment and Resolution

For each event, a charge Z is obtained from the measured scintillation and Čerenkov signals. In general, this charge is not an integer number.

Three charges are determined: two at the top of the instrument Z_{top} and Z_{tb} , and one at the bottom of the instrument Z_{bot} . For data selection C, for which the top Čerenkov detector cannot be used, Z_{tb} is used in the analysis instead of Z_{top} .

Individual charge resolutions are found for all elements for all three reconstructed charges with a Gaussian fit to peaks of the charge histogram. For this, elements are selected by the respective other charge: For determining the bottom charge resolution an element is selected by a hard cut on the top charge and vice versa. Resulting charge resolutions are given in Table 5.1.

The bottom charge, Z_{bot} , is less precise than the top charges, Z_{top} and Z_{tb} , because more δ -rays contribute to the total signal in the bottom scintillator. Of the top charges Z_{top} is more precise, but the shortcoming of Z_{tb} is small compared to the one of Z_{bot} . This results in a slightly worse charge resolution for data selection C.

The best charge resolution is obtained by combining top and bottom charges to average charges \hat{Z}_t and \hat{Z}_{tb} :

$$\hat{Z}_t = \frac{Z_{top} + Z_{bot}}{2}, \text{ or } \hat{Z}_{tb} = \frac{Z_{tb} + Z_{bot}}{2}. \quad (5.4)$$

For \hat{Z}_{tb} for data selection C, the top charge Z_{top} is replaced by Z_{tb} . The charge resolutions of

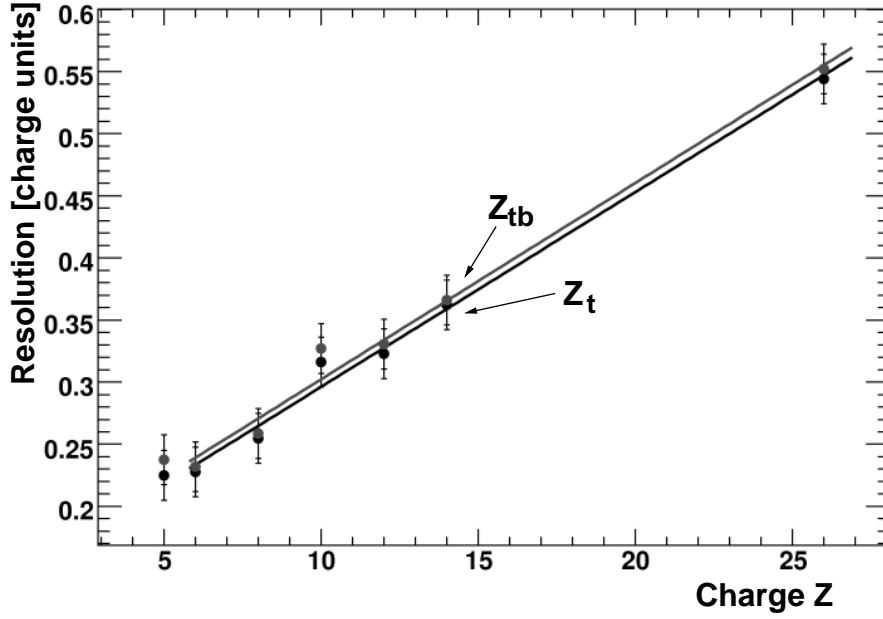


Figure 5.3: Charge resolution of the average charges \hat{Z}_t and \hat{Z}_{tb} . Without the use of the top Čerenkov counter the charge resolution is slightly reduced for \hat{Z}_{tb} . The depicted uncertainties are propagated from a Gaussian fit that determines the resolutions of the individual charges Z_{top} , Z_{tb} , and Z_{bot} .

the average charge is then $\hat{\sigma}_t = 0.5 \cdot \sqrt{\sigma_{top}^2 + \sigma_{bot}^2}$. Although this uncertainty is in principle enlarged by a small correlation factor when using \hat{Z}_{tb} , such an effect could not be found within the precision of the determination of the charge resolutions.

Figure 5.2 shows a charge histogram for all elements from beryllium to iron ($Z = 4$ to 26) for the average charge \hat{Z}_t derived from Z_{top} and Z_{bot} . A global fit to the histogram is illustrated as a solid line, with the results for individual elements in dashed lines. The fit assumes Gaussian peaks for all elements, so that the fit function $F(Z)$ is

$$F(Z) = \sum_i A_i e^{-\frac{(Z-Z_i)^2}{\sigma_i^2}}, \quad (5.5)$$

with the normalization A_i , the peak position Z_i , and the individual charge resolutions σ_i for all elements i from Be to Fe.

The resolutions found in the fit are in excellent agreement with the ones found by propagating the resolutions of the individual charge measurements to the average charges. The charge resolutions for the average charges \hat{Z}_t and \hat{Z}_{tb} are given in Table 5.1 for iron, oxygen and carbon. They are also shown in Figure 5.3. It can be seen that the measured resolutions are charge dependent and can be modeled as a linear function of the charge. This is the case, because the scintillation signal is not proportional to the square of the charge. The absolute charge resolutions for boron and carbon for the average charges \hat{Z}_t and \hat{Z}_{tb} are about 0.23 charge units e . They are equal within their uncertainties, presumably because the saturation effect in the scintillation counters for the two light elements is very similar leading to the

Table 5.1: Measured charge resolutions for carbon, oxygen and iron in charge units e . Given are resolutions of individual charges σ_{top} , σ_{tb} , and σ_{bot} as well as the resolutions of the average charges $\hat{\sigma}_t$ and $\hat{\sigma}_{tb}$.

| element | σ_{top} | σ_{tb} | σ_{bot} | $\hat{\sigma}_t$ | $\hat{\sigma}_{tb}$ |
|---------------|----------------|---------------|----------------|------------------|---------------------|
| carbon | 0.29 | 0.31 | 0.36 | 0.23 | 0.23 |
| oxygen | 0.31 | 0.33 | 0.42 | 0.25 | 0.26 |
| iron | 0.61 | 0.64 | 0.9 | 0.55 | 0.55 |

same resolution.

The difference in resolution of the average charge between data selections A and B, to data selection C, where Z_{tb} has to be used, is small (see Fig. 5.3). This means that the charge cut efficiencies over the whole flight are very similar.

The charge resolutions of the three individual charge measurements are in agreement with the charge resolution found in the analysis of the data from earlier flights of TRACER.

5.3 Charge-Changing Interactions

Neglecting signal fluctuations and interactions between the top and the bottom of the instrument, an event will be located exactly on its line of constant charge in correlations of any counters, top or bottom. However, energy loss and charge-changing interactions cause events to deviate from this expectation.

Events lose energy on the way to the bottom of the instrument. For a high-energy event this loss is not significant and it will stay on its charge line. For a low-energy event, however, this loss can be large and it produces then a larger signal in the bottom scintillator, and thus appears as a heavier nucleus at the bottom.

More important is the necessity to exclude events that underwent charge-changing interactions in which a nucleus of charge Z splits up into two products with charges Z_1 and Z_2 ($Z_1 + Z_2 = Z$). The products of the interaction will produce a smaller scintillation signal S_S and thus appear as a lighter particle in the bottom, because the signal is proportional to a power of the charge, and the power of a sum is larger than a sum of powers:

$$(Z_1 + Z_2)^n > Z_1^n + Z_2^n, \quad (5.6)$$

with Z_1 , Z_2 , and n greater than 1. Requiring consistency in the charge measurements on top and bottom permits to exclude interacting particles.

Figure 5.4 shows the charge distribution of Z_{bot} of events determined as iron at the top of the instrument. The figure illustrates both effects, when the measured distribution is compared to the Gaussian fit to the upper flank (solid line). Above the fitted curve very low-energy particles appear as heavier nuclei. Below, the long tail visible is due to interacting particles that appear as lighter nuclei in Z_{bot} . These interacting nuclei have to be avoided in the analysis.

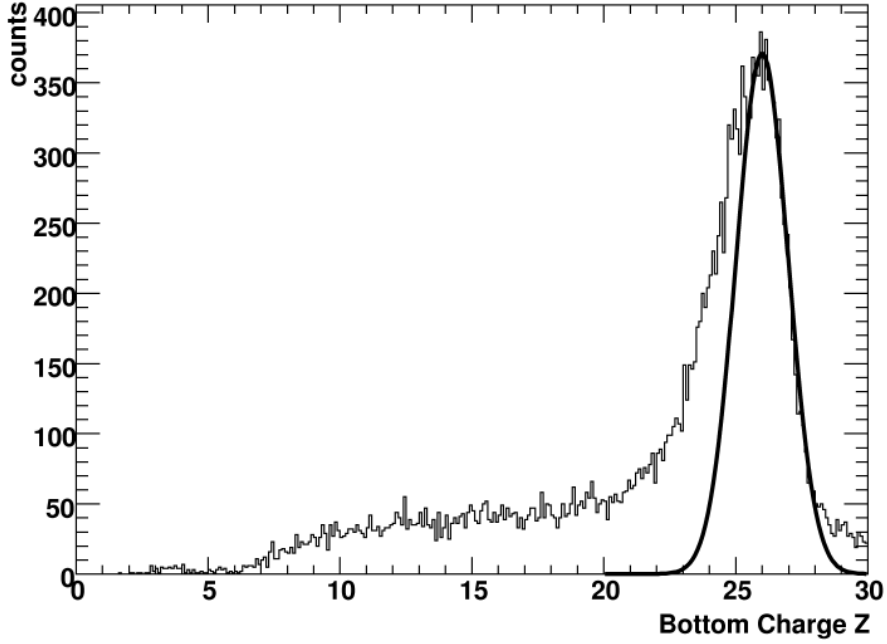


Figure 5.4: Illustration of interacting iron nuclei. Bottom Charge Z_{bot} distribution of events identified as iron at the top, $Z_{top} = 26 \pm 0.1$. About 50% of iron nuclei undergo a charge-changing interaction within the instrument. The solid line represents a Gaussian fit to the upper flank of the distribution to illustrate non-interacting nuclei.

An estimate of how many nuclei interact within the instrument can be derived from the data themselves or can be calculated if the total cross sections are known. From Figure 5.4 it can be estimated that about 50% of iron nuclei undergo a charge-changing interaction within the detector (from top Čerenkov to bottom scintillator), which is in agreement with the survival probability derived in the next section.

Calculation of Interaction Losses

The losses due to charge-changing interactions in the instrument and the residual atmosphere above the instrument must be taken into account and thus calculated. Therefore, total spallation pathlengths are estimated from total charge-changing cross sections derived with the Bradt-Peters form (see for example [93]):

$$\sigma = \pi r_0^2 \left(A_I^{1/3} + A_T^{1/3} - b \right)^2, \quad (5.7)$$

with the mass number of the incident particle A_I , the mass number of the target A_T , and the parameters $r_0 = 1.35$ fm and $b = 0.83$. The interaction lengths λ_i for all materials (with mass m_i) encountered by the particle on its way through the atmosphere and detector have to be evaluated individually for each cosmic-ray element j : $\lambda_{ij} = m_i / \sigma_{ij}$.

The survival probability P_j of a nucleus j can then be expressed as the product of the

survival probabilities through each material layer i :

$$P_j = \prod_i \exp \left[-\frac{\rho_i}{\lambda_{ij}} \right], \quad (5.8)$$

with the column density of layer i , ρ_i .

A detailed material list of the instrument determines the total column density of the active detector parts to 7.7 g/cm^2 ; the average residual atmosphere above TRACER was 4.5 g/cm^2 . The survival probability through instrument and atmosphere for iron or boron nuclei are 31% and 58% respectively.

One big advantage of a space mission is to avoid interactions in the atmosphere. Still, the survival probability in the detector itself is 48% and 73% for iron and boron respectively, in agreement with the observation in the iron data (see Fig. 5.4). These survival probabilities are calculated for the average incident angle of $\Theta = 30^\circ$.

In the data analysis this survival fraction is taken into account as a modified aperture for the instrument for each element. For example the geometric aperture of $3.85 \text{ m}^2 \text{ sr}$ found in Section 2.2.2 is reduced to an effective aperture of $1.2 \text{ m}^2 \text{ sr}$ for iron or $2.22 \text{ m}^2 \text{ sr}$ for boron.

5.4 The Selection of Elements

For the selection of elemental data samples, a charge cut is needed that produces clean samples with high efficiency. The most natural way to exploit the two independent charge measurements of TRACER is to realize a charge cut in the two-dimensional parameter space of Z_{top} and Z_{bot} . The two-dimensional charge histogram for light elements boron to oxygen is shown in Figure 5.5. It shows the clearly separated Gaussian peaks of the light elements.

A reasonable charge selection cut would be the 1σ contour around the charge peaks. However, in order to maximize the selection efficiencies ϵ and minimize contamination by adjacent elements at the same time, a different optimal shape of the cut was determined. To still follow the shape of the peaks in Fig. 5.5, the chosen selection cut is an ellipse with half axes commensurate with the charge resolutions in Z_{top} and Z_{bot} . The center of the cut ellipse $[C_{top} / C_{bot}]$ is at the fitted peak position. The shape of the selection cut is illustrated in Fig. 5.6, next to a parametrization of the elemental distributions of B, C, N, and O.

The half axis in the top-charge direction R_{top} must be small enough to avoid contamination by adjacent elements. It is noteworthy that contamination from lower charges is no issue for the energy measurement, but that contamination from heavier nuclei is important to avoid. This is the reason why in the case of boron the center of the selection cut is offset slightly towards lower charge and R_{top} is chosen to be rather small, although this results in a lower efficiency for boron.

The half axis in bottom-charge direction, R_{bot} , is chosen to avoid interacting events that appear at lower charge in the bottom. The restriction towards higher Z_{bot} does not have to be as strict, so the upper half axis of the selection cut used is $2 \cdot R_{bot}$. This allows for higher reconstructed charges to be accepted, which are due to the δ -ray effect in the bottom scintillator. It was found that the selection cuts defined like outlined before introduce some energy bias.

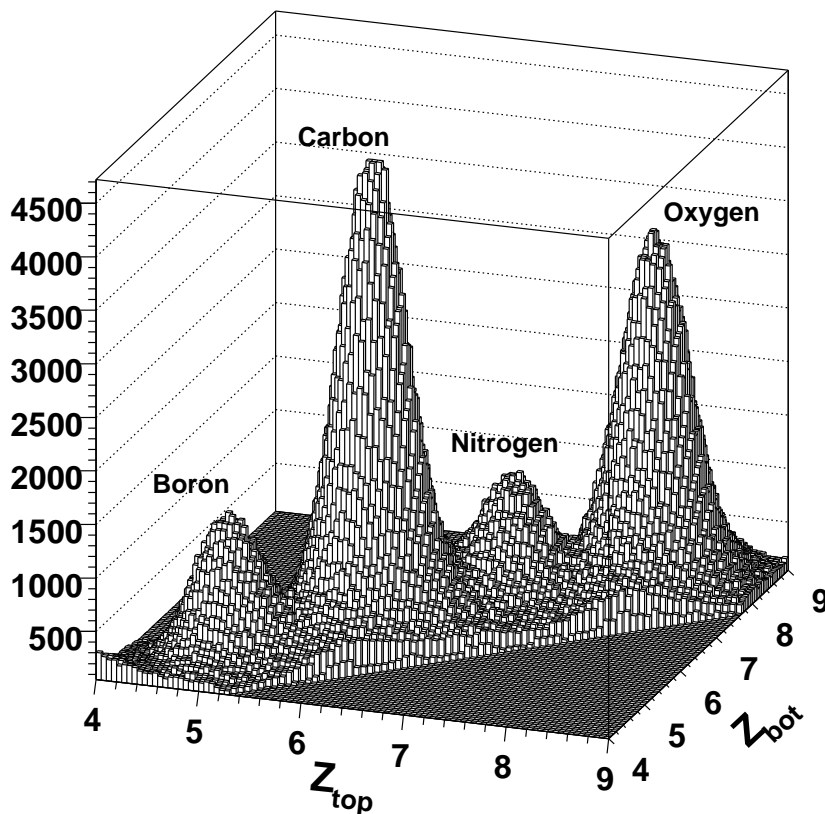


Figure 5.5: Two-dimensional charge distribution for B, C, N, and O data. The Gaussian peaks are clearly separated.

Therefore, cut efficiencies ϵ are determined for data samples below and above 3 GeV/amu. The low-energy efficiency ϵ^{LE} is higher than the efficiency at high energies ϵ^{HE} , because the δ -ray effect in the scintillation detectors causes lines of constant charge to be grouped more closely at high energies. This effect is more pronounced for heavy elements as can be seen in Table 5.2.

The efficiencies were estimated using the parametrization of the charge peaks by 2D-Gaussian distributions. The Gaussian distributions (shown in Fig. 5.6) were fitted to the data close to the peak position to avoid biases due to interactions and contamination. The efficiencies are derived as the integral within the cut areas divided by the total integral of the found Gaussian functions.

The cut parameters and cut efficiencies are summarized in Table 5.2. The same selection cuts are used for all data. The efficiencies have been determined for data selections A, B, and C (see Section 2.5) individually, as well as above and below 3 GeV/amu. The total efficiency is then the weighted average of the efficiencies for each selection.

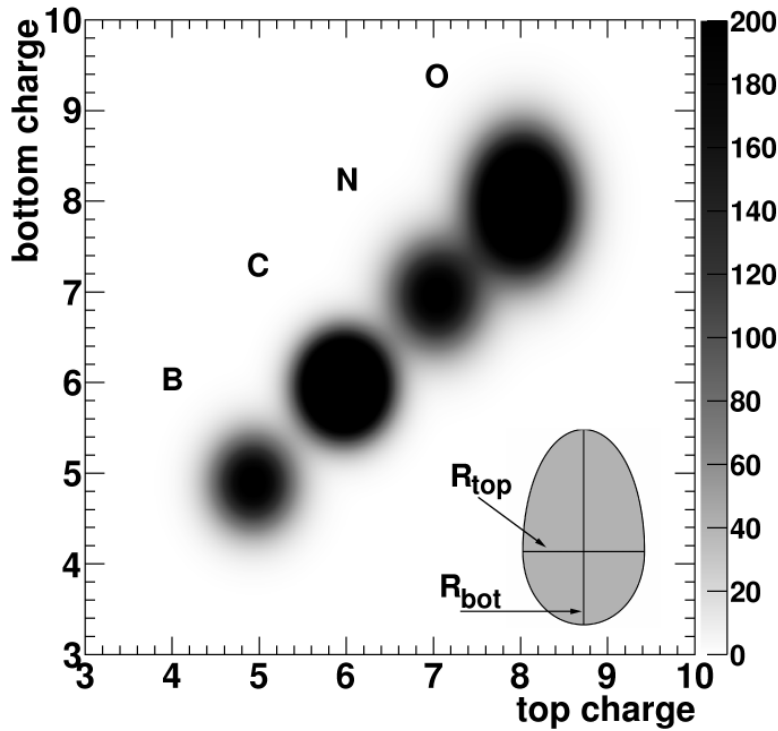


Figure 5.6: Parametrization of the charge distribution of top and bottom charge for B, C, N, and O. The shape of the selection cut used is illustrated.

Table 5.2: Parameters of charge selection cuts for boron, carbon, oxygen, and iron. Given are the cut positions in top and bottom charge $[C_{top} / C_{bot}]$ and the radii of the cut ellipses R_{top} and R_{bot} . Also efficiencies ϵ are given in the low- (LE, < 3 GeV/amu) and high-energy (HE, > 3 GeV/amu) region for selections A, B, C, and the complete data set.

| element | $[C_{top} / C_{bot}]$ | R_{top} | R_{bot} | $[\epsilon_A^{LE}, \epsilon_A^{HE}]$ | $[\epsilon_B^{LE}, \epsilon_B^{HE}]$ | $[\epsilon_C^{LE}, \epsilon_C^{HE}]$ | $[\epsilon^{LE}, \epsilon^{HE}]$ |
|---------------|-----------------------|-----------|-----------|--------------------------------------|--------------------------------------|--------------------------------------|----------------------------------|
| boron | [4.9 / 4.85] | 0.30 | 0.32 | [0.56, 0.42] | [0.46, 0.39] | [0.45, 0.30] | [0.48, 0.36] |
| carbon | [5.95 / 5.9] | 0.32 | 0.36 | [0.62, 0.49] | [0.55, 0.45] | [0.54, 0.40] | [0.56, 0.44] |
| oxygen | [8.0 / 8.0] | 0.52 | 0.60 | [0.86, 0.73] | [0.84, 0.70] | [0.76, 0.62] | [0.81, 0.68] |
| iron | [26 / 25.5] | 1.00 | 1.20 | [0.82, 0.63] | [0.79, 0.51] | [0.74, 0.43] | [0.78, 0.50] |

5.5 Carbon Contamination in the Boron Sample

For the low-abundance element boron it is especially important to avoid contamination from the highly abundant adjacent element carbon. Carbon of a low energy E would be incorrectly identified as a boron nucleus of a much higher energy E' in the energy measurement, and thus influence the measurement of the boron-to-carbon ration greatly.

The contamination is estimated by evaluating the two-dimensional parametrization of the carbon charge distribution inside the boron selection cut. Also, the number of carbon events

that fluctuate into the boron selection cut is estimated from data themselves. Therefore the cut silhouette for boron is moved around the carbon peak to an off region, where no boron is present. Assuming the carbon peak is symmetrical, the number of events at the off position in the selection cut is equal to the carbon contamination in the selected boron sample.

Both methods reveal a contamination of about 250 ± 12 carbon events in the sample of 40,000 boron events (0.6%) above 3 GeV/amu. This small contamination still has to be taken into account when the boron energy spectrum is constructed and the boron-to-carbon ratio is determined (Section 6.3.1).

Contamination from the lighter element beryllium can be neglected.

CHAPTER 6

ENERGY MEASUREMENT — THE ENERGY SPECTRA OF COSMIC RAYS

In this chapter the energy spectra of iron, oxygen, carbon, and boron are determined and discussed. Quality cuts applied to the data are explained as well as a high-energy selection cut, necessary to discriminate between high- and low-energy particles. After all equations are given to derive the energy spectra, all efficiencies and exposure factors are presented.

Special care is taken to reduce correlations between adjacent energy bins. In a steeply falling spectrum more events fluctuate into a bin from its low-energy neighbor, than out of it. This effect is accounted for with the so-called “overlap corrections”.

Additional effects introduce a bias to the measured energy spectrum of boron and must be corrected: Contamination from carbon and the atmospheric production of boron from heavier elements.

The necessary response functions in energy, signal fluctuations, and energy resolutions for all three sub-detectors used in this chapter have been described in Section 2.3.

6.1 The Determination of the Spectra

6.1.1 Quality Cuts and High-Energy Selection

The energy spectra are derived from high-quality events: The track of every event must be well defined through the whole proportional tube array. This assures a large lever arm for a good trajectory reconstruction. All proportional tube signals of the dE/dX-array and TRD used have to be consistent within 40%. This excludes very low-energy events and events with anomalies in tube response. Events have to be seen by at least 3 PMTs in every scintillation detector or Čerenkov counter.

These quality cuts have a combined efficiency of about 90%. An additional quality cut for low-energy events (below 3 GeV/amu) accepts only events of zenith angles between 30° and 32° in order to ensure total internal reflection of all Čerenkov light. This cut accepts only 4.3% of all low-energy events, but the overwhelming number of low-energy events still assures good

statistics.

The energy measurement is done with the bottom Čerenkov counter (at about 1 GeV/amu), the dE/dX-array (10 to 500 GeV/amu), and the TRD (above 700 GeV/amu). Accordingly, the spectra are determined with data points based on these three sub-detectors.

As can be seen from the response functions in Fig. 2.10, the response in the proportional tube array is ambiguous. Low-energy events and high-energy events produce large signals in the proportional tubes. This degeneracy is resolved by requiring a large Čerenkov signal.

Figure 6.1 shows the correlation of the dE/dX signal with the bottom Čerenkov signal for oxygen. The minimum of the correlation corresponds to minimum ionizing energy, 2.78 GeV/amu. In the normalization used here, minimum ionizing energy is at $3.07 \cdot Z^2$ in the dE/dX signal and $0.51 \cdot Z^2$ in the Čerenkov signal. Accepting only events with a Čerenkov signal greater than $0.51 \cdot Z^2$ for the high-energy spectrum (above 10 GeV/amu) avoids the degeneracy in the response functions of the dE/dX-array and the TRD. This cut is called “high-energy selection cut” and is shown in Fig. 6.1 as a solid line. The efficiency of this cut is discussed together with the effect of bin correlations in Section 6.1.4.

Another necessary cut is illustrated in the correlation of the signals from the top and bottom Čerenkov detectors, see Fig. 6.2 for oxygen nuclei. Residual scintillation has been subtracted, so the distribution begins at zero for both counters for events with energy below Čerenkov threshold. Then, the top Čerenkov signal increases while events are still below Čerenkov threshold in the bottom of the instrument due to energy loss. As the energy increases, the distribution crosses the diagonal. Above about 1.2 GeV/amu, particles are above the diagonal, because the bottom Čerenkov signal is enhanced due to δ rays (see Section 2.3).

In this plot a few events appear above the diagonal with high bottom Čerenkov but small top Čerenkov signal (thick markers in Fig. 6.2). These events show large signals in the proportional tube system, are about as abundant as TR events, but are low in energy. They presumably lose all their energy in the instrument and may stop in the bottom Čerenkov detector, causing a large scintillation signal. These events are removed by a cut on the top Čerenkov signal as illustrated in Fig. 6.2. This cut is 100% efficient and effective.

6.1.2 Determination of the Differential Flux

From the number of events ΔN_i in an energy bin i of width ΔE_i the differential flux is derived as:

$$\left(\frac{dN}{dE}\right)_i = \frac{1}{\Omega} \frac{\Delta N_i}{\Delta E_i} \frac{\omega_i}{\epsilon_i}, \quad (6.1)$$

with the total exposure Ω , the total efficiency ϵ_i , and the overlap correction ω_i . The weighted mean energy in a bin, is not at the center of the bin, but shifted to a smaller energy \hat{E} due to the steeply falling spectrum (see [50]). At this energy \hat{E} the flux is:

$$\frac{dN}{dE} = C \hat{E}^{-\alpha}. \quad (6.2)$$

For the number of events in bin i holds

$$\Delta N_i = \int_{E_i}^{E_{i+1}} C E^{-\alpha} dE, \quad (6.3)$$

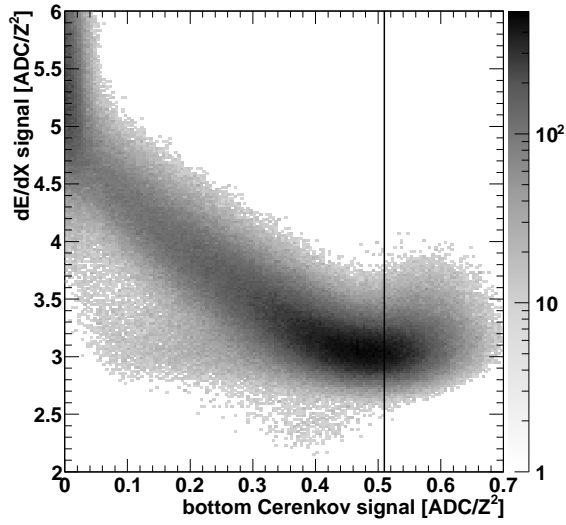


Figure 6.1: Proportional tube vs. Čerenkov signal (oxygen data). The minimum of the correlation is at minimum ionizing energy (2.78 GeV/amu) corresponding to signals of 3.07 in the dE/dX-array and 0.51 in the bottom Čerenkov (per Z^2). The cut to distinguish high energy events is illustrated by a line. Note that the z-scale is logarithmic.

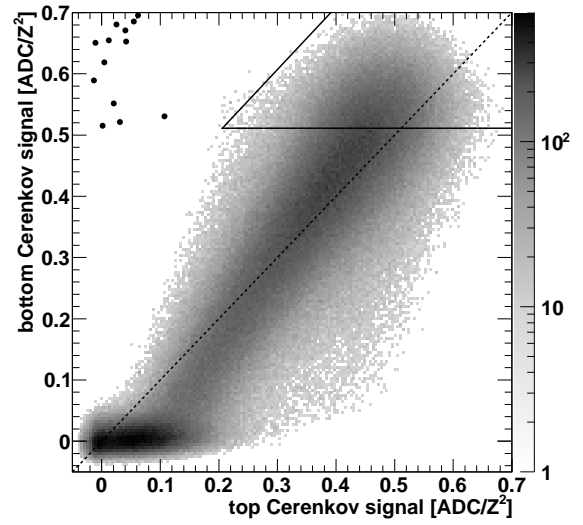


Figure 6.2: Correlation of Čerenkov signals (oxygen data). Events that suffer significant energy loss through the instrument are below the diagonal (dashed), fake high-energy events are above the diagonal (dots). Quality cut and high energy selection cut are indicated by solid lines. Note that the z-scale is logarithmic.

and then it follows for \hat{E} :

$$\hat{E} = \left[\frac{1}{\Delta E} \frac{1}{1-\alpha} \cdot (E_{i+1}^{1-\alpha} - E_i^{1-\alpha}) \right]^{-1/\alpha}. \quad (6.4)$$

The highest-energy data point in all spectra is an integral point. It is plotted at the median energy \hat{E}_{int} :

$$\hat{E}_{int} = \left[\frac{E_{low}^{1-\alpha}}{2} \right]^{1/(1-\alpha)}, \quad (6.5)$$

with the low edge of the integral bin E_{low} . The flux value of the integral bin at \hat{E}_{int} is

$$\left(\frac{dN}{dE} \right)_{int} = \Delta N_{int} \cdot \frac{1}{\Omega} \frac{\omega_{int}}{\epsilon_{int}} \frac{(\alpha-1) \hat{E}_{int}^{-\alpha}}{E_{low}^{1-\alpha}}. \quad (6.6)$$

The mean energy \hat{E} and the flux in the integral bin depend weakly on the power-law index α of the spectrum. An iterative procedure is used to take this dependence into account. The initial value of α is estimated from previous experiments, and is then in the next step modeled to match the present data. This process converges very fast and the spectra are stable after the second step.

Equations (6.1), (6.4) and (6.5), (6.6) define how to calculate the proper flux values and energies for the energy spectra of each element. In the following sections the necessary input values are described.

6.1.3 Event Counting and Efficiencies

To determine the energy of a particle different sub-detectors are used. Low-energy particles (below 3 GeV/amu), with a bottom Čerenkov signal of less than $0.51 \cdot Z^2$, are evaluated with the bottom Čerenkov signal. The remaining nuclei are evaluated with the dE/dX-array signal. If their TRD signal and dE/dX-array signal are high enough they are evaluated with the TRD signal. In this way, the spectra are split up into three separate energy regions commensurate with the energy ranges of the three sub-detectors.

The bins of the low-energy Čerenkov spectrum are defined in energy. The bin edges are set to 0.8, 1.0, 1.3, and 1.7 GeV/amu. For each event the measured signal is translated into an energy using the response function of the bottom Čerenkov detector. This energy is propagated through the detector and the residual atmosphere using the Bethe-Bloch formula (see Eq. (2.3)) and a detailed list of materials used in the instrument. At the top of the atmosphere the energy of the particle is estimated to be about 0.1 GeV/amu higher than at the bottom of the detector. The event is then registered in the appropriate energy bin.

The binning of the high-energy spectra (above 10 GeV/amu) is optimized in order to minimize the need for corrections. The bins are defined in signal space of the dE/dX-array and the TRD, and have to be at least 1.5 times as wide as the measured signal fluctuations. This keeps bin correlations at a moderate level. The lowest bin edge at about 10 GeV/amu, closest to the high-energy selection cut, is chosen to minimize the cut's influence on the spectrum. Bin correlations and the efficiency of the high-energy selection cut are described in detail in the next section (Sec. 6.1.4).

Two energy bins are realized for B, C, and O in the energy range of the dE/dX-array between 10 and 50 GeV/amu. Three bins could be used for iron in this range. For all elements one integral bin was used in the TR region above 1000 GeV/amu. The TR bin is at least 1.5 standard deviations in signal fluctuations separated from the highest dE/dX bin in order to avoid spillover.

Figure 6.3 illustrates high-energy data and binning for oxygen. About 500,000 oxygen events above 3 GeV/amu are shown in a correlation of the dE/dX-array signal and the TRD signal. Most of the events are clustered around the signal of particles at minimum ionizing energy ($3.07 \cdot Z^2$ in both signals: white marker in the figure). As the energy increases events start to climb towards higher signals along the diagonal since both signals are equal within fluctuations. Above about 780 GeV/amu the signal in the TRD is enhanced by transition radiation and events deviate upwards from the diagonal. The response function is indicated by the dash-dotted line. From all events, about 20 are possible TR events (thick markers). In this region the correlation plot is remarkably free of background. The dashed lines indicate the bin edges for the spectral analysis and correspond to 10, 90, 430, and 1500 GeV/amu.

Very similar correlation plots like Fig. 6.3 for oxygen, were evaluated for iron, carbon, and boron. For the light elements the same bins as for oxygen were used, since they were constructed to be 1.5 times as wide as the measured signal fluctuations for boron nuclei. The event counts and bin edges are summarized together with the flux values in Table 6.3 for carbon, oxygen and iron, as well as in Table 6.4 for boron.

Table 6.1 summarizes all exposure factors and efficiencies used to derive the spectra for

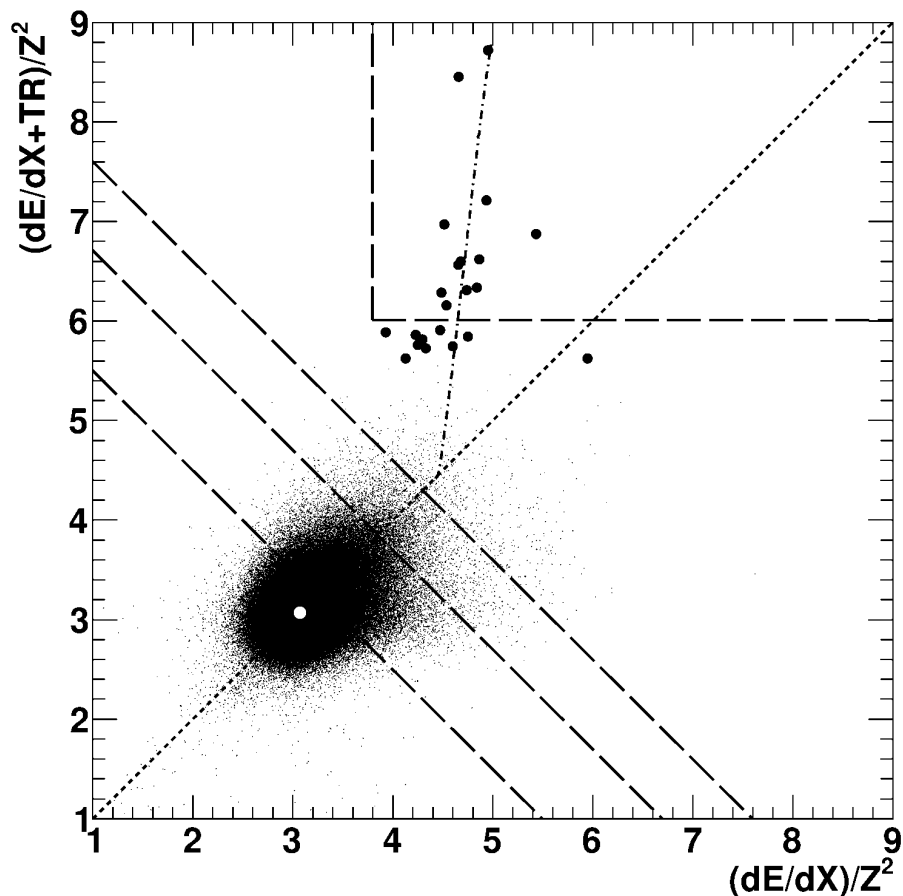


Figure 6.3: dE/dX -array signal versus TRD signal (measured in units of ADC/Z^2) for high energy oxygen data. The diagonal, the TRD response curve, and bin edges are indicated by lines. Possible TR events are shown in bold markers. See text for details.

boron, carbon, oxygen, and iron. The exposure is the product of the total active lifetime (see Section 2.5), effective aperture (Section 2.2.2), and surviving probability through the instrument and the atmosphere (Section 5.3). The resulting absolute normalization of the spectra is thus corrected for spallation losses and represents the flux at the top of the atmosphere.

Some of the efficiencies given in Table 6.1 depend on energy and nuclear charge. They are evaluated for all elements and energy regions separately. They represent the zenith-angle cut for the low-energy Čerenkov spectra, the tracking efficiency, the quality-cut efficiency, and the charge-selection efficiency. The total efficiency is the appropriate product of all efficiencies for a given element and energy region. The overall efficiency is dominated by the charge-selection efficiency and is about 50% for oxygen.

6.1.4 Evaluation of Bin Correlations

Bin correlations have to be accounted for from two effects: Correlations between bins in low-energy and high-energy spectra, which arise from the imperfection of the high-energy selection

Table 6.1: Summary of all efficiencies and exposure factors. Charge or energy dependent values are given for each element or energy range (denoted by the sub-detector used), respectively.

| item | spectrum | all elements | boron | carbon | oxygen | iron |
|--|----------|--------------|-------|--------|--------|------|
| exposure factor (m ² sr days) | all | — | 5.22 | 5.09 | 4.72 | 2.81 |
| zenith cut | CER | 0.043 | — | — | — | — |
| | dE/dX | — | — | — | — | — |
| | TRD | — | — | — | — | — |
| tracking efficiency | all | — | 0.90 | 0.92 | 0.92 | 0.94 |
| | | — | — | — | — | — |
| quality cuts | CER | — | 0.87 | 0.88 | 0.88 | 0.89 |
| | dE/dX | — | 0.88 | 0.89 | 0.90 | 0.88 |
| | TRD | — | 0.88 | 0.89 | 0.90 | 0.88 |
| charge cut | CER | — | 0.49 | 0.56 | 0.81 | 0.78 |
| | dE/dX | — | 0.36 | 0.44 | 0.68 | 0.67 |
| | TRD | — | 0.36 | 0.44 | 0.68 | 0.67 |

cut and correlations between adjacent energy bins due to the fluctuation of events between bins of a steeply falling spectrum. More events fluctuate upwards, into higher energy bins, than downwards. Thus, the uncorrected spectrum is too hard.

Both correlations arise from fluctuations in the measured signals. The signal fluctuations have been determined from data and are described in Section 2.3.3. Both correlation effects are taken into account by so-called “overlap corrections” simultaneously determined by a Monte Carlo simulation.

The Monte Carlo simulation is based on a model that assumes power-law spectra commensurate with previously published data. At high energy, spectral indices in agreement with the earlier TRACER measurements [12] are used. Other input parameters are the definition of the bins, the response functions of the sub-detectors, and the measured signal fluctuations.

The exact shape of the power law (i. e. the spectral index) and of the response functions (e. g. value of the relativistic rise, see Sec. 2.3) have only minor impact on the corrections. Also, the corrections are not sensitive to the width of the bins, provided they are at least 1.5 times as wide as the fluctuations of the measurement.

It was found that the overlap corrections are most sensitive to the measured signal fluctuations. This uncertainty is propagated to the correction factors and thus to the final spectra as a source of systematic uncertainty. In order to keep the statistical uncertainty to a minimum $30 \cdot 10^6$ events from 0.4 to 5000 GeV/amu were simulated for each element.

The individual correction for the high-energy selection cut depends strongly on the position of the low edge of the lowest dE/dX bin. This bin edge is chosen to result in a correction factor

close to unity.

The values of the factors needed to correct for bin correlations are derived from a matrix filled with simulated events according to the model described above. The matrix element M_{ij} is filled with events that should be in bin i (unfluctuated signal) but are counted in bin j (fluctuated signal). The diagonal entries are then correctly assigned events. One row and column of the matrix are used to evaluate the high-energy selection cut.

The combined correction factor for the two effects in bin i is the ratio of the sum over the corresponding row to the sum over the corresponding column:

$$\omega_i = \frac{\sum_j M_{ji}}{\sum_j M_{ij}} \quad (6.7)$$

Overlap corrections are always smaller than 1 and very close to unity for the Čerenkov and the TRD bins. Bins in the energy range of the dE/dX-array suffer larger corrections due to the poor energy resolution of this sub-detector. For example, overlap correction factors for carbon are 0.88 and 0.61 for the two dE/dX bins, respectively.

6.2 Energy Spectra of Iron, Oxygen, and Carbon

Here the energy spectra of the primary cosmic-ray elements iron, oxygen, and carbon are presented. For these elements no significant contributions from spallation of heavier nuclei in the atmosphere is expected. The differential fluxes have been propagated to the top of the atmosphere. They are presented as a function of kinetic energy per nucleon.

Table 6.3 summarizes the results: energy bins and the mean energy per bin (see Eq 6.4), number of events, and the resulting flux values. Uncertainties on the differential fluxes are given separately for statistical and systematic contributions. Figures 6.4, 6.5, and 6.6 present the measured energy spectra for iron, oxygen and carbon, respectively. They include previously published data for comparison. For clarity all spectra are also shown multiplied by $E^{2.65}$. The highest energy data point, the TRD bin, is an integral point for all elements.

The statistical uncertainties plotted in Figs. 6.4, 6.5, and 6.6 as error bars and given in Table 6.3 are based on Poisson counting statistics, with the uncertainty \sqrt{N} for N counted events. For ten and fewer events, errors are asymmetric and not equal to \sqrt{N} . Especially if just one event is counted, as in the highest energy bin for iron, the statistical uncertainty is +2.3 and -0.83 [32].

The systematic errors are evaluated taking into account uncertainties for overlap correction factors (i. e. signal fluctuations), calculated efficiencies, and imperfect knowledge of the response functions. For these, uncertainties are assumed in the estimated signal at the energy of minimum ionizing particles (MIP), normalization of the Čerenkov response function, relativistic rise in the dE/dX-array, energy of TR onset, and the magnitude of the TR signal truncation due to the new gas mixture. All these parameters of the response functions are mentioned in Section 2.3. Additionally, a systematic uncertainty stems from the assumed spectral indices used to calculate integral fluxes and plot energies \hat{E} . The individual values of the assumed uncertainties are given in Table 6.2. The resulting total systematic uncertainty is evaluated

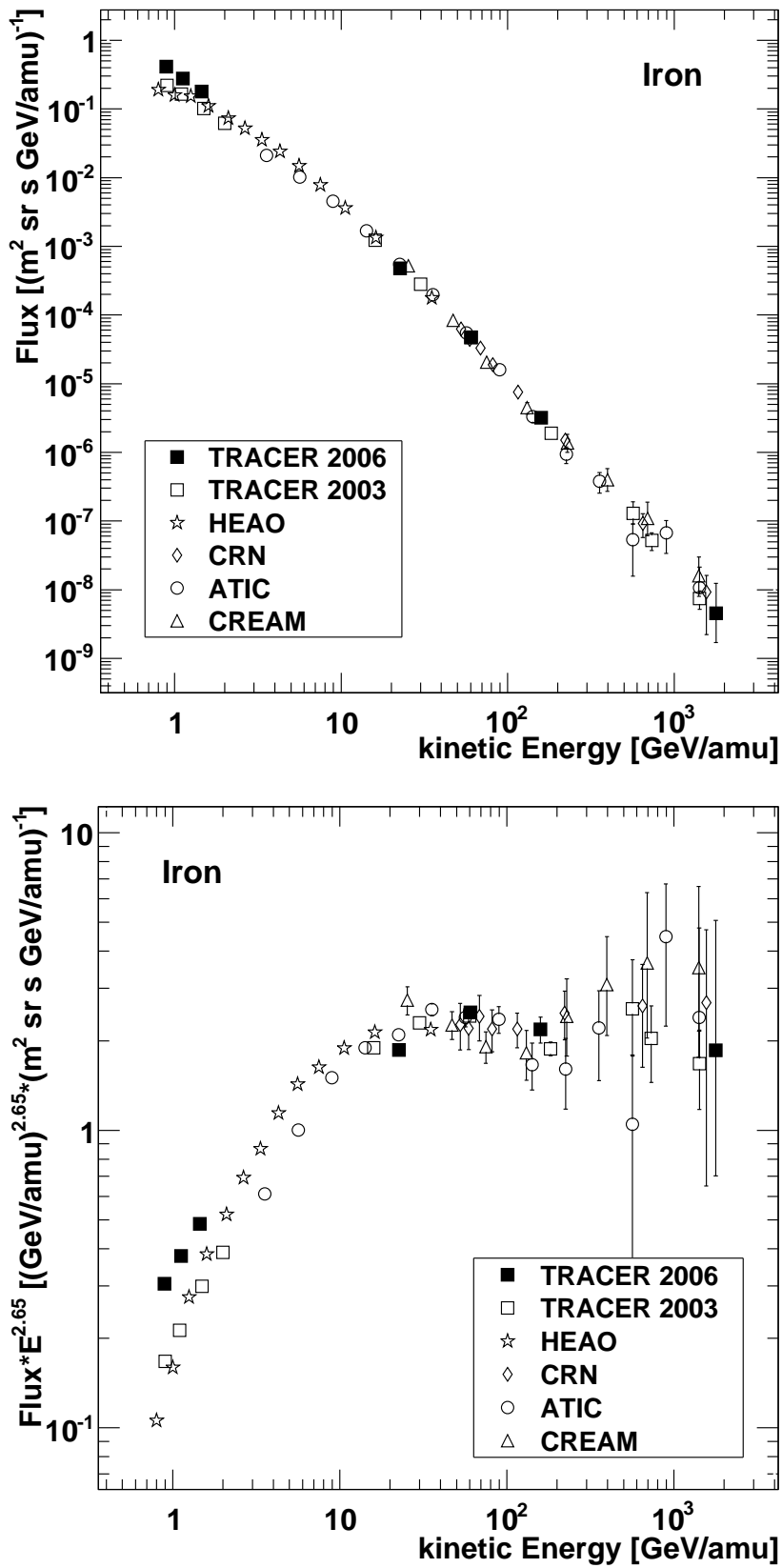


Figure 6.4: Differential energy spectrum of iron as derived in this thesis. The spectrum is multiplied by $E^{2.65}$ in the lower panel for clarity. For comparison, results from HEAO [27], CRN [60], ATIC [65], and CREAM [5] are shown. The error bars are statistical only.

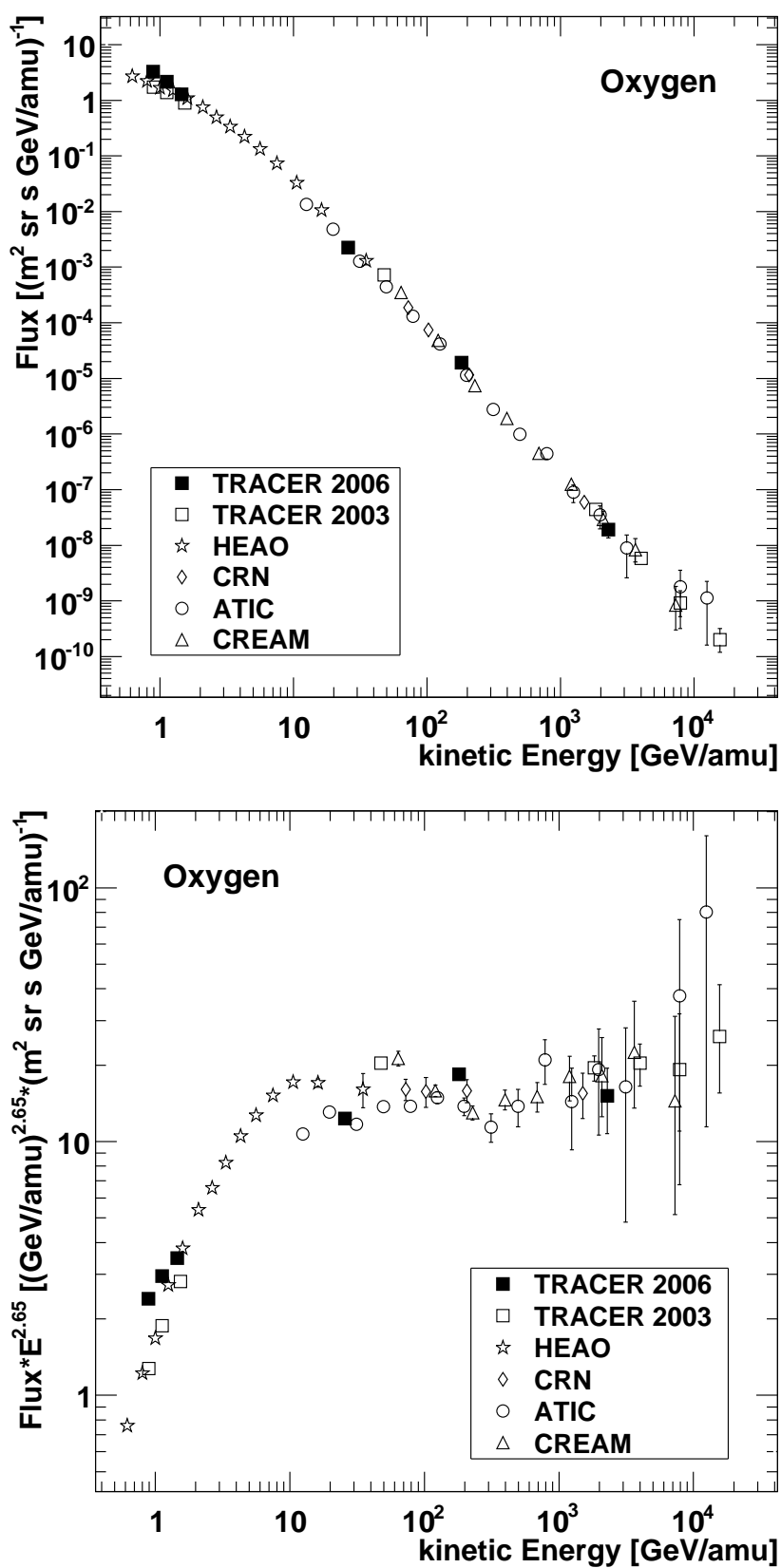


Figure 6.5: Differential energy spectrum of oxygen as derived in this thesis. The spectrum is multiplied by $E^{2.65}$ in the lower panel for clarity. For comparison, results from HEAO [27], CRN [60], ATIC [65], and CREAM [5] are shown. The error bars are statistical only.

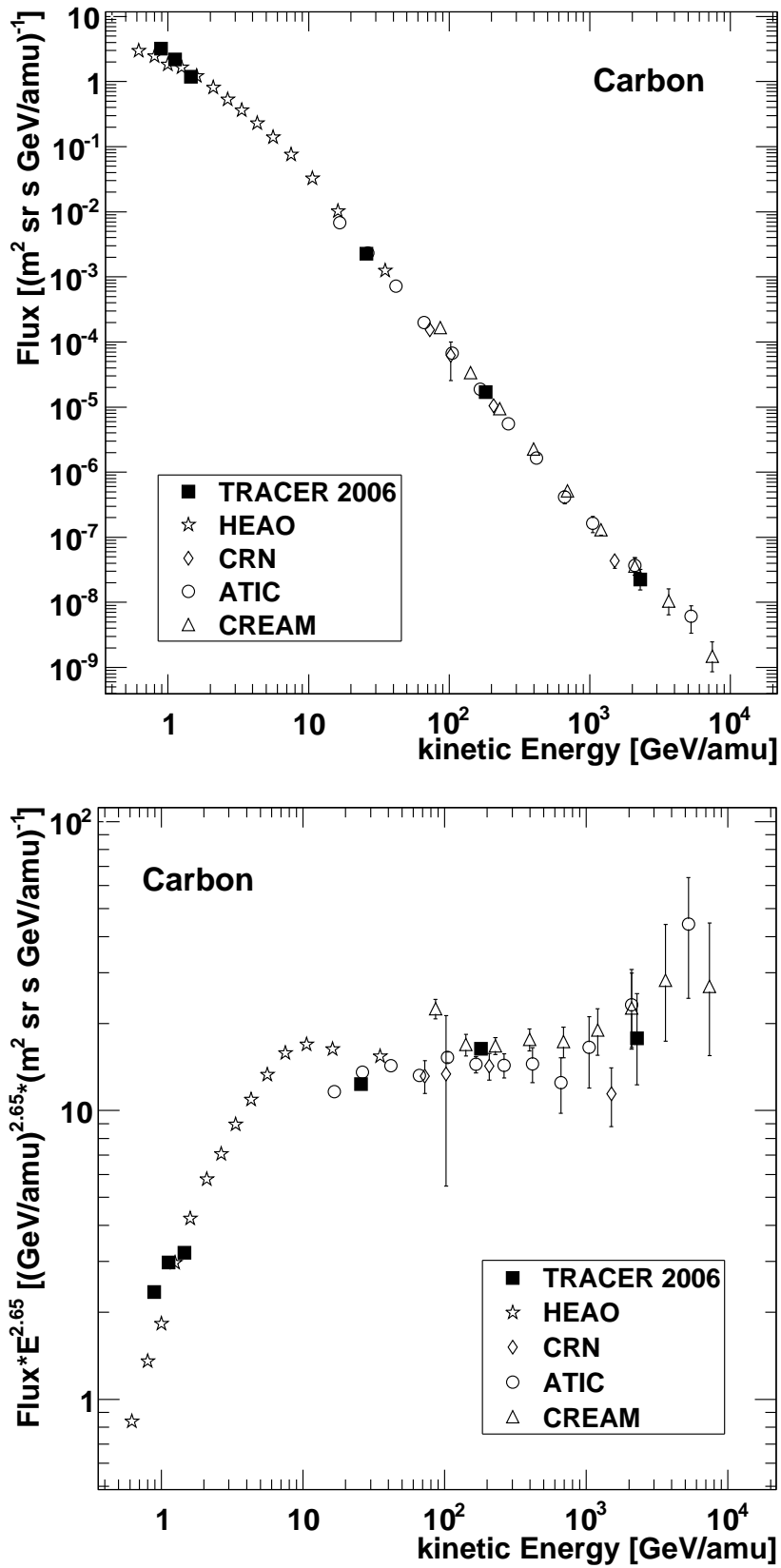


Figure 6.6: Differential energy spectrum of carbon as derived in this thesis. The spectrum is multiplied by $E^{2.65}$ in the lower panel for clarity. For comparison, results from HEAO [27], CRN [60], ATIC [65], and CREAM [5] are shown. The error bars are statistical only.

Table 6.2: Sources of systematic uncertainties, their central values, and their absolute uncertainties assumed.

| Source | Central Value | Uncertainty |
|---|--------------------------|-----------------------|
| Signal Fluctuations | 7.3% (B) to 3.8% (Fe) | 0.4% (B) to 0.2% (Fe) |
| Efficiencies | $\approx 50\%$ | $\approx 3\%$ |
| CER Normalization at MIP | 0.51 | 0.04 |
| Relativistic Rise | 33% | 2% |
| dE/dX Signal for MIP | 3.07 | 0.03 |
| dE/dX Signal at TR onset | 4.45 | 0.05 |
| TR truncation | 19% | 3% |
| Spectral Index α | 2.65 ($E > 16$ GeV/amu) | 0.1 |

by calculating the elemental spectra assuming the outlined parameters at their 1σ values for maximum and minimum resulting, measured flux. This flux range defines the 1σ systematic uncertainty of the measurement.

For the low-energy Čerenkov spectrum the systematic uncertainty is small and comes mainly from the limited knowledge of the response function. Between 10 and 500 GeV/amu, for the dE/dX spectrum, the uncertainty of the response function and of the overlap correction factors are the main contributions. The highest energy spectral data points are most sensitive to the uncertainty in the energy of TR onset.

The limited knowledge of the exact response functions contributes the most to the systematic uncertainties. This could be avoided by an end-to-end calibration of the detector at accelerators. Such a calibration is possible for the whole energy range of the detector and was conducted before the Antarctic flight in 2003. The detector upgrades before the most recent flight (see Sec. 2.2.1) necessitated adjustments to this calibration, which leads to the large systematic uncertainties, especially at highest energies.

The uncertainties affect both, energy and flux measurements. All uncertainties, also the uncertainty in the energy measurement, were propagated to the flux values. In order to do this the spectral fluxes were evaluated with the steepest and with the most shallow response functions within the systematic uncertainties. The resulting fluxes represent the lower and upper systematic uncertainties in the flux measurement due to the uncertainty in the energy determination.

For iron the systematic uncertainties are affected by an additional effect: The dE/dX-array and TRD signals for iron nuclei are slightly decreased because of a space charge effect in the proportional tubes. Vertical incident iron nuclei especially produce a dense electron cloud in the Xe gas that shields off some of the electric potential, which effectively reduces the tube gain by about 7%. This effect is taken into account as an additional source of systematic uncertainty. The space charge effect is not noticeable for any other elements.

Compared to the earlier measurements from TRACER in 2003 [12, 13], the new energy spectra for oxygen and carbon could be composed with two energy bins in the energy region between 10 and 500 GeV/amu instead of one. This is possible because of the improved energy

resolution in the dE/dX -array compared to the earlier flight. The agreement of the two data sets suggests similar values of observed spectral index and absolute normalization.

It is evident from Figures 6.4, 6.5, and 6.6 that the new results are also in good agreement with previous measurements from HEAO [27], CRN [60], ATIC [65], and CREAM [5]. Although the new measurements have less statistics than TRACER's earlier ones from 2003, the statistical accuracy is similar to those of the other balloon-borne experiments ATIC and CREAM and exceed those of the space missions HEAO and CRN. The newly measured spectra reach an energy of up to 2 TeV/amu.

The differential intensities at low energy are consistently higher compared to previous measurements. This can be attributed to the different solar modulation of low-energy cosmic rays ($E \lesssim 10$ GeV/amu) at the time of the flight. Solar modulation is the suppression of cosmic-ray flux due to solar activity and follows the 11-year solar cycle. It stems from the interaction of the charged cosmic-ray particles with the solar wind. In the force-field approximation solar modulation is described by the parameter Φ , which is the mean energy loss of a particle in the interplanetary medium [20, 34]. It is proportional to the modulation parameter ϕ , which is measured in volts and to which the low-energy cosmic-ray flux is inversely proportional. The modulation parameter ϕ was determined by ACE [94] for the time of the TRACER flights. It was 1030 MV for the Antarctic flight in 2003 and 450 MV for the flight from Sweden in 2006. The quantitative effect of solar modulation is charge dependent.

The agreement of elemental spectra of iron and oxygen with previous measurements, especially with the earlier measurements by TRACER, shows that the new measurement and its analysis are consistent. This gives confidence for the validity of the results for the lighter elements carbon and boron, which represent new measurements for TRACER.

6.3 Energy Spectrum of Boron

For boron, special care has to be taken in determining the energy spectrum. Contamination from carbon and production of boron in the atmosphere can bias the measured spectrum. These effects are treated in the following sections before the boron spectrum is presented.

6.3.1 Carbon Contamination

Due to the finite charge resolution and the large abundance of carbon some carbon events will contaminate the selected boron sample. As outlined in Section 5.4, the charge selection cut used for boron is optimized for efficiency under the constraint of low contamination.

At low energies (i. e. below 3 GeV/amu), no significant contamination is found in the large number of boron events due to the good charge resolution.

At high energies, above 3 GeV/amu, the relative amount of carbon to boron is higher and the charge resolution is reduced. Thus, a significant contamination of the boron sample by carbon nuclei is expected. In Section 5.5, it was found that the high-energy boron sample of about 40,000 events contains 250 carbon events. Placing a cut on the maximum Čerenkov

Table 6.3: Flux and energy values of the spectra of primary cosmic-ray species measured with TRACER in 2006. The kinetic Energy \hat{E} in each bin is derived according to Eq. (6.4). The number of events counted in each bin is stated.

| Element | Energy Range (GeV/amu) | Kinetic Energy \hat{E} (GeV/amu) | Number of Events | Flux $\pm \sigma_{stat} \pm \sigma_{sys}$ ($\text{m}^2 \text{ s sr GeV/amu}$) ⁻¹ |
|--------------------|---------------------------|---------------------------------------|---------------------|--|
| Fe (Z = 26) | 0.8 - 1.0 | 0.9 | 593 | $(4.14 \pm 0.2 \pm 0.1) \times 10^{-1}$ |
| | 1.0 - 1.3 | 1.1 | 487 | $(2.78 \pm 0.1 \pm 0.09) \times 10^{-1}$ |
| | 1.3 - 1.7 | 1.5 | 386 | $(1.79 \pm 0.07 \pm 0.2) \times 10^{-1}$ |
| | 14 - 38 | 23 | 1180 | $(4.8 \pm 0.1 \pm 1.3) \times 10^{-4}$ |
| | 38 - 101 | 60 | 314 | $(4.7 \pm 0.2 \pm 1.7) \times 10^{-5}$ |
| | 101 - 264 | 159 | 57 | $(3.2 \pm 0.3 \pm 1.4) \times 10^{-6}$ |
| | 1200 - | 1800 | 1 | $(4.5 \pm_{3.7}^{10} \pm_{3.2}^{2.1}) \times 10^{-9}$ |
| O (Z = 8) | 0.8 - 1.0 | 0.9 | 7900 | $(3.26 \pm 0.04 \pm 0.09) \times 10^0$ |
| | 1.0 - 1.3 | 1.1 | 6440 | $(2.17 \pm 0.03 \pm 0.05) \times 10^0$ |
| | 1.3 - 1.7 | 1.5 | 6210 | $(1.28 \pm 0.02 \pm 0.05) \times 10^0$ |
| | 9.5 - 87 | 26 | 43700 | $(2.2 \pm 0.01 \pm 0.06) \times 10^{-3}$ |
| | 87 - 432 | 181 | 2140 | $(1.9 \pm 0.04 \pm_{0.8}^{0.6}) \times 10^{-5}$ |
| | 1500 - | 2300 | 12 | $(1.9 \pm 0.6 \pm_{1.1}^{0.8}) \times 10^{-8}$ |
| C (Z = 6) | 0.8 - 1.0 | 0.9 | 6510 | $(3.19 \pm 0.04 \pm 0.1) \times 10^0$ |
| | 1.0 - 1.3 | 1.1 | 5460 | $(2.19 \pm 0.03 \pm 0.1) \times 10^0$ |
| | 1.3 - 1.7 | 1.5 | 4760 | $(1.19 \pm 0.02 \pm 0.1) \times 10^0$ |
| | 9.5 - 87 | 26 | 28300 | $(2.3 \pm 0.01 \pm 0.06) \times 10^{-3}$ |
| | 87 - 432 | 181 | 1430 | $(1.7 \pm 0.04 \pm_{0.7}^{0.5}) \times 10^{-5}$ |
| | 1500 - | 2300 | 10 | $(2.2 \pm_{0.7}^{0.9} \pm_{1.3}^{0.9}) \times 10^{-8}$ |

signal at $0.7 \cdot Z^2$, the carbon events contaminating the boron sample are restricted to an energy of about 3 GeV/amu.

Figure 6.7 shows a scatter plot of the boron data in the correlation of the dE/dX-array signal versus the TRD signal. The black markers represent the boron data, which center around the coordinates of the energy of minimum ionizing particles (white marker), while high-energy events reach upwards along the diagonal (medium black markers) as both signals are still the same within fluctuations. Finally, some events at very high energies above 780 GeV/amu stand out above the diagonal (thick black markers) as transition radiation enhances the signal in the TRD.

Also shown in Figure 6.7 is a simulated representation of 250 carbon events of an energy of about 3 GeV/amu (circles). They are distributed around the signal coordinates of minimum ionizing energy, shifted by a factor of $Z_C^2/Z_B^2 = 36/25$ in accordance with them being falsely assumed to be boron nuclei, and with fluctuations as determined for carbon from data (9%, 8 layers).

Many such representations are used to determine the average contamination in each energy

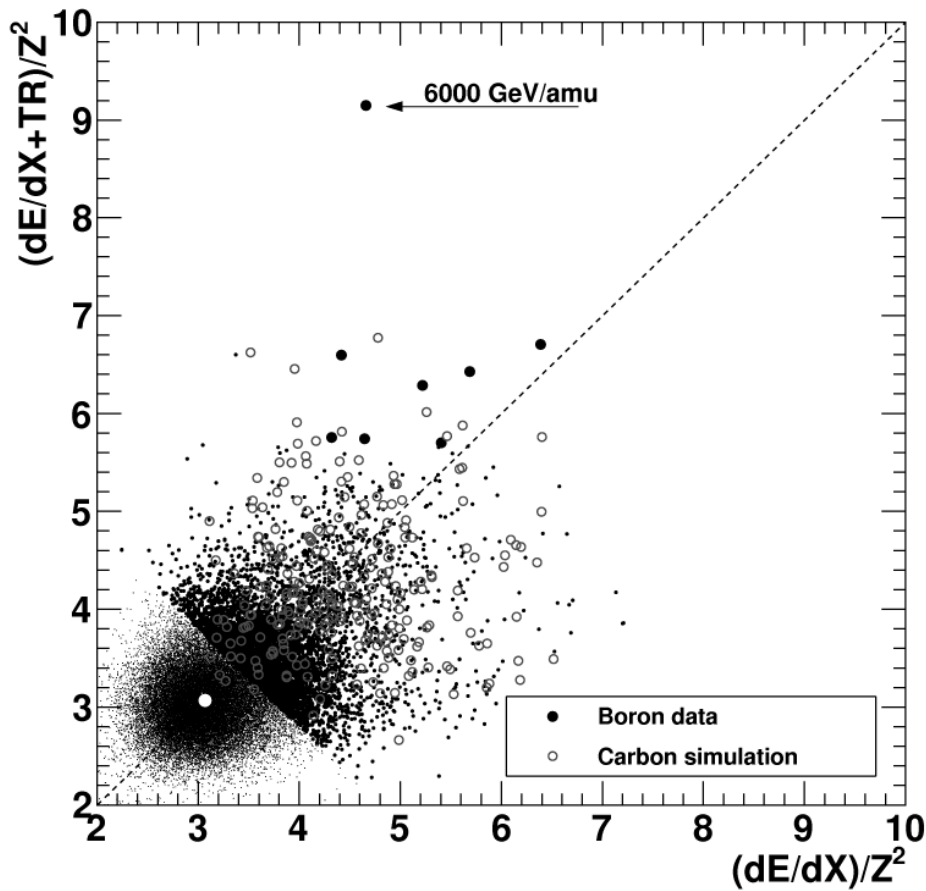


Figure 6.7: dE/dX -array signal versus TRD signal (measured in units of ADC/Z^2) for high energy boron data (40,000 events). Small, medium and thick black markers represent boron data, circles indicate carbon contamination (250 events, MC simulated). Minimum ionizing energy is indicated as a white marker. See text for details.

bin, where the simulation generates 250 ± 12 carbon events according to a normal distribution. It is found that many events fall between dE/dX and TRD bins, so that the contamination for the dE/dX bins is small, and that on average one event in the TRD bin is a true boron event. As indicated in Fig. 6.7 the highest energy event in the boron sample is at about 6000 GeV/amu. This event is about 5σ outside the simulated carbon distribution and has a probability of 10^{-5} of being a carbon nucleus (i. e. one could expect 0.003 carbon nuclei at this position). Therefore, the event represents the highest-energy cosmic-ray boron nucleus ever recorded.

The exact amount of contamination in each bin is subtracted from the sampled events. They are given in Table 6.4.

6.3.2 Atmospheric Production

All cosmic-ray nuclei traversing matter may undergo spallation. Only the surviving fraction at the bottom of the instrument is used for the measurement. The relative amount of interacting

nuclei for each element is calculated as outlined in Section 5.3. This is applied as a factor reducing the effective exposure of the experiment.

But a cosmic-ray species does not only suffer losses, it is also produced as the result of spallation of heavier nuclei. This effect is negligible for carbon, oxygen, and iron because of the low abundances of their neighbors and the small partial cross sections for spallation products heavier than protons. For boron however, gains due to spallation of carbon and oxygen are significant, because their abundances are high, while boron's is low.

The amount of boron produced in the atmosphere can be estimated using partial cross sections, or inferred from the measured rates themselves. During the flight the instrument samples data at different altitudes and thus different column densities of atmosphere above it. This is evident in the flight profile given in Figure 2.2. The ambient pressure p in units of hPa is converted to vertical column density ρ in units of g/cm^2 according to

$$\rho = p \cdot \frac{10}{g} = p \cdot \frac{10}{9.81 \text{ m/s}^2}, \quad (6.8)$$

with the gravitational acceleration $g = 9.81 \text{ m/s}^2$. For the analysis, the average column density that the cosmic-ray particles encounter has to be used. Thus, the measured vertical column density is scaled by 15% as the average incident angle is 30° .

Without atmospheric production, the data rate R , e. g. for oxygen, varies with atmospheric depth ρ as

$$R_O = R'_O \cdot e^{-\rho/\Lambda_O} \approx R'_O \cdot \left(1 - \frac{\rho}{\Lambda_O}\right), \quad (6.9)$$

with the rate at the top of the atmosphere R'_O and the spallation pathlength Λ_O . The spallation pathlength is connected to the total cross section σ_O for a target with atomic mass m as

$$\Lambda_O = \frac{m}{\sigma_O}. \quad (6.10)$$

In Figure 6.8 the measured rate of oxygen is shown as a function of column density ρ , which was derived from ambient pressure measurements during flight. The solid line represents the best fit to the data according to Eq. (6.9) with a result of $\Lambda_O = 23.4 \pm 7.3 \text{ g}/\text{cm}^2$, with the uncertainty range depicted as dashed lines. The dotted line indicates a calculated prediction of $\Lambda_O = 24.6 \text{ g}/\text{cm}^2$ based on the Bradt-Peters formula, Eq. (5.7), to derive total cross sections. Although the uncertainty of the measurement is rather large because of the narrow range of column density encountered, the result is in excellent agreement with the calculated prediction.

The same procedure for iron and carbon also results in measured total spallation pathlengths commensurate with the Bradt-Peters calculation. The result for iron is a measured $\Lambda_{Fe} = 11.5 \pm 4 \text{ g}/\text{cm}^2$, compared to a calculated value of $14.2 \text{ g}/\text{cm}^2$. For carbon the measured value is $\Lambda_C = 38.6 \pm 8.4 \text{ g}/\text{cm}^2$, which is slightly larger than the calculated pathlength of $27.4 \text{ g}/\text{cm}^2$. However, if the production of carbon due to spallating oxygen is not ignored, the effective pathlength for carbon loss in the atmosphere, using the proper partial cross sections, is $32.1 \text{ g}/\text{cm}^2$. This value provides a better agreement with the fit. This consideration of carbon production in the atmosphere shifts the overall carbon abundance by about 2%, which was taken into account for the carbon spectrum and, thus, also for the boron-to-carbon ratio.

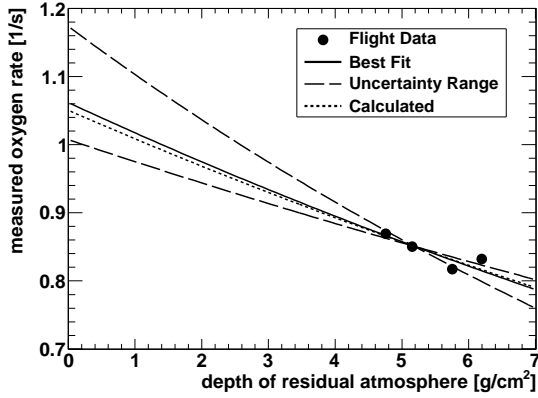


Figure 6.8: Oxygen rate as a function of atmospheric depth. The best fit to the data (solid line) is shown, as well as its uncertainty range (dashed), and the prediction based on partial cross sections (dotted). See text for notes on fit and calculation.

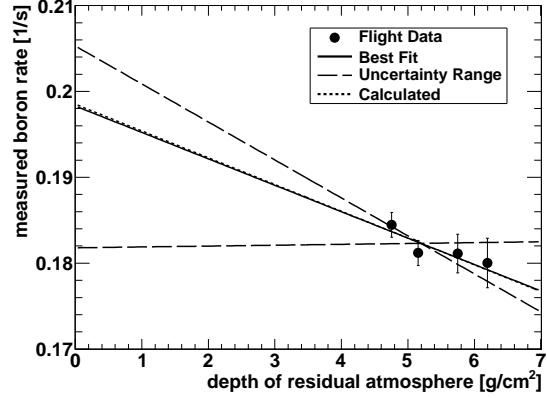


Figure 6.9: Boron rate as a function of atmospheric depth. The best fit to the data (solid line) determines the production of boron from carbon and oxygen in the atmosphere. The range of the fit uncertainty (dashed) is shown, as well as the prediction based on partial cross sections (dotted).

The results of the analysis of the elemental event rate as a function of atmospheric overburden lead to the conclusion that the formalism used to calculate the total cross sections is sound and reproduces the needed pathlengths accurately.

In a next step the rate of boron is analyzed as a function of column density. Because boron production from heavier nuclei is not negligible, the rate R_B at the top of the instrument is:

$$\begin{aligned} R_B &= R'_B \cdot \left(1 - \frac{\rho}{\Lambda_B}\right) + R'_C \frac{\rho}{\Lambda_{C \rightarrow B}} + R'_O \frac{\rho}{\Lambda_{O \rightarrow B}} \\ &= R'_B \cdot \left[1 - \rho \left(\frac{1}{\Lambda_B} - \frac{k_C}{k_B} \frac{1}{\Lambda_{\rightarrow B}}\right)\right], \end{aligned} \quad (6.11)$$

where R'_i is the rate at the top of the atmosphere for element i , Λ_B is the spallation pathlength for boron, and $\Lambda_{C \rightarrow B}$ and $\Lambda_{O \rightarrow B}$ are the production pathlengths for boron from carbon and oxygen. It is assumed here that only carbon and oxygen contribute significantly to the boron production, since the abundance of nitrogen is very low at the top of the atmosphere. Also it is assumed that the energy per nucleon (or Lorentz factor) is preserved in nuclear interactions.

To simplify the equation, the abundance ratio k_C/k_B of carbon to boron at the top of the atmosphere is used, as well as the ratio of oxygen to carbon k_O/k_C in the effective production pathlength $\Lambda_{\rightarrow B}$:

$$\frac{1}{\Lambda_{\rightarrow B}} = \frac{1}{\Lambda_{C \rightarrow B}} + \frac{k_O}{k_C} \frac{1}{\Lambda_{O \rightarrow B}}. \quad (6.12)$$

The ratio of oxygen to carbon is assumed to be independent of energy and close to unity as can be inferred from Table 6.3 or in [5, 83].

Figure 6.9 shows the measured boron rate as a function of column density ρ . The best fit (Eq. (6.11)) is indicated as a solid line with the error range depicted as two dashed lines. The

data are restricted in energy to 3–9 GeV/amu for which the ratio k_C/k_B is 4.35 according to HEAO data [27]. The fit also assumes the spallation pathlength to be 28.7 g/cm², as calculated from Eq. (5.7). The free parameters of the fit are thus the normalization R'_B and the effective production pathlength $\Lambda_{\rightarrow B}$, which is estimated to:

$$\Lambda_{\rightarrow B} = 225 \pm 102 \text{ g/cm}^2. \quad (6.13)$$

The dotted line in Fig. 6.9 represents a predicted curve on the basis of partial cross sections measured by Webber et al. [90]. The effective boron production pathlength $\Lambda_{\rightarrow B}$ is calculated to be:

$$\Lambda_{\rightarrow B} = \frac{m_{\text{Air}}}{f_C \sigma_{C \rightarrow B} + f_O \sigma_{O \rightarrow B}} = 227.3 \pm 44 \text{ g/cm}^2, \quad (6.14)$$

with the average atomic mass of air m_{Air} (79% N₂ and 21% O₂: 29 amu), the partial cross sections given by Webber et al. [90] at 1.5 GeV/amu for a carbon target. The given partial cross section have been determined for a carbon target. They have been scaled to the target material of air by the factors f_C and f_O . The scaling factors can be evaluated using the proportionality of the partial cross sections to the total cross sections [89]. These are in turn proportional to $(A_T^{1/3} + A_I^{1/3} - b)^2$ according to Eq. (5.7) with $b = 0.83$. Therefore the scaling factors are

$$f_{C/O} = \frac{(A_{\text{Air}}^{1/3} + A_{C/O}^{1/3} - b)^2}{(A_C^{1/3} + A_{C/O}^{1/3} - b)^2}. \quad (6.15)$$

The uncertainty of the calculated pathlength is due to a 10% error assumed for k_O/k_C , which is set to unity, and a 25% uncertainty in the partial cross sections. Although the reported uncertainty of their measurement is very small (3%), a larger error is assumed due to differences of the values to other measurements (e. g. [85]), to a possible change from the measurement energy of 1.5 GeV/amu to the energy range of this measurement, and to the necessary scaling factor.

The atmospheric production of boron has to be subtracted from the measured flux. The average column density above the TRACER detector encountered by a cosmic-ray particle at the average angle of incidence of 30° is $\hat{\rho} = 5.2 \text{ g/cm}^2$. The corrected flux is

$$N_B = N'_B - N'_C \cdot \frac{\hat{\rho}}{\Lambda_{\rightarrow B}} \exp(\hat{\rho}/\Lambda_B), \quad (6.16)$$

with the measured fluxes corrected for spallation losses N'_B and N'_C . The effective production pathlength of boron $\Lambda_{\rightarrow B}$, and the spallation pathlength of boron in the atmosphere Λ_B . The correction factor takes into account spallation processes in the atmosphere and the detector as the fluxes are determined at the bottom of the instrument. Processes that require two or more interactions in the atmosphere or in the detector are neglected. The correction for the boron-to-carbon ratio (B/C) is then

$$\left(\frac{B}{C}\right)_{\text{top}} = \frac{N'_B}{N'_C} - \frac{\hat{\rho}}{\Lambda_{\rightarrow B}} \exp(\hat{\rho}/\Lambda_B). \quad (6.17)$$

Assuming all cross sections to be independent of energy in the energy range of the measurement and the oxygen to carbon ratio k_O/k_C to be constant with energy, the correction to the boron-to-carbon ratio is a constant.

In this work the calculated, effective boron production pathlength $\Lambda_{\rightarrow B} = 227 \pm 44 \text{ g/cm}^2$ is used. It still has the advantage of the smaller uncertainty compared to the measured production pathlength. The correction factor used in this work is

$$\frac{\hat{\rho}}{\Lambda_{\rightarrow B}} \exp(\hat{\rho}/\Lambda_B) = 0.027 \pm_{0.004}^{0.007}. \quad (6.18)$$

It is important to note, that both the pathlengths measured here and that determined from measured cross sections do agree well within their uncertainties. The method of estimating the production of boron in the atmosphere outlined in this section can be a powerful tool for future cosmic-ray measurements. It has already proven to be able to reproduce the values for the production pathlengths from a calculation using partial cross sections. With better experimental statistics it would be possible to arrive at precise numerical values for production pathlengths at high energies. These can be more precise at the energies needed for cosmic-ray measurements than the extrapolation of currently available accelerator measurements.

6.3.3 The Spectrum of Boron

The spectrum of boron is presented in Table 6.4 and in Figure 6.10 as a function of kinetic energy per nucleon. It is compared to the carbon spectrum and to the results of previous experiments. The table states the energy bins, the kinetic energy at which the derived flux is valid, the number of boron events in a bin, the number of carbon contaminants in a bin, and the derived flux with its statistical and systematic uncertainties.

The measured spectrum contains in its highest energy bin one event of about 6000 GeV/amu in energy. Due to the nature of the construction of the spectrum, this leads to a flux of $3.5 \times 10^{-9} \text{ 1/(m}^2 \text{ s sr GeV/amu)}$ at an energy of about 2000 GeV/amu. This highest energy boron event has a chance of about 20% to be atmospheric instead of cosmic in origin. Thus, it might be prudent to think of this data point as an upper limit.

All sources of systematic uncertainties detailed for the heavier elements are also considered for boron (see Sec. 6.2). An additional uncertainty was introduced due to the subtraction of atmospheric production of boron from carbon and oxygen. Contrary to other systematic uncertainties, this one does not cancel for the boron-to-carbon ratio.

The subtraction of carbon contamination was done prior to evaluating the statistical uncertainty. Thus, the statistical uncertainty stated for the highest energy bin is the uncertainty of counting one event (see [32]). This is a different uncertainty as compared to counting “5 – 4” events. This is motivated by the fact that the one boron count is not a result of a statistical method but could be identified clearly as the only boron event in the bin.

The overall agreement with previous experiments is good. Only HEAO and CRN previously reported absolute boron spectra, which are exceeded in energy by this measurement. Other experiments determined only the ratio of boron to carbon. The boron spectrum is clearly steeper than the carbon spectrum. A detailed comparison of the boron and carbon spectra is conducted in the next chapter with regard to the boron-to-carbon ratio.

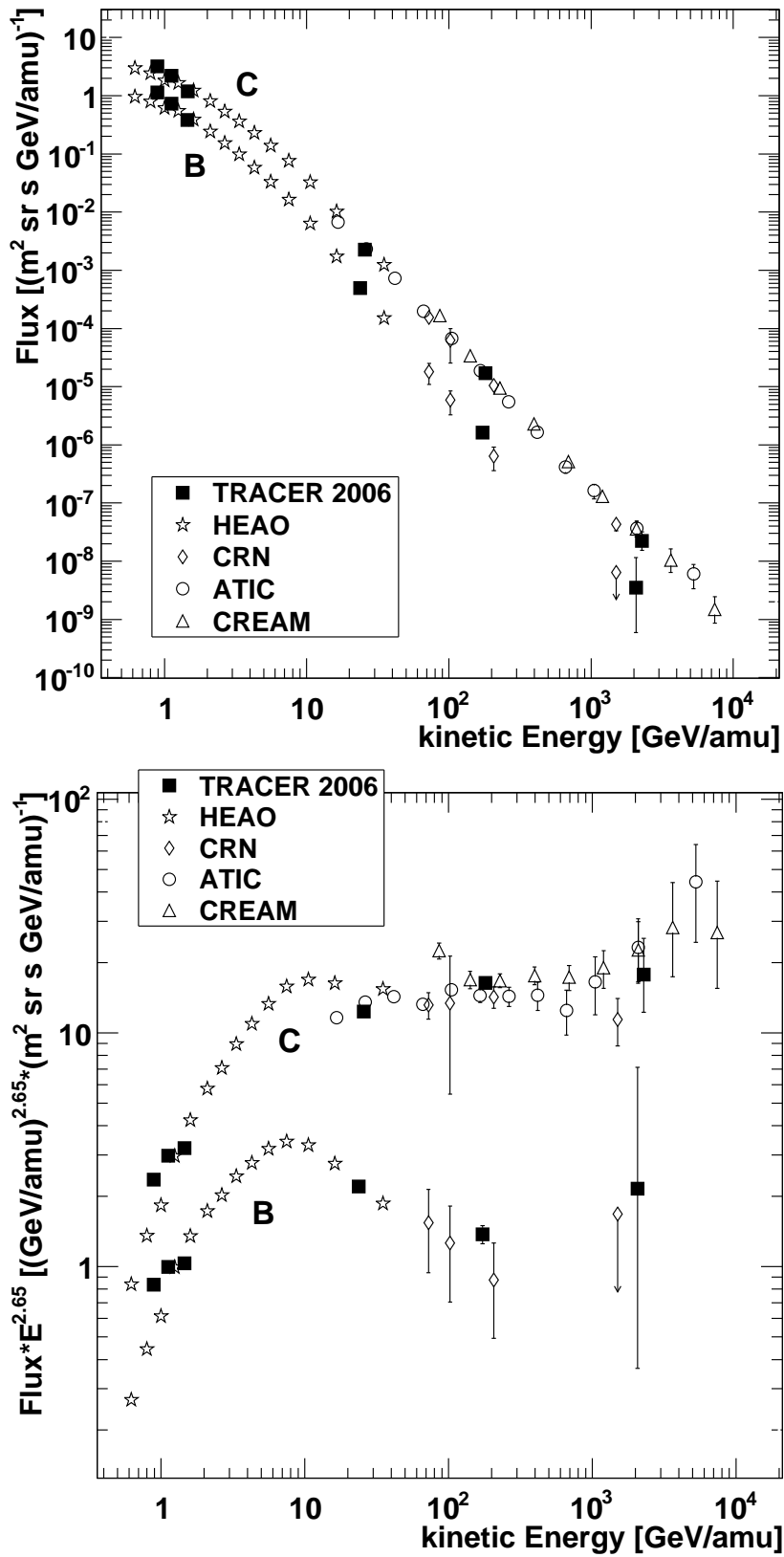


Figure 6.10: Spectrum of boron as derived in this thesis. In a logarithmic representation (upper panel) and additionally multiplied by $E^{2.65}$ (lower panel). It is compared to carbon and previous experiments (HEAO [27], CRN [83], ATIC [65], and CREAM [5]). Note that only HEAO and CRN reported absolute boron spectra. The error bars are statistical only.

Table 6.4: Flux and energy values of the spectrum of boron. The mean kinetic Energy \hat{E} is derived according to Eq. (6.4). Where applicable the number of estimated carbon events in the boron sample is given.

| Element | Energy Range (GeV/amu) | Kinetic Energy \hat{E} (GeV/amu) | Number of B events | Number of C events | Flux $\pm \sigma_{stat} \pm \sigma_{sys}$ ($\text{m}^2 \text{ s sr GeV/amu}$) ⁻¹ |
|------------------|---------------------------|---------------------------------------|-----------------------|-----------------------|--|
| B (Z = 5) | 0.8 - 1.0 | 0.9 | 2170 | — | $(1.1 \pm 0.03 \pm 0.1) \times 10^0$ |
| | 1.0 - 1.3 | 1.1 | 1600 | — | $(7.3 \pm 0.2 \pm 0.1) \times 10^{-1}$ |
| | 1.3 - 1.7 | 1.5 | 1280 | — | $(3.8 \pm 0.1 \pm 0.1) \times 10^{-1}$ |
| | 9.5 - 86.5 | 23.8 | 7200 | 27 | $(4.9 \pm 0.07 \pm 1.0) \times 10^{-4}$ |
| | 86.5 - 432 | 173 | 413 | 48 | $(1.6 \pm 0.1 \pm 0.4) \times 10^{-6}$ |
| | 1500 - | 2070 | 5 | 4 | $(3.5 \pm_{2.9}^{8.1} \pm 1.7) \times 10^{-9}$ |

CHAPTER 7

THE BORON-TO-CARBON RATIO AND ITS IMPLICATIONS

The boron-to-carbon abundance ratio of Galactic cosmic radiation is presented and discussed in this chapter.

7.1 The Boron-to-Carbon Ratio

The boron-to-carbon abundance ratio (B/C) is calculated from the differential intensities presented in the previous chapter. Although the same energy intervals have been used to derive the energy spectra, the mean energy in each bin differs slightly because of the different spectral indices. The boron spectrum is steeper than the carbon spectrum, resulting in an about 10% lower mean energy \hat{E} (see Eq. (6.4)). For the ratio, the carbon flux is scaled to the boron energies \hat{E}_B using the spectral index α of the carbon spectrum:

$$N_C(\hat{E}_B) = N_C(\hat{E}_C) \cdot \left(\frac{\hat{E}_B}{\hat{E}_C} \right)^{-\alpha}. \quad (7.1)$$

Above 20 GeV/amu, the index α is 2.65, in agreement with the TRACER measurements. Below that energy α is chosen to be commensurate with low-energy measurements from HEAO [27].

Table 7.1 presents the resulting boron-to-carbon abundance ratio as a function of kinetic energy per nucleon. The table states both statistical and systematic uncertainties.

This is shown in Figure 7.1. Statistical and systematic uncertainties are shown as thin and thick error bars respectively. The TRACER measurement covers an energy range from 1 GeV/amu to several TeV/amu and gives a detailed picture of the boron-to-carbon ratio above 30 GeV/amu. The ratio exceeds the 1 TeV/amu energy range.

Most of the systematic effects are correlated for boron and carbon, and thus cancel. The main source of systematic uncertainty remaining for this measurement is in the calculation of the amount of boron produced in the atmosphere above the instrument. It is of particular importance when the abundance of boron becomes very small as compared to the abundance

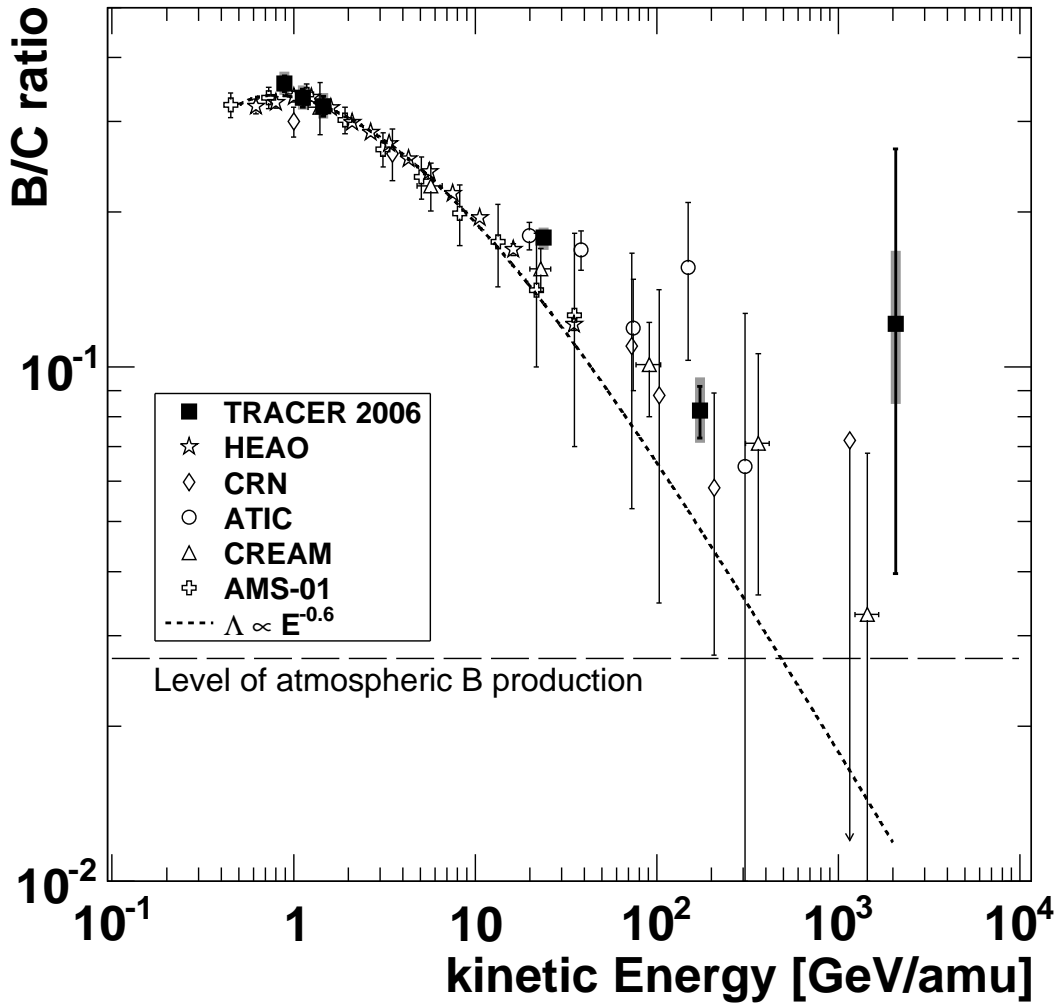


Figure 7.1: The boron-to-carbon abundance ratio as a function of kinetic energy per nucleon. Error bars are statistical (thin) and systematic (thick). A simple model with asymptotic proportionality of the escape pathlength to $E^{-0.6}$ (dotted) and the subtracted contribution of atmospheric production of boron (dashed) are indicated. Previous measurements are shown from HEAO [27], CRN [83], ATIC [66], CREAM [4] and AMS-01 [1].

of carbon. The uncertainty is $\sigma = \begin{smallmatrix} +0.007 \\ -0.004 \end{smallmatrix}$. Also, the uncertainty of the energy measurement does not entirely cancel due to the different spectral indices of the boron and carbon energy spectra. The systematic uncertainty in the highest energy data point is largely attributed to this uncertainty.

The statistical uncertainties are propagated using Poisson errors, $\sigma_N = \sqrt{N}$, so that the uncertainty on the ratio can be written a

$$\sigma_R = R \cdot \left(\frac{1}{\sigma_B^2} + \frac{1}{\sigma_C^2} \right)^{1/2}, \quad (7.2)$$

with σ_B and σ_C determined according to the number of boron and carbon events counted, respectively. This calculation is valid when the number of events counted is large compared to 1, and when the ratio is not close to zero.

Table 7.1: Summary of parameters used to derive the boron-to-carbon abundance ratio (B/C). The ratio is calculated at \hat{E}_B , see Eq. 6.4.

| Energy Range (GeV/amu) | Energy \hat{E}_B (GeV/amu) | Flux of B at \hat{E}_B ($\text{m}^2 \text{ s sr GeV/amu}$) ⁻¹ | Flux of C at \hat{E}_C ($\text{m}^2 \text{ s sr GeV/amu}$) ⁻¹ | B/C ratio $\pm \sigma_{stat} \pm \sigma_{sys}$ |
|---------------------------|---------------------------------|---|---|---|
| 0.8 - 1.0 | 0.9 | 1.1×10^0 | 3.2×10^0 | $(3.6 \pm 0.1 \pm_{0.17}^{0.19}) \times 10^{-1}$ |
| 1.0 - 1.3 | 1.1 | 7.3×10^{-1} | 2.2×10^0 | $(3.3 \pm 0.1 \pm_{0.17}^{0.19}) \times 10^{-1}$ |
| 1.3 - 1.7 | 1.5 | 3.8×10^{-1} | 1.2×10^0 | $(3.2 \pm 0.1 \pm_{0.17}^{0.19}) \times 10^{-1}$ |
| 9.5 - 86.5 | 23.8 | 4.9×10^{-4} | 2.3×10^{-3} | $(1.8 \pm 0.04 \pm_{0.09}^{0.08}) \times 10^{-1}$ |
| 86.5 - 432 | 173 | 1.6×10^{-6} | 1.7×10^{-5} | $(8.2 \pm 0.9 \pm_{1.1}^{1.3}) \times 10^{-2}$ |
| 1500 - | 2070 | 3.5×10^{-9} | 2.2×10^{-8} | $(1.2 \pm_{0.84}^{1.4} \pm_{0.4}^{0.5}) \times 10^{-1}$ |

For the data point at 2 TeV/amu (based on 10 carbon events and 1 boron event) a different approach, based on Bayes' Theorem, was used to determine the uncertainty.¹

The subtraction of carbon contamination and atmospheric contribution to the boron-to-carbon ratio are based on statistical arguments, which break down with just one event. Thus, some caution in the evaluation of the result is advisable.

As is evident from Figure 6.7 in Section 6.3.1, this one event could be unambiguously determined to be a boron nucleus. Still, this boron event has a 20% chance of being of atmospheric origin. If it is indeed of atmospheric origin, the data point should be regarded as an upper limit.

The dashed line in the figure indicates the estimated level of the boron-to-carbon ratio due to atmospheric production of boron, which has been subtracted. The value of the ratio at this dashed line indicates a systematic limit that balloon-borne experiments can achieve, as the atmospheric contribution becomes larger than the cosmic-ray contribution. The energy at which this limit is encountered, however, depends on the shape of the ratio. A possible solution to this limitation is to conduct a measurement in space with no residual atmosphere.

In Fig. 7.1, previous measurements from HEAO [27], CRN [83], ATIC [66], CREAM [4] and AMS-01 [1] are shown in comparison to this work's result. The data agree well where uncertainties are small enough to facilitate such a comparison. At high energies, the data agree within the large statistical uncertainties. At low energies, slight differences between measurements may be expected due to solar modulation, which is rigidity dependent, and therefore its effect does not entirely cancel in the ratio of boron to carbon.

This measurement features better statistical accuracy than previous balloon-borne measurements from ATIC and CREAM. It greatly exceeds the statistical accuracy of the space-borne

¹The calculation of the uncertainty follows the prescription given by M. Paterno [67], evaluating the probability distribution of the ratio $r = k/n$. The counted variables k and n are taken from a binomial distribution. The necessary assumption on the ratio prior to the Bayesian analysis is that the ratio is less than 1 and not smaller than 0. Then the probability distribution of the ratio r as a function of k and n can be found. The most probable ratio is always $r = k/n$. The 1σ uncertainty range is defined as the smallest interval around r which contains 68% of all possible ratios. The method requires complicated numerical integrations, which are implemented in the ROOT data analysis framework [19]. The resulting statistical uncertainty is $\sigma = \begin{smallmatrix} +120\% \\ -70\% \end{smallmatrix}$.

experiments CRN, HEAO, and AMS-01 at high energies.

The dotted line in Fig. 7.1 represents a parametrization of the escape pathlength for the propagation of cosmic rays in the Galaxy based on the data from ACE/CRIS [95] and HEAO [27] below 10 GeV/amu. The escape pathlength $\Lambda(R)$ is thereby assumed to be a function of rigidity R [95]:

$$\Lambda(R) = \frac{26.7\beta}{(\beta R)^{0.58} + (0.714 \cdot \beta R)^{-1.4}} \text{ g/cm}^2, \quad (7.3)$$

with the particle velocity β and rigidity R . For highly relativistic particles the rigidity is proportional to the particle's energy and it is defined as:

$$R = \frac{pc}{Ze} \left(= \frac{E}{Ze} \text{ for } \gamma \gg 1 \right), \quad (7.4)$$

with the particle's momentum p , charge Ze , and the speed of light c . The proportionality to the kinetic energy per nucleon is valid for $\gamma \gg 1$. Thus, at high energy Eq. 7.3 is proportional to $E^{-0.58}$, and no asymptotic saturation is assumed.

Above 10 GeV/amu, this work's result and previous measurements lie consistently above the values predicted by this model. Even though the uncertainties are large, it is useful to consider alternative models to interpret the data. They are discussed in the following section.

7.2 Discussion of the Result

As outlined in Section 1.3, the boron-to-carbon ratio is a measure for the escape pathlength, Λ_{esc} , of cosmic rays from the Galaxy. The propagation model, described in the same section, predicts a power-law dependence of the escape pathlength on energy. Previous measurements, at energies below 10 GeV/amu, have suggested a propagation index δ of about 0.6 (see Eq. 7.3). The propagation model and predictions based on previous measurements are discussed in the following section in the light of the new measurement of this work.

In practice, simplifications of the propagation model have to be assumed for the interpretation of experimental data, leading to a "Leaky-Box" model, or extensive numerical simulations have to be employed. The next sections cover both approaches.

7.2.1 A Leaky-Box Model with Residual Pathlength

In the Leaky-Box approximation of Galactic propagation of cosmic rays the differential intensity N_i of a elemental species is given as Eq. (1.9):

$$N_i = \frac{1}{\Lambda_{\text{esc}}^{-1} + \Lambda_s^{-1}} \cdot \left[\frac{Q_i}{\beta\rho c} + \sum_{k>i} \frac{N_k}{\Lambda_{k \rightarrow i}} \right], \quad (7.5)$$

where Λ_{esc} is the escape pathlength, Λ_s is the spallation pathlength of element i , Q_i is its source term, $\beta\rho c$ is the matter traversed, and $\Lambda_{k \rightarrow i}$ is the production length of species i from a heavier species k .

For boron, the source term is not applicable and therefore vanishes. The production of boron through spallation is primarily due to carbon and oxygen. This leads to:

$$N_B = \frac{1}{\Lambda_{\text{esc}}^{-1} + \Lambda_s^{-1}} \cdot \left[\frac{N_C}{\Lambda_{C \rightarrow B}} + \frac{N_O}{\Lambda_{O \rightarrow B}} \right]. \quad (7.6)$$

Dividing by the carbon intensity, N_C , an expression for the boron-to-carbon abundance ratio (B/C), in terms of the Leaky-Box approximation, is arrived at:

$$\left(\frac{B}{C} \right) = \frac{N_B}{N_C} = \frac{\Lambda_{\rightarrow B}^{-1}}{\Lambda_{\text{esc}}^{-1} + \Lambda_s^{-1}}. \quad (7.7)$$

Here, the production pathlength for boron is $\Lambda_{\rightarrow B}^{-1} = \Lambda_{C \rightarrow B}^{-1} + \Lambda_{O \rightarrow B}^{-1}$, assuming the abundances of carbon and oxygen are equal and energy independent as can be seen from Table 6.3 or in [5, 83]. For interstellar matter (90% H, 10% He), the numerical value is $\Lambda_{\rightarrow B} = 26.8 \text{ g/cm}^2$. The spallation pathlength for boron Λ_s in the interstellar medium is 9.3 g/cm^2 . These values have been evaluated with the cross sections reported by Webber et al. [90, 91].

The escape pathlength is assumed to follow the parametrization given in Eq. (7.3) with an asymptotic behavior as a function of energy like:

$$\Lambda_{\text{esc}}(E) = C \cdot E^{-\delta} + \Lambda_0, \quad (7.8)$$

with the power-law index of the escape pathlength δ and the residual pathlength Λ_0 (see also Section 1.3). The parametrization of Λ_{esc} used to fit the experimental data is thus:

$$\Lambda(R) = \frac{26.7\beta}{(\beta R)^\delta + (0.714 \cdot \beta R)^{-1.4}} + \Lambda_0 \text{ g/cm}^2, \quad (7.9)$$

Cosmic-ray Propagation and the TRACER Measurement

Previous measurements at energies below 10 GeV/amu suggest a pathlength index δ of about 0.6 with no residual pathlength (Eq. (7.3)). The resulting parametrization of the boron-to-carbon ratio is shown as the dotted line in Figure 7.2.

A fit to the TRACER data was conducted for Λ_0 assuming $\delta = 0.6$. The result is a value of $\Lambda_0 = 0.77 \pm 0.32 \text{ g/cm}^2$ for the residual pathlength. This result is illustrated as the dashed line in Fig. 7.2, indicating the good agreement of the model with the data.

However, no a-priori assumption regarding the power-law index of the escape pathlength $\delta = 0.6$ has to be made. Treating δ and Λ_0 as free parameters in the fit, a χ^2 map is produced as shown in Figure 7.3. It can be seen that δ is well constrained and close to the originally assumed value of 0.6, but that Λ_0 is not well constrained. The range Λ_0 is very wide, as it is only sensitive to high-energy data. The resulting most probable values are $\delta = 0.53 \pm 0.06$ and $\Lambda_0 = 0.31 \pm_{0.31}^{0.55} \text{ g/cm}^2$. They are indicated as solid line in Fig. 7.2.

The central value for Λ_0 is consistent with that reported previously by the TRACER group on the basis of an independent analysis of the measured energy spectra of the primary elements (Chapter 3, [13]).

A propagation index of 1/3, corresponding to a Kolmogorov spectrum of magnetic irregularities in the Galaxy (see Section 1.3), is strongly disfavored within the framework of the Leaky-Box approximation.

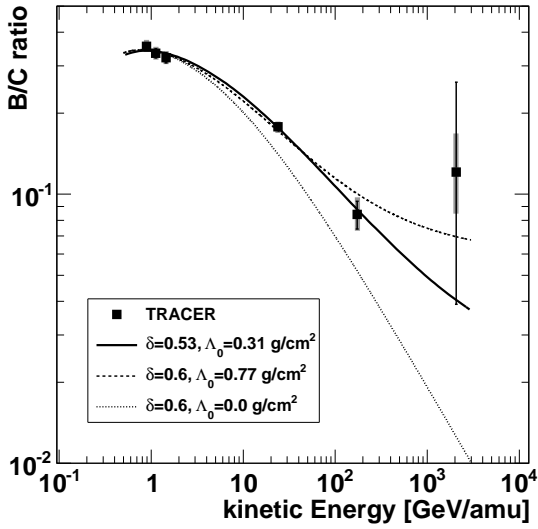


Figure 7.2: The boron-to-carbon measurement as a function of energy made by the TRACER experiment. The dashed and dotted lines represent possible outcomes of the Leaky-Box model with δ set to 0.6 and a residual pathlength of 0.77 and 0.0 g/cm^2 , respectively. The solid line represents the overall best fit with $\delta = 0.53$ and $\Lambda_0 = 0.31 \text{ g}/\text{cm}^2$.

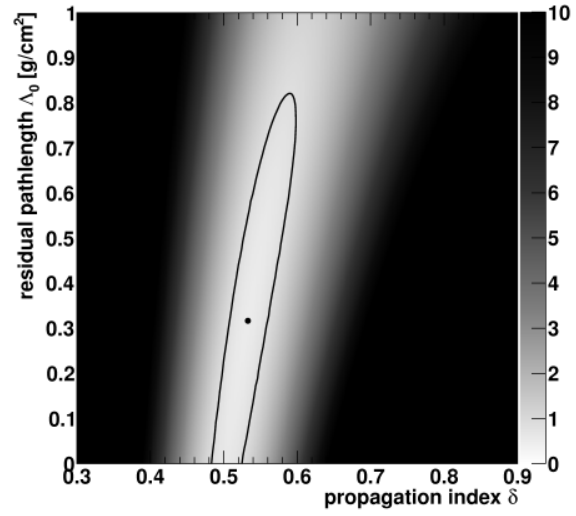


Figure 7.3: χ^2 map in the parameter space of δ vs. Λ_0 . The best fit values are marked at $(\delta, \Lambda_0) = (0.53, 0.31 \text{ g}/\text{cm}^2)$ and the 1σ contour is indicated.

The large uncertainty of the best fit value of Λ_0 is due to the large statistical uncertainty of the measurement at high energies. However, the most probable value found for the residual pathlength is non-zero, which implies that the escape pathlength may not become arbitrarily small at high energies. An arbitrarily small escape pathlength would imply that a cosmic-ray particle travels a very short distance to the Earth. This would lead to anisotropies in the cosmic-ray flux that have not been observed [68]. It should be noted that the IceCube collaboration recently reported anisotropies in the cosmic-ray flux of about 20 TeV at the angular scale of 10° to 30° [84]. While this could be an indication of a nearby cosmic-ray source or a very small escape pathlength, a conclusive interpretation is not possible.

The fit result for the boron-to-carbon ratio can be used to determine an absolute parametrization of the escape pathlength. The absolute escape pathlength is shown in Figure 7.4 as parametrized in Eq. 7.9 with $\delta = 0.53 \pm 0.06$ and $\Lambda_0 = 0.31 \pm_{0.31}^{0.55} \text{ g}/\text{cm}^2$ found with the TRACER data. The uncertainty range is indicated with dashed lines. The average column density a primary cosmic ray traverses is determined to be about $4.4 \text{ g}/\text{cm}^2$ at 20 GeV/amu and about $1.7 \text{ g}/\text{cm}^2$ at 200 GeV/amu.

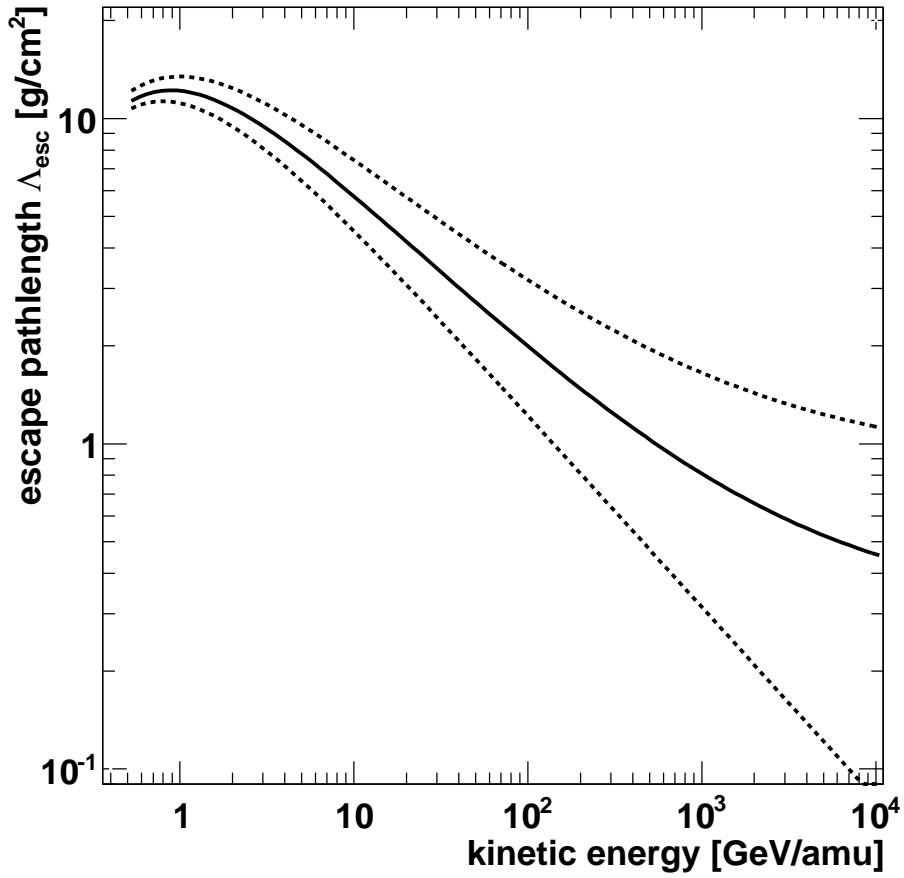


Figure 7.4: The escape pathlength Λ_{esc} as derived from the TRACER measurement with $\delta = 0.53 \pm 0.06$ and $\Lambda_0 = 0.31 \pm_{0.31}^{0.55} \text{ g/cm}^2$. The escape pathlength is defined in Eq. 7.9. The dashed lines illustrate the 1σ uncertainty range for the escape pathlength.

Combining all Available Data

The same Leaky-Box propagation model is also fit to all previous measurements including the results presented here. The data and fitted curves are shown in Figure 7.5. However, because not all authors define the uncertainties of their data consistently, there might be a bias in this fit.

Using the same power-law index that fits the low-energy data, $\delta = 0.6$, a value for the residual pathlength Λ_0 is found to be $\Lambda_0 = 0.38 \pm_{0.37}^{0.54} \text{ g/cm}^2$ (dashed line in Fig. 7.5). The large uncertainty reflects not only the large statistical uncertainties of all measurements at high energies, but also the considerable spread of the data points. Still, a non-zero residual pathlength is again favored. This result is consistent, within the uncertainties, with the results presented above from the TRACER instrument.

Allowing δ to vary as a free parameter, the combined fit to all data yields $\delta = 0.64 \pm 0.02$ and $\Lambda_0 = 0.7 \pm 0.2 \text{ g/cm}^2$, and is represented as the solid line in Figure 7.5. The χ^2 contour map for this fit to all data is shown in Fig. 7.6. The best fit values are marked and a 1σ contour is shown.

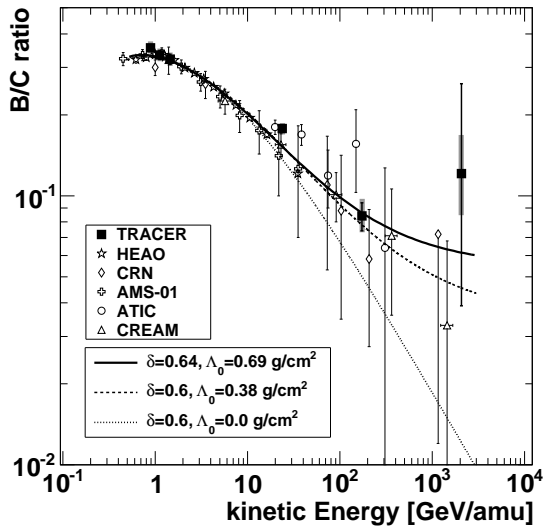


Figure 7.5: The abundance ratio of boron and carbon from TRACER (this work), space-born experiments HEAO [27], CRN [83] and AMS-01 [1], and balloon-borne experiments ATIC [66], CREAM [4]. For the dashed and dotted lines δ is set to 0.6 and the residual pathlength is 0.38 and 0.0 g/cm^2 , respectively. The solid line represents the overall best fit with $\delta = 0.64$ and $\Lambda_0 = 0.69 \text{ g/cm}^2$.

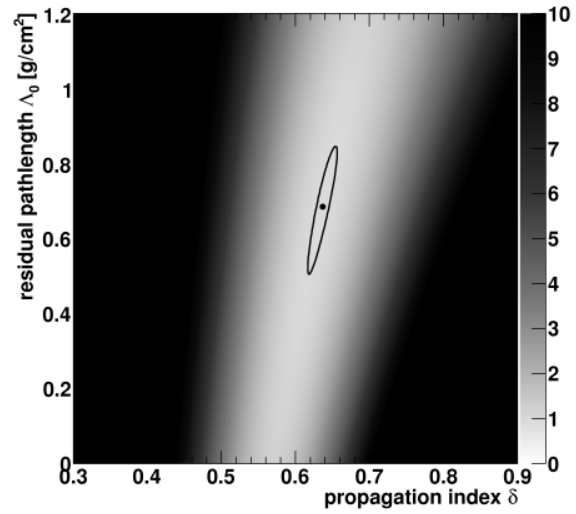


Figure 7.6: χ^2 map in the parameter space of δ vs. Λ_0 for the model fit to all data (according to Eq. 7.9 see Fig. 7.5 for references). The best fit values are marked at $(\delta, \Lambda_0) = (0.64, 0.69 \text{ g/cm}^2)$ and the 1σ contour is indicated.

Again, the power-law index for the propagation of cosmic rays is better constrained than the residual pathlength. The combined data favor slightly larger values for δ than the TRACER data alone, but are not inconsistent. A large range of possible values for Λ_0 between 0.5 and 1.0 g/cm^2 is evident and is commensurate with the range found for Λ_0 with only TRACER data.

7.2.2 The Effect of a Leaky-Box Model on Cosmic-Ray Spectra

It is commonly assumed that energy spectra produced at the sources of cosmic rays are power laws. This is consistent with first-order Fermi acceleration, however deviations from pure power-law behavior may be expected in more realistic scenarios. [7].

The CREAM experiment has recently published in [6] what they call a “discrepant” hardening in their observed primary cosmic-ray spectra for elements from carbon to iron above 200 GeV/amu . The authors discuss constraints to acceleration models that the spectral hardening poses. However, before one can make a statement about effects at the source one also needs to consider deformations of the cosmic-ray spectra that may occur during propagation through the Galaxy.

In the Leaky-Box model, the relation between energy spectra at the source and at the Earth

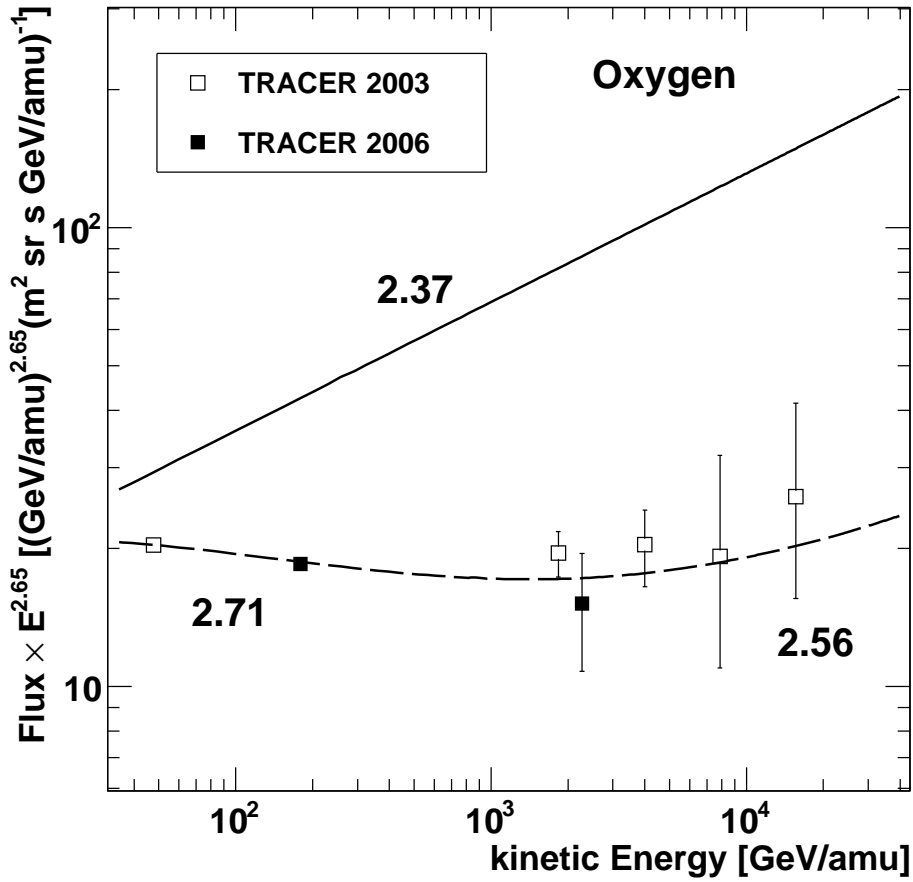


Figure 7.7: Energy spectrum of oxygen as measured by TRACER in its two flights. A source spectrum is fit to the data according to Eq. (7.10). The resulting source spectrum with index $\alpha = 2.37$ is shown as a solid line. The corresponding, modified spectrum that is observed at the Earth is shown as a dashed line. The respective spectral indices are stated. The normalization of the source spectrum is arbitrary.

can be expressed as:

$$\left(\frac{dN_i}{dE}\right)_{\text{Earth}} \propto E^{-\alpha} \cdot \frac{1}{\Lambda_{esc}^{-1} + \Lambda_i^{-1}}, \quad (7.10)$$

with the spallation pathlength in interstellar matter for the investigated element Λ_i and the escape pathlength Λ_{esc} . This equation follows from Eq. (7.5) if one neglects the production of element i by spallation of heavier elements in the interstellar material. It is evident from Equation 7.10 that the smaller pathlength has the dominant effect on the observed spectrum. At high energies the dominant (i. e. smaller) pathlength is the escape pathlength compared to the spallation pathlength, even for iron.

Also, Equation 7.10 assumes that the source spectrum is a straight power law with index α . The source spectral index α is a key parameter to characterize cosmic-ray sources. Simple acceleration models at strong shocks predict α to be close to 2.0 [15]; whereas more complicated approaches can result in indices of about 2.3 or 2.4 [46]. In the following, the source index α is estimated in the light of the TRACER measurements and the results on the propagation of cosmic rays in the Galaxy.

Figure 7.7 illustrates these effects of propagation on the oxygen energy spectrum. The energy spectrum of oxygen is fit to the data of both TRACER measurements according to Eq. 7.10. The escape pathlength found with the (B/C) ratio from TRACER measurements only with $(\delta, \Lambda_0) = (0.53 \pm 0.06, 0.31 \pm_{0.31}^{0.55} \text{ g/cm}^2)$ is used together with the spallation pathlength corresponding to cross sections given by Webber et al. [91]. Free parameters are a normalization factor and the source spectral index α .

For oxygen, the data are fit best between 30 and about 15,000 GeV/amu in kinetic energy with a source index of $\alpha = 2.37 \pm 0.12$. The observed spectrum then has an average spectral index of about 2.65, as also reported previously by TRACER [12]. Since the escape pathlength is not a power law, the spectrum at Earth is therefore not a strict power law. The observed spectral index changes from 2.71 at low energies, to 2.56 above several hundred GeV/amu. This could be interpreted as a spectral hardening. However, even if a hardening is present in the cosmic-ray energy spectra, it could not yet be significantly detectable within the accuracy of the present data. It should be noted, that a hardening due to propagation effects affects energy spectra of different elements to a different degree; whereas a source effect might affect all elemental spectra in the same way.

It is also evident that the resulting spectral index of the observed spectrum at the Earth is not the sum of source index α and propagation index δ , but smaller. This is caused by the additive parameters, the residual pathlength Λ_0 and the spallation pathlength Λ_{sp} .

7.2.3 Comparison of the Data with GALPROP

As a further check on our conclusions we have also tested our results with predictions of the GALPROP model. The GALPROP computer simulation (GALactic PROPagation, [78]) numerically models the propagation of Galactic cosmic rays. This simulation has had much success in providing a consistent model of many aspects of Galactic cosmic radiation, e. g. the proton to anti-proton ratio, secondary-to-primary abundance ratios, electron spectrum, positron fraction, and γ -ray background. A review of GALPROP is available in [80].

GALPROP is available as a webrun interface [86] to determine many parameters of Galactic cosmic rays, including the boron-to-carbon ratio. The user can choose input parameters or use the default parameters that have been optimized to best describe all available data on Galactic cosmic rays.

GALPROP calculates cosmic-ray fluxes in a two-dimensional model of the Galaxy. Here, a scale height of $L = 4$ kpc is chosen, motivated by observations of radioactive nuclei [79]. The diffusion coefficient characteristic for cosmic-ray propagation is assumed to be a function of magnetic rigidity R :

$$D = \beta D_0 R^\delta, \quad (7.11)$$

with the particle velocity $\beta = v/c$, a proportionality factor D_0 , and the propagation index δ . This index is essentially the same index as found in the previous section in the Leaky-Box approximation for a one dimensional flat halo model [70], but its meaning for cosmic-ray transport can change when transferring it to multi-dimensional numerical models. GALPROP does not invoke any asymptotic value for the diffusion coefficient, so there is no equivalent to

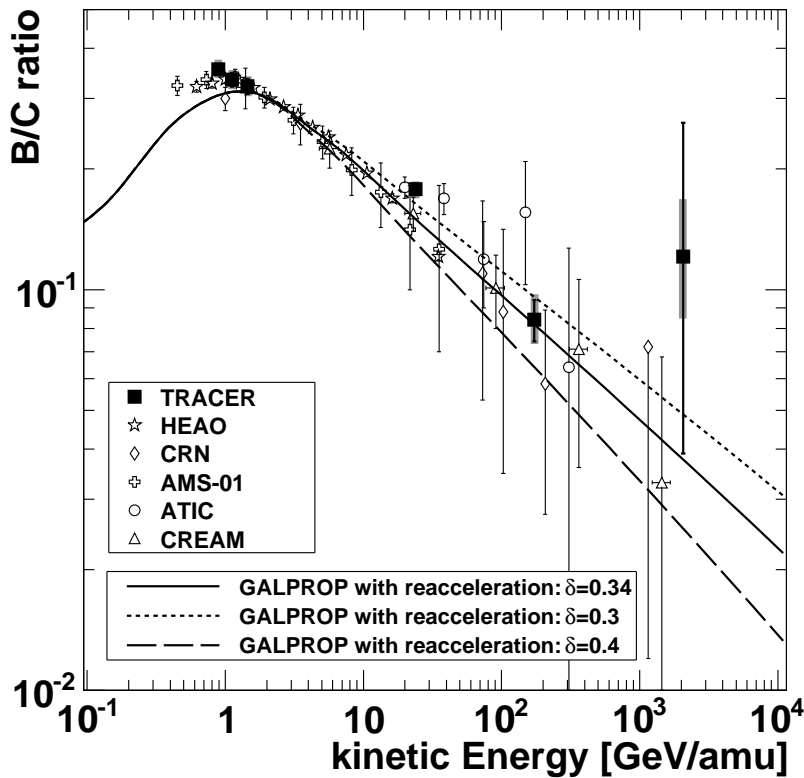


Figure 7.8: Illustration of GALPROP models. Best model describing all available cosmic-ray data with $\delta = 0.34$ (solid). Models with different values of δ are represented with dashed lines.

the residual pathlength Λ_0 that was estimated earlier.

Other key input parameters are measured interaction cross sections and values thereof given by Webber et al. [91] when no experimental data are available. The source abundances are tuned to fit ACE/CRIS observations [24]. A spectral index of 2.34 at the source is assumed for all elements, as suggested by the GALPROP group as the preferred value to describe all available cosmic-ray observations.

GALPROP can include convection and reacceleration of cosmic rays in its calculations. Convection in the Galactic wind, however, is not established as a probable effect cosmic rays are exposed to and is neglected here. Reacceleration is a distributed acceleration at moving magnetic fields, described by second-order Fermi acceleration. It is taken into account here as suggested by the standard GALPROP model.²

In contrast to GALPROP, the diffusion coefficient in the Leaky-Box approximation is not proportional to β but only $D_0 R^\delta$, which can lead to differences in interpretation at low energies. Also, the boundaries of the propagation volume are fully transparent to cosmic rays in the numerical model, but have a finite escape probability in the Leaky-Box model. Another difference between numerical models and the Leaky-Box model is that reacceleration is not taken into account in the latter.

For the calculation of the model prediction for the boron-to-carbon ratio GALPROP was

²An Alfvén speed of 36 km/s of the magnetic fields is used.

used with the input parameters as detailed before. Three cases were investigated: (1) the best fit model to all cosmic-ray data with reacceleration and diffusion index δ set to 0.34; (2) with $\delta = 0.3$; and (3) with $\delta = 0.4$. Thus, model (1) represents the standard GALPROP model that fits all observed data best.

Figure 7.8 shows the comparison of the boron-to-carbon ratio from the GALPROP simulation and from the TRACER measurement. Also, previous measurements are shown for comparison. The GALPROP curves are independently calculated and do not use the data in any form for normalization. The discrepancy between model and data at low energies may be due to the effect of solar modulation. It is also present in a recent review of the GALPROP group [80]. However, this discrepancy at low energies is of no primary interest in the present study.

The best agreement of the TRACER data and the GALPROP model is evident for input parameters of source spectral index $\alpha = 2.34$, propagation index $\delta = 0.34$, and including reacceleration. The data are compatible with a range for δ between 0.3 and 0.4, as illustrated in Fig. 7.8. This result for δ is consistent with $\delta = 1/3$, corresponding to Kolmogorov turbulence of magnetic fields.

The input spectral index of the source, $\alpha = 2.34$, agrees with the earlier findings of TRACER from primary cosmic-ray spectra (see Chapter 3 or [13]). It is also in agreement with the results of this work using the observed oxygen spectrum and the propagation parameters inferred from the measured boron-to-carbon ratio.

7.2.4 Synopsis of the Results

Estimated Propagation Parameters Both models, the Leaky-Box model and GALPROP, describe the measured data well. The decrease of the boron-to-carbon ratio with energy is described in the Leaky-Box model as a spectral index modified at high energies by an asymptotic limit. Within GALPROP, it is described as a slower decrease that is steepened at low energies by reacceleration. This is a principal difference of the models and illustrates that δ cannot be interpreted as the same physical quantity in both models.

Within the framework of a Leaky-Box model the propagation index δ and the residual pathlength Λ_0 (see Eq (7.8)) were estimated with TRACER data alone to $\delta = 0.53 \pm 0.06$ and $\Lambda_0 = 0.31 \pm_{0.31}^{0.55} \text{ g/cm}^2$, respectively. Using Equation (7.9), this suggests that a cosmic-ray nucleus at 200 GeV/amu traverses about 1.7 g/cm^2 of column density before it escapes the Galaxy. Fitting the Leaky-Box model simultaneously to all data the values become $\delta = 0.64 \pm 0.02$ and $\Lambda_0 = 0.7 \pm 0.2 \text{ g/cm}^2$. These slightly larger values are consistent with the values found with TRACER data alone.

With the numerical simulation of Galactic propagation of cosmic rays, GALPROP, the propagation index was commensurate with all experimental data for values between $\delta = 0.3$ and 0.4. GALPROP [78] does not include any asymptotic lower limit for the escape pathlength Λ_{esc} , so the question remains in this model if Λ_{esc} can become zero.

Hardening of the Measured Primary Cosmic-Ray Spectra A non-zero value for the residual pathlength Λ_0 can change the shape of the observed cosmic-ray spectra of primary elements.

This would appear as a "hardening" of the observed spectra at a few hundred GeV/amu. Such a hardening, predicted by the Leaky-Box model, is not predicted by the current GALPROP model that assumes no asymptotic value for the diffusion coefficient. In order to unambiguously decide if such an asymptotic value exists measurements of secondary-to-primary cosmic-ray abundance ratios are needed at higher energies than currently available.

The Spectral Index at the Source Both propagation models, the Leaky-Box approximation and GALPROP, do agree in one key result. They both suggest a source spectral index α of about 2.3 to 2.4. A very similar result was previously reported by TRACER from the measurement of primary cosmic-ray spectra [13].

This experimentally deduced source index stands in contrast to a value of about 2.0 suggested by first-order Fermi acceleration of cosmic rays at strong shocks. Some modifications to currently accepted acceleration models may be needed to accommodate a soft source spectrum with $\alpha \approx 2.3$.

A complementary estimation of the source index is desirable, for example from very high-energy γ -ray astronomy. The source spectrum of hadronic cosmic rays is imprinted in γ -ray emission at about 10 times smaller energy (e. g. [41]).

Several supernova remnants have now been observed, but it is difficult to compare the spectral indices found in a conclusive way. As an example, the estimated spectral index for the supernova remnant RX J1713 [2] is 1.98 ± 0.05 at an energy of about 500 GeV/amu [3]. The questions remain if the emission is truly of hadronic origin, and if RX J1713 is a "typical" cosmic-ray source.

A rigorous study of this comparison is an interesting prospect for the future, but is beyond the scope of this thesis.

CHAPTER 8

CONCLUDING SUMMARY

TRACER is a balloon-borne detector that measures the individual energy spectra of cosmic radiation from boron ($Z = 5$) to iron ($Z = 26$). In this work, the results of the TRACER project are presented with emphasis on the measurement of the boron-to-carbon abundance ratio.

TRACER is currently the largest balloon-borne cosmic-ray detector and has had two successful long-duration balloon flights. The results presented here are based on the data recorded in 2006 in the flight from Sweden to Canada. This flight lasted for 4.5 days, and had to be terminated early due to the lack of permission to fly over the Russian territory.

The instrument performed well during the flight without deterioration of the gas in the proportional tube system. It was successfully recovered and currently resides at the University of Chicago. Post-flight testing indicated that the instrument is in remarkably good condition and could be refurbished for another flight.

The data analysis of the 2006 flight is now complete. The analysis begins with determining the trajectories of the particles through the instrument. Next the nuclear charge is determined for each particle using a correlation of scintillation and Čerenkov detectors. The charge resolution is 0.23 charge units for boron and carbon, rising to 0.55 charge units for iron.

The measurement of the TRACER instrument covers a large range in energy from about 800 MeV/amu to several TeV/amu. This is achieved by combining the responses of three sub-detectors; the Čerenkov detector below 3 GeV/amu, the dE/dX-array between 10 and 500 GeV/amu, and the TRD above 700 GeV/amu. The energy resolution of each detector is determined as a function of charge. The energy spectra are constructed taking care of bin correlations that are present for steeply falling spectra.

The differential intensities of cosmic-ray elements iron, oxygen, carbon and boron at the top of the atmosphere are presented here. Good agreement exists between this data set and previous measurements. The determination of the absolute boron energy spectrum includes, for the first time, a measurement of this nucleus above 1 TeV/amu. The highest-energy boron event is found at 6 TeV/amu. Special care is taken to avoid a bias to the boron energy spectrum, and thus the boron-to-carbon ratio, due to carbon events contaminating the boron sample.

The rate of production of boron in the residual atmosphere above the detector must be subtracted appropriately from the measured fluxes. It can be calculated using particle-particle

cross sections. However, the systematic uncertainty of the calculation is considerably large. Therefore, a method was developed, using the TRACER data, to determine the rate of production as a function of atmospheric overburden. The results of this method are compatible, within uncertainties, to the calculation, and are promising for future balloon missions with improved statistics.

A new measurement of the important boron-to-carbon ratio is presented. The ratio is consistent with previous measurements at low energies and represents a detailed measurement above 30 GeV/amu. The measurement extends to 2 TeV/amu, with 10 carbon events and 1 boron event at the highest energy interval.

The abundance ratio of boron-to-carbon is compared to two models of Galactic cosmic-ray propagation, the Leaky-Box model and GALPROP. For the Leaky-Box model the propagation index δ and the residual pathlength Λ_0 are evaluated to $(\delta, \Lambda_0) = (0.53 \pm 0.06, 0.31 \pm_{0.31}^{0.55} \text{ g/cm}^2)$ from the TRACER measurement. As a result it can be inferred that a primary cosmic ray of 200 GeV/amu energy traverses about 1.7 g/cm² of interstellar matter. Also, a non-zero residual pathlength causes a hardening in the observed energy spectra above several 100 GeV/amu. This emphasizes the importance to understand cosmic-ray propagation before source properties are inferred from the observed energy spectra.

The best GALPROP model to describe the measured data includes reacceleration and a high-energy diffusion coefficient proportional to $E^{-0.34}$, with a possible range in the index from 0.3 to 0.4. This is a significantly smaller propagation index than what is found using the Leaky-Box model. However, the propagation index δ has different meaning in the models. It is modulated in the Leaky-Box model by the residual pathlength. In the GALPROP model it requires a significant amount of reacceleration at low energies to match the observed data.

Both models, however, agree on the source spectral index to be rather soft: $\alpha = 2.3$ to 2.4. The source spectral index to fit the observed data best within the Leaky-Box framework is $\alpha = 2.37 \pm 0.12$ for oxygen. The input value of the source index in the preferred GALPROP model is $\alpha = 2.34$. These values are in excellent agreement with the value deduced from the previous TRACER measurement of spectra of primary cosmic-ray elements. The derived source spectra are softer than expected from first-order Fermi acceleration at strong shocks ($\alpha \approx 2.0$).

In conclusion, the measurements conducted with the TRACER detector contributed significantly to the current understanding of cosmic radiation at high energy. The detector has demonstrated its capability to access the highest energies with a direct measurement at the top of the atmosphere. It has been shown that a transition radiation detector is currently the most promising approach to measure cosmic-ray nuclei heavier than lithium up to energies around a hundred TeV/amu.

It has to be mentioned, that finding a handful of high-energy particles out of the overwhelmingly numerous low-energy background is very challenging. The TRACER concept has proven that it is capable to excel at the task, its limitations are well understood and can be reduced, and the TRACER detector can be fully refurbished for a future flight.

DEUTSCHE ZUSAMMENFASSUNG

Als Kosmische Strahlung bezeichnet man Atomkerne und Elektronen, die aus dem Weltraum in die Atmosphäre der Erde eindringen. Die Teilchen sind zum Großteil galaktischen Ursprungs und werden an Schockfronten, wie sie z. B. nach Supernovas entstehen, beschleunigt.

Bevor sie auf die Erde treffen, breiten sie sich diffus für etwa 15 Millionen Jahre durch die Galaxie aus, von der sie auch entweichen oder mit interstellarer Materie in Wechselwirkung treten können. So wird das beobachtete Energiespektrum Kosmischer Strahlung an der Erde nicht nur durch Eigenschaften der Quellen, sondern auch von der Art und Weise ihrer Ausbreitung durch die Galaxie bestimmt.

Ein Aspekt dieser Ausbreitung ist das Verlassen der Galaxie. Dies kann durch die Messung vom Verhältnis sekundärer zu primärer Kosmischer Strahlung, z. B. Bor zu Kohlenstoff, bestimmt werden. Bor kommt nicht in den Quellen Kosmischer Strahlung vor. Durch Kohlenstoff wird dagegen Bor auf dem Weg durch interstellare Materie bei atomaren Kollisionen produziert. Ist die Wegstrecke (d. h. die Massenbelegung), die Kohlenstoff hinter sich bringt, bevor es aus der Galaxie austritt, lang, so wird viel Bor produziert; ist sie kurz, wird wenig Bor produziert. So ist das Verhältnis von Bor zu Kohlenstoff ein Maß für die durchquerte Materie bevor Kosmische Strahlung aus der Milchstraße austritt.

An der Erde angekommen kann galaktische Kosmische Strahlung mit einer Energie von weniger als 10^{15} eV (Elektronenvolt, $1 \text{ eV} = 1,6 \cdot 10^{-19}$ Joule) direkt gemessen werden. Dazu werden Teilchendetektoren, die Ladung und Energie der Teilchen messen, entweder in den Weltraum gebracht oder mit Ballons an den oberen Rand der Atmosphäre gehoben. Aus beiden Methoden ergeben sich gravierende Einschränkungen für die experimentelle Technik in Bezug auf Gewicht, Größe, Stromverbrauch und Messzeit.

Der zur Zeit größte von einem Ballon getragene Detektor ist TRACER mit einer geometrischen Apertur von $5 \text{ m}^2 \text{ sr}$. Der Detektor wurde an der Universität von Chicago gebaut. Es werden nur elektromagnetische Prozesse genutzt, um Ladung und Energie der Kerne zu bestimmen, die den Detektor durchqueren.

Die Ladungszahl wird durch eine Kombination von Szintillator- und Čerenkov-Detektoren am oberen und unteren Ende des Instrumentes gemessen. Dies ist auch notwendig, um Ereignisse herauszufiltern, die im Detektor wechselwirken. Die Energiemessung findet in drei unabhängigen Bereichen statt: Um 1 GeV/amu mit dem unteren Čerenkov Detektor, zwischen 10 und 500 GeV/amu mit dem Signal des "dE/dX-array" (gemessen durch den flachen Anstieg des Signals im Bereich der relativistischen Zunahme spezifischer Ionisation in Gas) und oberhalb von 700 GeV/amu mit dem Übergangsstrahlungsdetektor (gemessen durch die

zur spezifischen Ionisation zusätzlichen Übergangsstrahlung).

Der TRACER Detektor wurde bei drei Ballonflügen eingesetzt. Zunächst wurde 1999 ein Testflug durchgeführt. Es folgten zwei Langzeitballonflüge: 2003 in der Antarktis und 2006 von Schweden nach Kanada. Der zweite Langzeitballonflug musste leider nach 4,5 Tagen abgebrochen werden, da keine Genehmigung für einen Flug über russisches Territorium zu erreichen war. Der TRACER Detektor wurde nach seinem letzten Flug wieder an die Universität von Chicago gebracht. Er ist grundsätzlich intakt und kann für einen weiteren Flug präpariert werden.

Im zweiten Langzeitballonflug konnten die Elemente von Bor bis Eisen ($Z = 5$ bis 26) gemessen werden. Die Daten dieses Flugs bilden die Grundlage der vorliegenden Doktorarbeit.

Der Schwerpunkt der Messung liegt auf dem Verhältnis von Bor zu Kohlenstoff, um die Ausbreitung Kosmischer Strahlung durch die Galaxie zu untersuchen. In dieser Arbeit wurde der Zustand des Detektors nach dem Flug getestet, die Datenauswertung durchgeführt und schließlich die Messung im Rahmen von Modellen zur galaktischen Ausbreitung Kosmischer Strahlung interpretiert.

Die Datenanalyse beginnt mit der Bestimmung und Anwendung verschiedener Korrekturen, die aus den gemessenen Daten selbst bestimmt wurden. Anschließend wurden die Flugbahnen der aufgezeichneten Teilchen rekonstruiert. Danach war es möglich die Ladung und Energie der Ereignisse zu bestimmen.

Das Resultat dieser Arbeit sind die Energiespektren von Bor, Kohlenstoff, Sauerstoff und Eisen. Sie reichen bis 2 TeV/amu in Energie. Für alle Elemente kann eine Übereinstimmung mit vorhergehenden Experimenten berichtet werden. Das Spektrum von Bor erweitert frühere Messungen signifikant zu höheren Energien. Dabei hat TRACER den bisher höchst-energetischen Bor Atomkern mit 6000 GeV/amu nachgewiesen.

Aus den Spektren von Kohlenstoff und Bor konnte deren Häufigkeitsverhältnis als Funktion der Energie bestimmt werden. Dabei wurde speziell darauf geachtet, dass mögliche systematische Messfehler durch Kohlenstoff-Kontamination oder atmosphärische Produktion von Bor vermieden wurden. Hierzu wurde eine Methode entwickelt, um die atmosphärische Produktion von Bor aus den Messdaten selbst abzuschätzen. Obwohl diese Methode mit den derzeitigen Daten lediglich dazu dienen kann die errechnete Produktionsrate zu überprüfen, ist sie im Hinblick auf zukünftige Experimente interessant.

Das gemessene Verhältnis von Bor zu Kohlenstoff erreicht 2 TeV/amu und übertrifft die früheren Messungen von HEAO, CRN, ATIC und AMS-01 bei hohen Energien an statistischer Genauigkeit. Die Teilchenzahl-Statistik ist vergleichbar mit der des CREAM Experimentes, das allerdings eine fast zehnmal längere Messzeit aufweist. Dies zeigt die überragenden Möglichkeiten des TRACER Konzepts auf, speziell auch für zukünftige Projekte.

Wie bereits ausgeführt folgt das Verhältnis von Bor zu Kohlenstoff der mittleren Massenbelegung, die Kosmische Strahlung auf dem Weg durch die Galaxie durchquert, bevor sie entweichen kann. Dies ist eine Funktion der Energie, ein Potenzgesetz mit Exponenten $-\delta$. Dieser Exponent konnte im Rahmen eines einfachen Modells (das "Leaky-Box" Modell) relativ genau auf $\delta = 0,53 \pm 0,06$ bestimmt werden. Es ist schwer vorstellbar, dass die Massenbelegung vor dem Entweichen aus der Galaxie beliebig klein werden könnte, wie das gemessene

Potenzgesetz proportional zu $E^{-0.53}$ es bedingen würde. Daher wird ein asymptotischer Wert Λ_0 eingeführt. Obwohl die Messung einen Wert von 0 für diesen Parameter nicht definitiv ausschließt, ist ein Wert von $0,31 \text{ g/cm}^2$ am wahrscheinlichsten.

Ein von Null verschiedener Wert für Λ_0 führt in den beobachteten Energiespektren zu einer Veränderung des spektralen Indexes oberhalb einer Energie von einigen 100 GeV/amu . Dieser Effekt muss sorgfältig studiert werden, bevor man Aussagen über die Energiespektren an den Quellen der Kosmischen Strahlung treffen kann.

Ein Computerprogramm zur numerischen Simulation der Ausbreitung Kosmischer Strahlung in der Milchstraße ist GALPROP. Das gemessene Verhältnis von Bor zu Kohlenstoff wird hierbei am besten mit einem spektralen Index der Ausbreitung $\delta = 0,34$ beschrieben. Dies unterscheidet sich signifikant vom Wert, der mit dem Leaky-Box Modell gefunden wurde. Allerdings muss man beachten, dass die Parameter δ nicht direkt verglichen werden können. Um die gemessenen Daten zu beschreiben, wird δ im Leaky-Box Modell durch den asymptotischen Wert Λ_0 moduliert, während es bei GALPROP bei niedrigen Energien durch den Effekt der Wiederbeschleunigung Kosmischer Strahlung moduliert wird.

Eine bedeutende Übereinstimmung der beiden Modelle ist aber, dass der spektrale Index der Quellenspektren zu $\alpha = 2,3$ bis $2,4$ bestimmt werden kann. Dies stimmt mit früheren Ergebnissen von TRACER überein, die aus Energiespektren primärer Elemente der Kosmischen Strahlung abgeleitet wurden.

Es ist offensichtlich, dass eine Messung des Verhältnisses von Bor zu Kohlenstoff oder anderer sekundär zu primär Verhältnissen bei höheren Energien als bisher wünschenswert ist, um die Ausbreitung Kosmischer Strahlung besser zu bestimmen. Ein langer Flug von TRACER könnte das erreichen. Die Einschränkung der Messgenauigkeit durch atmosphärische Produktion von sekundären Teilchen oberhalb des Detektors wird dann allerdings die hauptsächliche Quelle an Unsicherheit sein. Diese kann nur durch ein Experiment im Weltraum vermieden werden. Grundsätzlich ist ein Einsatz eines Experimentes basierend auf dem TRACER Konzept im Weltraum denkbar.

NEDERLANDSE SAMENVATTING¹

Met *kosmische straling* worden de atoomkernen en elektronen bedoeld, die uit het heelal de atmosfeer van de Aarde binnendringen. Deze deeltjes zijn voor het grootste deel van galactische oorsprong, en worden versneld in schokfronten, zoals die bijvoorbeeld ontstaan na een supernova.

Voordat de deeltjes de Aarde bereiken, bewegen ze zich gedurende circa 15 miljoen jaar voort door het Melkwegstelsel. Zij kunnen de Melkweg ook verlaten, of interactie ondergaan met de interstellaire materie. Op deze manier wordt het op Aarde waargenomen energiespectrum van kosmische straling niet alleen bepaald door de eigenschappen van de bronnen, maar ook door de wijze waarop de deeltjes propageren door het Melkwegstelsel.

Een aspect van deze propagatie is het ontsnappen uit de Melkweg. Dit proces kan worden vastgesteld door het meten van de verhouding van secundaire tot primaire kosmische straling, b.v. van boor ten opzichte van koolstof. Boor komt niet voor in de bronnen van kosmische straling, maar wordt geproduceerd wanneer koolstofdeeltjes op hun reis door het Melkwegstelsel in botsing komen met interstellaire materie. Is de afgelegde weg (d.w.z. kolomdichtheid) van koolstofdeeltjes voordat ze de Melkweg verlaten lang, dan wordt veel boor geproduceerd; bij een korte weg wordt weinig boor geproduceerd. De verhouding tussen boor en koolstof is dus een maat voor de hoeveelheid materie waar de kosmische straling doorheen reist voor zij de Melkweg verlaat.

Bij de Aarde aangekomen kan de galactische kosmische straling met een energie tot 10^{15} eV (electronvolt, $1 \text{ eV} = 1,6 \cdot 10^{-19}$ Joule) direct worden gemeten. Hiertoe worden deeltjesdetectoren, die de lading en energie van de deeltjes kunnen meten, ofwel in een baan om de Aarde, ofwel d.m.v. ballons aan de bovengrens van de atmosfeer gebracht. Voor beide methoden bestaan sterke beperkingen voor de gebruikte experimentele techniek, wat betreft het gewicht, de grootte, het stroomverbruik en de meettijd.

De grootste detector die tot nu toe met een ballon is gebruikt is TRACER, met een geometrische apertuur van $5 \text{ m}^2 \text{ sr}$. De detector werd gebouwd door de Universiteit van Chicago. Om de lading en energie te bepalen van de atoomkernen die de detector doorkruisen, worden uitsluitend elektromagnetische processen gebruikt.

Het ladingsgetal van iedere atoomkern wordt door een combinatie van scintillator- en Čerenkov-detectoren aan de bovenzijde en onderzijde van het instrument gemeten. Dit is nodig om de gevolgen van wisselwerkingen in de detector uit te filteren. De energiemeting vindt in drie onafhankelijke gebieden plaats: rond 1 GeV/amu met de onderste Čerenkov-

¹Many thanks to Marc van der Sluys for the translation!

detector, tussen 10 en 500 GeV/amu met het signaal van het “dE/dX-array” (gemeten door de bijna vlakke toename van het signaal in het regime van de “relativistic rise” van de specifieke ionisatie in het gas), en boven 700 GeV/amu met de overgangsstralingsdetector (gemeten aan de overgangsstraling die vrijkomt naast de specifieke ionisatie).

De TRACER detector is bij een drietal ballonvluchten ingezet. Als eerste werd in 1999 een testvlucht uitgevoerd. Daarop volgden twee langdurige ballonvluchten: in 2003 in Antarctica, en in 2006 van Zweden naar Canada. De tweede langdurige ballonvlucht moest helaas na 4,5 dagen worden afgelast, doordat geen toestemming kon worden verkregen voor een vlucht boven Russisch grondgebied. Na zijn laatste vlucht is de TRACER detector weer teruggebracht naar de universiteit van Chicago. Hij is overwegend intact, en kan worden opgeknapt voor een volgende vlucht.

Gedurende de tweede langdurige ballonvlucht konden de elementen van boor tot ijzer ($Z = 5$ tot 26) worden gemeten. De data van deze vlucht vormen de basis voor dit proefschrift.

Het zwaartepunt van de meting ligt bij de verhouding tussen boor en koolstof, om de voortplanting van de kosmische straling door de Melkweg te onderzoeken. Voor dit proefschrift werd de toestand van de detector na de vlucht getest, de data-analyse doorgevoerd, en uiteindelijk werden de metingen in het kader van de modellen van galactische propagatie geïnterpreteerd.

De data-analyse begint met de toepassing van een aantal correcties, welke uit de gemeten data zelf worden bepaald. Vervolgens werden de banen van de waargenomen deeltjes gereconstrueerd. Daarna was het mogelijk de lading en energie te bepalen van ieder gedetecteerd deeltje.

Het resultaat van dit proefschrift zijn de energiespectra van boor, koolstof, zuurstof en ijzer, tot een energiewaarde van 2 TeV/amu. Voor al deze elementen vinden we een overeenstemming met eerdere experimenten. Het spectrum van boor overtreft eerdere metingen significant in de hogere energieën. Daarnaast vond TRACER de tot nu toe hoogst gemeten energie in een boor-atoomkern: 6000 GeV/amu.

Uit de spectra van boor en koolstof konden hun abundanties als functie van de energie worden bepaald. Daarbij werd speciale zorg in acht genomen om systematische meetfouten door contaminatie van koolstof of atmosferische productie van boor te vermijden. Hiertoe werd een methode ontwikkeld om de atmosferische productie van boor uit de meetwaarden zelf af te schatten. Hoewel deze methode met de huidige data slechts kan dienen als test voor de berekende productiesnelheden, is ze interessant met het oog op toekomstige experimenten.

De gemeten verhouding van boor tot koolstof loopt tot 2 TeV/amu en overtreft de eerdere metingen van HEAO, CRN, ATIC en AMS-01 bij hogere energieën in nauwkeurigheid. De statistiek van de deeltjesaantallen is vergelijkbaar met die van het CREAM experiment, dat echter een tienmaal langere meettijd kende. Dit toont de betere mogelijkheden aan van het concept van TRACER, in het bijzonder voor toekomstige projecten.

Zoals reeds beschreven volgt de verhouding van boor tot koolstof de gemiddelde massakolom die de kosmische straling op haar weg door de Melkweg doorkruist voordat ze kan ontsnappen. Dit is een functie van de energie, een machtswet met exponent $-\delta$. Deze exponent kon in het kader van een simpel model (het “Leaky-Box” model) relatief nauwkeurig worden bepaald op $0,53 \pm 0,06$. Het is vrijwel onmogelijk dat de massakolom voor het ontsnappen

uit de Melkweg willekeurig klein zou kunnen worden, zoals de gemeten machtswet $E^{-0.53}$ voorschrijft. Om die reden is een asymptotische waarde Λ_0 ingevoerd. Hoewel de meting een waarde van nul voor deze parameter niet definitief uitsluit, is $\Lambda_0 = 0,31 \text{ g/cm}^2$ het meest waarschijnlijk.

Een waarde voor Λ_0 die afwijkt van nul leidt in de waargenomen energiespectra tot een verandering van de spectrale index boven een energie van enkele honderden GeV/amu. Dit effect moet zorgvuldig worden onderzocht, voordat men een uitspraak kan doen over de energiespectra van de bronnen van de kosmische straling.

GALPROP is een computerprogramma om de voortplanting van kosmische straling in de Melkweg numeriek te simuleren. De gemeten verhouding tussen boor en koolstof wordt hierin het best beschreven met een spectrale index van $\delta = 0,34$. Dit is significant anders dan de waarde die werd gevonden met het Leaky-Box model. Men moet echter bedenken dat deze waarden van δ niet direct vergeleken kunnen worden. Om de gemeten data te beschrijven wordt de waarde van δ in het Leaky-Box model veranderd door de asymptotische waarde Λ_0 , terwijl deze waarde in GALPROP bij geringe energieën wordt beïnvloed door het effect van herversnelling van de kosmische straling.

Een belangrijke overeenstemming van beide modellen is dat de spectrale index van de bronspectra op $\alpha = 2,3$ tot $2,4$ kan worden bepaald. Dit komt overeen met eerdere bepalingen, die werden afgeleid uit de energiespectra van primaire elementen in de kosmische straling.

Om de propagatie van kosmische straling beter te bepalen, is een meting gewenst van de verhouding van boor tot koolstof, of van andere verhoudingen van secundaire tot primaire elementen, bij hogere energieën dan tot nu toe gebeurd is. Een langdurige vlucht van TRACER zou dit kunnen bereiken. De beperking van de meetnauwkeurigheid door atmosferische productie van secundaire deeltjes boven de detector zal dan de voornaamste bron van onzekerheid zijn. Dit kan slechts worden vermeden met een experiment in de ruimte. In principe is het uitvoeren van zo'n experiment, gebaseerd op het concept van TRACER, een mogelijkheid.

BIBLIOGRAPHY

- [1] M. Aguilar et al. Relative composition and energy spectra of light nuclei in cosmic rays. Results from AMS-01. *ApJ*, 724:329–340, 2010.
- [2] F. A. Aharonian et al. High-energy particle acceleration in the shell of a supernova remnant. *Nature*, 432:75–77, 2004.
- [3] F. A. Aharonian et al. A detailed spectral and morphological study of the gamma-ray supernova remnant RX J1713.7–3946 with HESS. *A&A*, 449:223–242, 2006.
- [4] H. S. Ahn et al. Measurements of cosmic-ray secondary nuclei at high energies with the first flight of the CREAM balloon-borne experiment. *Astro. Ph.*, 30:133–141, 2008.
- [5] H. S. Ahn et al. Energy spectra of cosmic-ray nuclei at high energies. *ApJ*, 707:593–603, 2009.
- [6] H. S. Ahn et al. Discrepant hardening observed in cosmic-ray elemental spectra. *ApJ Letters*, 714:L89, 2010.
- [7] E. Amato, P. Blasi, and S. Gabici. Kinetic approaches to particle acceleration at cosmic ray modified shocks. *MNRAS*, 385:1946–1958, 2008.
- [8] C. D. Anderson. The positive electron. *Phys. Rev.*, 43:491, 1933.
- [9] T. Antoni et al. KASCADE measurements of energy spectra for elemental groups of cosmic rays: Results and open problems. *Astropart. Phys.*, 24:1–25, 2005.
- [10] W. B. Atwood et al. The large area telescope on the FERMI gamma-ray space telescope mission. *ApJ*, 697:1071–1102, 2009.
- [11] P. Auger. Extensive cosmic-ray showers. *Rev. Mod. Phys.*, 11:288, 1939.
- [12] M. Ave et al. Composition of primary cosmic-ray nuclei at high energies. *ApJ*, 678:262–273, 2008.
- [13] M. Ave et al. Propagation and source energy spectra of cosmic-ray nuclei at high energies. *ApJ*, 697:106–114, 2009.
- [14] M. Ave et al. *NIM A*, 2011. in preparation.

- [15] A. R. Bell. The acceleration of cosmic rays in shock fronts - I. *MNRAS*, 182:147–156, 1978.
- [16] E. Beuville et al. AMPLEX, a low-noise, low-power analog CMOS signal processor for multi-element silicon particle detectors. *NIM A*, 288:157–167, 1990.
- [17] J. B. Birks. Scintillations from organic crystals: Specific fluorescence and relative response to different radiations. *Proc. Phys. Soc. A*, 64:874–877, 1951.
- [18] J. Blümer, R. Engel, and J. R. Hörandel. Cosmic rays from the knee to the highest energies. *Prog. Part. Nucl. Phys.*, 63(2):293–338, 2009.
- [19] R. Brun and F. Rademakers. ROOT: An object oriented data analysis framework. *NIM A*, 389:81, 1997. See also <http://root.cern.ch/>, v5.24.
- [20] M. Buchvarova and P. I. Y. Velinov. Empirical model of cosmic ray spectrum in energy interval 1 MeV-100 GeV during 11-year solar cycle. *Adv. Space Res.*, 45:1026–1034, 2010.
- [21] M. L. Cherry. Measurements of the spectrum and energy dependence of x-ray transition radiation. *Phys. Rev. D*, 17(9):2245–2260, 1978.
- [22] M. L. Cherry and D. Müller. Measurements of the frequency spectrum of transition radiation. *Phys. Rev. Letters*, 38(1):5–8, 1977.
- [23] J. W. Cronin, T. K. Gaisser, and S. P. Swordy. Cosmic rays at the energy frontier. *Scientific American*, 276:44–49, 1997.
- [24] G. A. de Nolfo et al. Observations of the Li, Be, and B isotopes and constraints on cosmic-ray propagation. *Adv. Space Res.*, 38:1558–1564, 2006.
- [25] O. Dössel. *Bildgebende Verfahren in der Medizin*. Springer Verlag, Berlin (GER), 2008.
- [26] D. C. Ellison et al. Galactic cosmic rays from supernova remnants. II. Shock acceleration of gas and dust. *ApJ*, 487:197–217, 1997.
- [27] J. J. Engelmann et al. Charge composition and energy spectra of cosmic-ray nuclei for elements from Be to Ni. Results from HEAO-3-C2. *A&A*, 233:96–111, 1990.
- [28] E. Fermi. On the origin of cosmic radiation. *Phys. Rev.*, 75(8):1169, 1949.
- [29] F. Gahbauer et al. A new measurement of the intensities of the heavy primary cosmic-ray nuclei around 1 TeV/amu. *ApJ*, 607:333–341, 2004.
- [30] T. K. Gaisser. *Cosmic rays and particle physics*. Cambridge University Press, Cambridge (UK), 1990.
- [31] M. Garcia-Munoz, G. M. Mason, and J. A. Simpson. The age of galactic cosmic rays derived from the abundance of ^{10}Be . *ApJ*, 217:859–877, 1977.

- [32] N. Gehrels. Confidence limits for small numbers of events in astrophysical data. *ApJ*, 303:336–346, 1986.
- [33] V. L. Ginzburg and S. Syrovatskii. *On the Origin of Cosmic Rays*. McMillan, New York (USA), 1964.
- [34] M. L. Goldstein et al. Energy loss of cosmic rays in the interplanetary medium. *Phys. Rev. Letters*, 25(12):832–835, 1970.
- [35] K. Greisen. End to the cosmic-ray spectrum? *Phys. Rev. Letters*, 16(17):748, 1966.
- [36] J. H. Han et al. Pulsar rotation measures and the large-scale structure of the galactic magnetic field. *ApJ*, 642:868–881, 2006.
- [37] V. F. Hess. Über Beobachtungen der durchdringenden Strahlung bei sieben Freiballonfahrten. *Physik. Zeitschr.*, 13:1084, 1912.
- [38] V. F. Hess. Über den Ursprung der durchdringenden Strahlung. *Physik. Zeitschr.*, 14:610, 1913.
- [39] A. M. Hillas. The origin of ultra-high energy cosmic rays. *Annu. Rev. Astron. Astrophys.*, 22:425, 1984.
- [40] J. A. Hinton. The status of the HESS project. *New Astr. Rev.*, 48:331–337, 2004.
- [41] J. A. Hinton and W. Hofmann. Teraelectronvolt Astronomy. *Annu. Rev. Astron. Astrophys.*, 47:523–565, 2009.
- [42] C. Höppner. Cosmic ray composition at high energies: Results from the TRACER project. Master’s thesis, TU Munich, 2006.
- [43] J. R. Hörandel. Models of the knee in the energy spectrum of cosmic rays. *Astropart. Phys.*, 21(3):241–265, 2004.
- [44] M. H. Israel et al. Isotopic composition of cosmic rays: Results from the cosmic ray isotope spectrometer on the ACE spacecraft. *Nucl. Phys. A*, 758:201–208, 2005.
- [45] K.-H. Kampert et al. Cosmic ray energy spectra and mass composition at the knee - recent results from KASCADE. *Nuc. Phys. B (Proc. Suppl.)*, 136:273–281, 2004.
- [46] H. Kang. Cosmic ray acceleration in supernova remnant shocks. *J. Kor. Astron. Soc.*, 43:1–15, 2010.
- [47] W. Kolhörster et al. Gekoppelte Höhenstrahlen. *Naturwiss.*, 10:576, 1938.
- [48] A. N. Kolmogorov. The local structure of turbulence in incompressible viscous fluid for very large Reynolds numbers. *Proc.: Math. Phys. Sciences*, 434(1890):9–13, 1991. Translation of the seminal paper by Kolmogorov in 1941.

- [49] A. Kowalski. The time development of muon and x-ray signals in proportional counters. Master's thesis, The University of Chicago, 2006.
- [50] G. D. Lafferty and T. R. Wyatt. Where to stick your data points: The treatment of measurements in wide bins. *NIM A*, 355:541–547, 1995.
- [51] P. O. Lagage and C. J. Cesarsky. The maximum energy of cosmic rays accelerated by supernova shocks. *A&A*, 125:249–257, 1983.
- [52] J. L'Heureux et al. A detector for cosmic-ray nuclei at very high energies. *NIM A*, 295:246–260, 1990.
- [53] M. L. Lijowski et al. Elemental abundances for $3 \leq Z \leq 30$ galactic cosmic ray nuclei measured by the cosmic ray isotope spectrometer on ACE. *APS Meeting Abstracts*, page 807ff, 1998.
- [54] M. S. Longair. *High energy astrophysics*. Cambridge University Press, Cambridge (UK), 1992.
- [55] P. Maestro et al. Energy cross-calibration from the first CREAM flight: Transition radiation detector versus calorimeter. In *Proceedings of the 30th International Cosmic Ray Conference*. Merida, Mexico, 2007.
- [56] N. Matsufuji et al. The response of a NE102 scintillator to passing-through relativistic heavy ions. *NIM A*, 437:346–353, 1999.
- [57] J.-P. Meyer et al. Galactic cosmic rays from supernova remnants. I. A cosmic-ray composition controlled by volatility and mass-to-charge ratio. *ApJ*, 487:182–196, 1997.
- [58] R. A. Millikan and I. S. Bowen. High frequency rays of cosmic origin I. Sounding balloon observations at extreme altitudes. *Phys. Rev.*, 27(4):353–361, 1926.
- [59] D. Müller. Transition radiation detectors in particle astrophysics. *NIM A*, 522:9–15, 2004.
- [60] D. Müller et al. Energy spectra and composition of primary cosmic rays. *ApJ*, 374:356–365, 1991.
- [61] M. Nagano and A. A. Watson. Observations and implications of ultrahigh-energy cosmic rays. *Rev. Mod. Phys.*, 72(3):689, 2000.
- [62] K. Nakamura et al. (Particle Data Group). Review of particle physics. *J. Phys. G*, 37, 2010.
- [63] G. Navarra. Study of cosmic ray primaries between 10^{12} and 10^{16} eV from EAS-TOP. In *Proceedings of the 28th International Cosmic Ray Conference*. Tsukuba, Japan, 2003.
- [64] S. H. Neddermayer and C. D. Anderson. Note on the nature of cosmic ray particles. *Phys. Rev.*, 51:884, 1937.

- [65] A. D. Panov et al. Elemental energy spectra of cosmic rays from the data of the ATIC-2 experiment. *Bull. Russ. Acad. Sci., Phys.*, 71(4):494–497, 2007.
- [66] A. D. Panov et al. Relative abundances of cosmic-ray nuclei B-C-N-O in the energy region from 10 GeV/n to 300 GeV/n. Results from ATIC-2 (the science flight of ATIC). In *Proceedings of the 30th International Cosmic Ray Conference*. Merida, Mexico, 2007.
- [67] M. Paterno. Calculating efficiencies and their uncertainties. DØ note 2861, <http://home.fnal.gov/~paterno/images/effic.pdf>, 2003.
- [68] V. S. Ptuskin. Transport of high energy cosmic rays. *Adv. Space Res.*, 19(5):697–705, 1997.
- [69] V. S. Ptuskin. Propagation, confinement models, and large-scale dynamical effects of galactic cosmic rays. *Space Sci. Rev.*, 99:281–293, 2001.
- [70] V. S. Ptuskin. Cosmic ray transport in the galaxy. *J. of Phys.: Conf. Ser.*, 47:113–119, 2006.
- [71] V. S. Ptuskin et al. On leaky-box approximation to GALPROP. *Astropart. Phys.*, 31:284–289, 2009.
- [72] V. S. Ptuskin et al. Spectrum of Galactic cosmic rays accelerated in supernova remnants. *ApJ*, 718:31–36, 2010.
- [73] A. Romero-Wolf. Energy loss and energy deposit in single-wire proportional tubes. Master’s thesis, University of Chicago, 2005.
- [74] B. Rossi and B. Hall. Variation of the rate of decay of mesotrons with momentum. *Phys. Rev.*, 59(3):223–228, 1941.
- [75] F. Schüssler et al. Measurement of the energy spectrum of cosmic rays above 10^{18} using the Pierre Auger Observatory. *Phys. Lett. B*, 685:239, 2010.
- [76] T. Stanev. *High energy cosmic rays*. Springer Verlag, Berlin (GER), 2010.
- [77] J. C. Street and E. C. Stevenson. New evidence for the existence of a particle of mass intermediate between proton and electron. *Phys. Rev.*, 52:1003, 1937.
- [78] A. W. Strong and I. V. Moskalenko. Propagation of cosmic-ray nucleons in the Galaxy. *ApJ*, 509:212–228, 1998.
- [79] A. W. Strong and I. V. Moskalenko. Models for Galactic cosmic-ray propagation. *Adv. Space Res.*, 27(4):717–726, 2001.
- [80] A. W. Strong, I. V. Moskalenko, and V. S. Ptuskin. Cosmic-ray propagation and interactions in the Galaxy. *Annu. Rev. Nucl. Part. Sci.*, 57:285–327, 2007.

- [81] S. P. Swordy. Expectations for cosmic ray composition changes in the region 10^{14} to 10^{16} eV. In *Proceedings of the 24th International Cosmic Ray Conference*, volume 2, page 697, 1995.
- [82] S. P. Swordy et al. Measurements of x-ray transition radiation from plastic fibers. *NIM*, 193:591–596, 1982.
- [83] S. P. Swordy et al. Relative abundances of secondary and primary cosmic rays at high energies. *ApJ*, 349:625–633, 1990.
- [84] S. Toscano et al. Observation of the anisotropy in arrival direction of cosmic rays with IceCube. arXiv:1011.5428v1 [astro-ph.HE], 2010.
- [85] C. H. Tsao et al. Partial cross sections of nucleus-nucleus reactions. *ApJ*, 501:920–926, 1998.
- [86] A. E. Vladimirov et al. GALPROP WebRun: an internet-based service for calculating cosmic ray propagation and associated diffuse emissions. arXiv:1008.3642v1 [astro-ph.HE], 2010.
- [87] R. Voltz et al. Influence of the nature of ionizing particles on the specific luminescence of organic crystals. *J. Chem. Phys.*, 45:3306–3311, 1966.
- [88] S. P. Wakely et al. Transition radiation detectors for energy measurements at high Lorentz factors. *NIM A*, 531:435–444, 2004.
- [89] W. R. Webber et al. Formula for calculating partial cross sections for nuclear reactions of nuclei with $E \geq 200$ MeV/nucleon in hydrogen targets. *Phys. Rev. C*, 41(2):566–571, 1990.
- [90] W. R. Webber et al. Individual charge changing fragmentation cross sections of relativistic nuclei in hydrogen, helium, and carbon targets. *Phys. Rev. C*, 41(2):533–546, 1990.
- [91] W. R. Webber et al. Total charge changing and mass changing cross sections of relativistic nuclei in hydrogen, helium, and carbon targets. *Phys. Rev. C*, 41(2):520–532, 1990.
- [92] T. C. Weekes et al. VERITAS: The Very Energetic Radiation Imaging Telescope Array System. *Astropart. Phys.*, 17:221–243, 2002.
- [93] G. D. Westfall et al. Fragmentation of relativistic ^{56}Fe . *Phys. Rev. C*, 19:1309–1323, 1979.
- [94] M. E. Wiedenbeck et al. The level of solar modulation of galactic cosmic rays from 1997 to 2005 as derived from ace measurements of elemental energy spectra. In *Proceedings of the 29th International Cosmic Ray Conference*. Pune, India, 2005.
- [95] N. E. Yanasak et al. Measurement of the secondary radionuclides ^{10}Be , ^{26}Al , ^{36}Cl , ^{54}Mn , and ^{14}C and implications for the Galactic cosmic-ray age. *ApJ*, 563:768–792, 2001.

-
- [96] G. T. Zatsepin and V. A. Kuz'min. Upper limit of the spectrum of cosmic rays. *JETP Lett.*, 4(3):78, 1966.

ACKNOWLEDGMENTS

I am grateful to Prof. Dr. Sijbrand de Jong for his advice, his kind support, and the opportunity to graduate from this young and vibrant institute at the Radboud Universiteit Nijmegen.

I would like to express my deepest gratitude to Prof. Dr. Dietrich Müller and Prof. Dr. Jörg Hörandel. In the last four years they have accompanied, supported, and encouraged me on my way to the doctoral degree. Dietrich warmly welcomed me in Chicago and gave me the best support a young PhD student can imagine. Through long discussions, he sharpened my mind for research and made my best performance possible. He taught me that sometimes “you can’t have it both ways.” Jörg introduced me to TRACER and made the whole story possible. He was always willing to listen and always had an open door for me (or telephone/email when the Atlantic Ocean was between us). He discussed physics with me as a colleague, not as a boss, which taught me countless lessons for career and life. This work would never have been possible without his support, advice, and patience.

My thanks go also to Prof. Dr. Paul Groot who welcomed me cordially into his department. The atmosphere at the department is embossed by his kindness and openness.

I am most thankful to Dr. Patrick (Jojo) Boyle. His patience, help, and optimism guided me through all the pitfalls that TRACER dug for me. His expertise, and his willingness to share it, saved me on many occasions throughout this PhD adventure. Jojo was the perfect second (and sometimes first) opinion to Dietrich; together they made sure I looked at all problems from all sides until we believed the solutions.

In the long line of people who worked toward the success of TRACER, I am but the latest addition. All members of the TRACER project have my gratitude. They paved the way for my work and for the outstanding performance of TRACER. Special thanks goes to Maximo Ave (silent but brilliant advice), Masakatsu Ishimura (lessons on charge and Japanese computer power), Christian Höppner (taking the data), Elliott Brannon (master of the flat table), Jesse Marshall (fitter of ’em all), and Aaron Martell (great fun with ^{55}Fe).

Many thanks are due my colleagues and friends at the University of Chicago and the Radboud University Nijmegen. They are responsible for the great atmosphere in which a PhD student can flourish and achieve the best results in a relatively relaxed way. Special thanks go to the Journal Club at UofC; don’t just read about photons!

I especially want to thank Tom and Peggy, and all of the I-House crew! They succeeded at the hardest task: to make a Bavarian feel at home in Chicago. It took a while, but Chicago became my home and I never want to forget those three years of cold, heat, pain, laughter, crazy mischief, and friendships never ending! We take strawberries for butter and polish the

soccer ball!

I also want to thank all of my friends at home and especially at Hütte. They supported me and distracted me from my problems these past years. To those who never forgot me although I was far away, those who believed in me although I was pessimistic, those who encouraged me although I couldn't explain myself!

I give my special gratitude to the little Family: Mini, Carina, Phillip and Rebecca. Your support kept me sane, sound, and pushed me through! You mean the world to me!

Last but not least: Mein ganz besonderer Dank gilt meinen Eltern und meinem Bruder. Erst durch ihre Unterstützung konnte ich mich verwirklichen und zu dem werden, der ich heute bin. Die Energie, die meine Eltern in mich investieren, macht meinen Erfolg erst möglich.

CURRICULUM VITAE AND LIST OF PUBLICATIONS

Curriculum Vitae

Andreas Obermeier was born on the 15th of December in the year 1980 in Eggenfelden, Germany.

There, he also attended high school, the Karl-von-Closen Gymnasium, from which he graduated in the year 2000. For one year he then served his civil service at a private school for handicapped children.

In 2001, Andreas moved to Karlsruhe, Germany, to study physics. He became a member of the academic club “A. V. Hütte” (Akademischer Verein Hütte e. V.), in which he fulfilled leading positions.

While studying physics, Andreas chose the subsidiary subjects of physical chemistry, imaging techniques in medicine, and astroparticle physics and cosmology.

For his Diploma thesis, he joined his supervisor J. Hörandel in the group of the Auger Observatory at the research center in Karlsruhe (now KIT). The title of the Diploma thesis is “The fluorescence yield of air excited by electrons measured with the AIRFLY experiment”. Its purpose was to find a better calibration for the fluorescence telescope of the Auger Observatory by measuring the fluorescence yield of air in controlled environments. Andreas undertook several trips to Fermilab and the Argonne National Laboratory (both near Chicago, USA) for measurement campaigns at four different particle accelerators. He finished his Diploma thesis, and thus his studies, in December 2006.

During his stays at the University of Chicago, and later through his thesis advisor, Andreas came in contact with the TRACER project. Starting his PhD thesis in February 2007, he moved to Chicago and worked there under the supervision of D. Müller and P. Boyle for three years. He then came to the Radboud University in Nijmegen, following his thesis advisor J. Hörandel, to complete this thesis.

List of Publications

Corresponding Author

- Diploma Thesis, “The Fluorescence Yield of Air excited by Electrons measured with the AIRFLY Experiment”, 12/2006, Report FZKA 7284
- M. Ave et al., “Spectrally resolved pressure dependence measurements of air fluorescence emission with AIRFLY”, NIM A 597:41, 2008
- A. Obermeier et al., “On the atmospheric production of cosmic-ray nuclei”, ApJ, in preparation
- A. Obermeier et al., “The boron to carbon abundance ratio and Galactic propagation of cosmic radiation”, ApJ, in preparation
- A. Obermeier et al., “Energy spectra of primary and secondary cosmic-ray nuclei measured with TRACER”, ApJ, in preparation
- A. Obermeier et al., “The TRACER Project — Measuring Galactic Cosmic Rays”, Adv. Space Res., in preparation, solicited COSPAR’10 contribution

Co-Author

- P. Privitera et al. (AIRFLY-Collaboration), “Measurement of the pressure dependence of air fluorescence emission induced by electrons”, Astroparticle Physics 28:41, 2007
- M. Ave et al., “Energy dependence of air fluorescence yield measured by AIRFLY”, NIM A 597:46, 2008
- M. Ave et al., “Temperature and humidity dependence of air fluorescence yield measured by AIRFLY”, NIM A 597:50, 2008
- M. Ave et al., “A novel method for the absolute fluorescence yield measurement by AIRFLY”, NIM A 597:55, 2008
- D. Müller for TRACER, “Studies of high-energy cosmic rays with TRACER”, Proceedings of the 31st ICRC, Lodz, 2009
- M. Ave et al. “The balloon-borne cosmic-ray detector TRACER”, NIM A, in preparation

Contributions to Conferences

- DPG Frühjahrstagung, Dortmund (GER), 3/2006, Talk: “Messung der Fluoreszenzlicht-Ausbeute mit AIRFLY”
- 4th Fluorescence Workshop, Prag-Pruhonice (CZ), 5/2006, Talk: “Measurement of the Air Fluorescence Yield with AIRFLY”
- 30th International Cosmic-Ray Conference, Merida (MEX), 7/2007
- 5th Fluorescence Workshop, Madrid (ESP), 9/2007, Talk: “Spectrally Resolved Pressure Dependence Measurements of Air Fluorescence Emission with AIRFLY”
- International School of Cosmic-Ray Astrophysics (16th course), Erice (ITA), 7/2008, Talk: “Galactic Propagation and Source Abundances of Cosmic-Ray Nuclei at High Energies”
- 37th COSPAR Scientific Assembly, Montreal (CAN), 7/2008, Talk: “Galactic Propagation and Source Abundances of Cosmic-Ray Nuclei at High Energies: Discussion of Results from TRACER”
- APS April Meeting, Denver (USA), 5/2009, Talk: “Composition and Propagation of Galactic Cosmic-Ray Nuclei at High Energies”
- 31st International Cosmic-Ray Conference, Lodz (PL), 7/2009, Talk: “Propagation and Energy Spectra of Galactic Cosmic-Ray Nuclei at High Energies”
- 38th COSPAR Scientific Assembly, Bremen (GER), 7/2010, Solicited Talk: “Determining Composition and Propagation of Galactic Cosmic Rays with TRACER”
- 22nd European Cosmic-Ray Symposium, Turku (FIN), 8/2010, Talk: “Measuring the B/C ratio with TRACER”

